Watching The World Sweat

Development and utilization of an in-situ conductivity sensor for monitoring chloride dynamics in high temperature hydrothermal fluids at divergent plate boundaries

Benjamin Isaac Larson

A dissertation
submitted in partial fulfillment of the
requirements for the degree of

Doctor of Philosophy

University of Washington
2008

Program Authorized to Offer Degree:
School of Oceanography

INFORMATION TO USERS

The quality of this reproduction is dependent upon the quality of the copy submitted. Broken or indistinct print, colored or poor quality illustrations and photographs, print bleed-through, substandard margins, and improper alignment can adversely affect reproduction.

In the unlikely event that the author did not send a complete manuscript and there are missing pages, these will be noted. Also, if unauthorized copyright material had to be removed, a note will indicate the deletion.

ProQuest LLC
789 E. Eisenhower Parkway
PO Box 1346
Ann Arbor, MI 48106-1346

University of Washington
Graduate School

This is to certify that I have examined this copy of a doctoral dissertation by

Benjamin Isaac Larson

and have found that it is complete and satisfactory in all respects,
and that any and all revisions required by the final
examining committee have been made.

Chair of the Supervisory Committee:

Marvin D. Lilley

Reading Committee:

Marvin D. Lilley

Deborah S. Kelley

William S. D. Wilcock

Date: 1-7-08

In presenting this dissertation in partial fulfillment of the requirements for the doctoral degree at the University of Washington, I agree that the Library shall make its copies freely available for inspection. I further agree that extensive copying of the dissertation is allowable only for scholarly purposes, consistent with "fair use" as prescribed in the U.S. Copyright Law. Requests for copying or reproduction of this dissertation may be referred to ProQuest Information and Learning, 300 North Zeeb Road, Ann Arbor, MI 48106-1346, 1-800-521-0600, to whom the author has granted "the right to reproduce and sell (a) copies of the manuscript in microform and/or (b) printed copies of the manuscript made from microform."

Signature Benjamin Lunn

Date 1-7-08

University of Washington

Abstract

Watching The World Sweat
Development and utilization of an in-situ conductivity sensor for monitoring chloride dynamics in high temperature hydrothermal fluids at divergent plate boundaries

Benjamin Isaac Larson

Chair of the Supervisory Committee:
Professor Marvin D. Lilley
Oceanography

The magmatic upwelling that drives plate tectonic motion at divergent plate boundaries also heats seawater circulating within the Earth's crust. The seawater undergoes physical and chemical changes beneath the surface and the resulting buoyant hydrothermal fluid ascends to the seafloor where it is comes out of structures called hydrothermal vents. One subsurface process of particular interest is phase separation, which is the transformation of a homogenous fluid into two phases, each with properties different from the original fluid. Phase separation is the dominant control on chloride in hydrothermal systems and chloride controls the distribution of all other chemical species. Thus, the measurement of chloride in hydrothermal fluids gives insight into extreme subsurface processes that are inherently difficult to probe. Since these processes evolve with time, measurements must be taken on a continuous basis. The research presented herein discusses the development and utilization of an instrument capable of continuously monitoring the hot salty solutions that flow out of hydrothermal pores in the Earth's crust. Instruments were deployed at two different mid-ocean ridge hydrothermal systems. An array of instruments was deployed on the Juan de Fuca Ridge at the Main Endeavour Field 12-15 months after a magmatic intrusion. Tidal changes and non-tidal changes on timescales of minutes to hours were observed. Chloride data were also used to infer subsurface mixing between two non-seawater fluids at depths below the seafloor between 486 and 695 meters.

Another instrument was deployed at Bio 9' vent at 9°50'N on the East Pacific Rise in the immediate vicinity of seismometers monitoring earthquake activity. The hydrothermal response to intense seismicity was observed on two separate occasions. On the basis of these observations, conditions of subsurface phase separation were estimated at pressures between 269 and 288 bars and temperatures between 369.7 and 403.5°C. Recurrent chloride spikes were also observed, with magnitudes up to 720 mmol/kg and durations up to 7 minutes. At both study sites, data indicate the influence of subsurface fluids with chloride concentrations greater than seawater. These observations may help resolve the apparent chloride deficit indicated by venting of chloride-depleted fluids over decadal timescales.

TABLE OF CONTENTS

Page

LIST OF FIGURES

Figure Number **Page**

LIST OF TABLES

Table Number **Page**

Acknowledgements

It has been a great privilege to work with a whole community of exceptional scientists. Marv Lilley and Eric Olson conduct ambitious and first rate hydrothermal research, always pushing the limits and succeeding under the most extreme conditions. I have always considered myself fortunate to be part of their crew. Thanks to Dave Butterfield for fruitful conversations at sea about hydrothermal chemistry. Those talks not only taught me a great deal but also helped me pass the time during those long weather delays. Thanks also to Debbie Kelley whose innovative approach to outreach and dedication to student involvement gave me the opportunity and the language to bring our amazing science to the public. Will Wilcock served on my committee and held me accountable for the hard details that are the foundation of good science; without his input, the research would have suffered. Al Devol also served on my committee and made me examine the assumptions I take for granted when surrounded by hydrothermal chemists.

None of the research would have been possible without the capable minds and quick hands of the Ocean Engineering Services Group. In particular, I'd like to mention Peter Kaufmann, the godfather of the resistivity probe, and Rex Johnson, who is all knowing and the fastest solder gun this side of the Mississippi. Also, thanks to all the personnel of the Alvin, Jason and ROPOS submersibles and Atlantis and Thompson R/V's who kindly put our instruments out and brought them back up.

Thanks also to Ocean Administration, especially Su Tipple and Tracie Watkins who grease the wheels of academic research that might otherwise come to a halt.

Many thanks to my lab mates: Giora Proskurowski, Brooke Love and Susan Lang, capable scientists all, and especially Susan who can quickly understand complex problems outside her expertise and provide substantive feedback. Several other people kept me grounded during my time in Seattle: Red Tide, the softball team with a heart; and the other three of the Fabulous Four: Masumi, Cindy and Susan.

My family also deserves special thanks. Mom, Dad, Dan and Matt, You have helped make me who I am.

And Sarah and Lily, you are what makes every day worthwhile.

Dedication

For Sarah

Chapter 1 – Overview

The drift of the Earth's massive tectonic plates on top of a layer of molten lava is driven, in part, by the creation of new crust at divergent plate boundaries. As magma upwells from the mantle in locations where chunks of the crust are pulling apart, seawater circulates within the rock, convectively cooling the solidifying magma at pressures several hundred times higher than at the Earth's surface. In this type of system, known as a mid-ocean ridge hydrothermal system, seawater can be heated to extremely high temperatures (Alt and Back, 2003; Alt, 1985). Under these conditions, seawater phase separates, creating fluids with chemical and physical properties significantly different than the seawater precursor (Bischoff and Pitzer, 1989; Butterfield et al., 2003; Von Damm, 1995). These hot buoyant fluids spew out of holes in the earth's surface known as hydrothermal vents.

One goal of hydrothermal chemistry is to use the properties of hydrothermal vent fluids to constrain subsurface pressures and temperatures. However, the extreme nature of hydrothermal processes and their remote location makes the study of mid-ocean ridge (MOR) hydrothermalism a multilayered problem. Moreover, seafloor spreading is not a smooth function with respect to time. Rather, crust formation is sporadic, occurring in discrete bursts of activity marked by high heat and mass flux as well as rapid variability in hydrothermal chemistry (Delaney et al., 1998; Lilley et al., 2003; Malinvero and Pockalny, 1990; McClain et al., 1993). Thus, our understanding of MOR hydrothermalism relies, in part, on our ability to measure the properties of high temperature vent fluids on a continuous basis.

The collection of discrete fluid samples for later analysis is an extremely informative technique but it is limited in its temporal coverage. This approach requires a research vessel and some type of submersible vehicle and even when these conditions are met, a given hydrothermal vent may be sampled only once a day. Furthermore, the time between cruises to a particular site can range from months to years. Thus, fluid sampling may miss periods of short-lived variability altogether (Butterfield et al., 1997; Lilley et

al., 2003; Von Damm et al., 1995). Given the short timescales (minutes to hours) and unpredictability of hydrothermal processes, there is a genuine need for new and novel techniques that can continuously analyze the system as it exists in its natural state. Such techniques increase the likelihood of observing changes in vent effluent associated with bursts of volcanic or tectonic activity.

Many existing in-situ analytical methods preclude their use in the typically inaccessible and extreme environments of deep-sea hydrothermal vents. Thus, the development of a viable in-situ device must meet several criteria. It must be robust enough to withstand the high temperatures and pressures characteristic of the target environment (Delaney et al., 1992; Von Damm et al., 2003) and it must be simple enough that it can be deployed by the unwieldy manipulators typically used by manned submersibles and remotely operated vehicles (ROV's). In addition, the data collection process must not use more power than can be provided by a battery pack with a limited lifetime; the size of the data collected cannot exceed the memory available to store it; and the design must be capable of remaining on the seafloor for extended periods of time.

Fluid parameters measured by existing instruments that meet the aforementioned requirements include temperature (Scheirer et al., 2006; Tivey et al., 2002), pH (Ding and Seyfried, 1996), H_2 and H_2S (Ding et al., 2001). One notable parameter missing from this list is chloride. Dissolved chloride is the master chemical variable in hydrothermal fluids and nearly all other chemical species either correlate or anti-correlate with chloride (Butterfield et al., 2003; Butterfield et al., 1994; Butterfield et al., 1990; Seyfried et al., 1986; Von Damm, 1995). Chloride is also useful in diagnosing the effects of phase separation because it does not participate significantly in water-rock reactions during ascent (Butterfield et al., 2003; Butterfield et al., 1994; Seewald and Seyfried, 1990). The effects of phase separation are of particular interest because of the observed chloride deficit in vent fluids over decadal timescales (Butterfield et al., 1994; Lilley et al., 2003; Von Damm, 2004). Simply put, chloride-depleted hydrothermal fluids have been venting for so long in some cases that it's not clear what happens to the remaining chloride.

The goal of the present study is to develop an instrument that can make in-situ measurements of chloride concentration in hydrothermal fluids with temperatures up to 400°C and at pressures up to 250 bars. This information will be used to constrain the pressure and temperature conditions of fluid circulation, including how these parameters evolve over time both before and after periods of intense volcanic activity.

The results of the study are presented in three chapters. Chapter 2 deals with the design, construction and calibration of an in-situ chloride sensor. Chapter 3 discusses a large scale deployment of 10 instruments 12-15 months after an intrusive magmatic event at the Juan de Fuca Ridge in the Northeast Pacific Ocean (Johnson et al., 2000; Lilley et al., 2003) .Within the context of this discussion, pressure and temperature of hydrothermal circulation are constrained and the impact of the ocean tides is considered including the role played by critical fluids in tidally correlated changes. Also, a possible explanation of the chloride deficit is considered. Chapter 4 discusses the deployment of a single instrument 9-14 months before an eruption at 9°50' N on the East Pacific Rise (Tolstoy et al., 2006). The chloride data from this deployment are complimented by seismic data (Tolstoy et al., 2006). The combined data are used to constrain pressure and temperature of subsurface hydrothermal processes occurring in conjunction with seismic events. We also consider a second possible explanation for the chloride deficit in MOR hydrothermal systems, short-lived bursts of chloride rich fluid, which can't be seen with discrete sampling techniques.

The data presented herein represent the most extensive set of time-series chloride measurements ever collected at MOR high temperature vents. The data are used to shed light on the evolution of subsurface hydrothermal conditions and to help answer questions as to the fate of chloride in hydrothermal systems. Although future studies will be needed to refine the theories discussed below, this work represents an important contribution to our understanding of the forbidding and ever-changing hydrothermal environments that vigorously churn thousands of meters beneath the ocean surface.

Chapter 2 – Instrument Description and Calibration

In-situ Measurement of Dissolved Chloride in High Temperature Hydrothermal Fluids

Summary

The ability to continuously monitor chemical properties of hydrothermal vent effluents for extended periods of time is essential to understanding dynamic processes responsible for the temporally variable nature of mid-ocean ridge hydrothermal systems. Although instruments do exist for some parameters, there has been no sensor capable of measuring the chloride concentration, an indicator of possible phase separation, on a real-time and long-term basis. In this article, we discuss the construction of a novel instrument which measures solution resistance as a proxy for chloride concentration. The sensor consists of four gold electrodes embedded in a cylindrical ZrO_2 ceramic housing. It has been successfully deployed in several high temperature vents at the Main Endeavour Field (MEF) on the Juan de Fuca ridge in the NE Pacific, and calibrated under simulated hydrothermal conditions ranging up to 380°C and 300 bars. The in-situ data clearly demonstrate a tidal influence on the effluent from some high temperature vents possibly relating to a subsurface mixing process involving non-seawater end-members. Non-tidal changes are used to constrain the sequence and type of controls operating on fluids circulating within the subsurface.

1. Introduction

The production of new oceanic lithosphere at divergent plate boundaries is accompanied by fluid circulation within the upper crust at high temperatures and pressures. If this circulating fluid is sufficiently heated, it will undergo phase separation resulting in a significant alteration of fluid composition. The result of this process is the production of one phase that is denser than seawater and enriched in chloride and other major elements and another phase that is less dense than seawater and depleted in chloride and enriched in volatile components. Hence, chloride concentration is an important indicator of fluid modification by phase separation, and the degree of modification depends on the temperature and pressure at which the fluid phase separates (Bischoff and Pitzer, 1989). Chloride also exhibits controls on mineral solubility via aqueous complexes, ionic strength and charge balance (Seyfried and Ding, 1995). Thus, phase separation profoundly impacts not only the chloride concentration but also the composition of hydrothermal fluids in general. The effects of phase separation have been observed in several deep sea hydrothermal systems including the Main Endeavour Field (MEF) on the Juan de Fuca ridge (Butterfield et al., 1994; Lilley et al., 2003; Seewald et al., 2003 Seyfried et al., 2003), and have been shown to vary over time (Von Damm et al., 1997; Von Damm, 2000) and space (Butterfield et al., 1990).

Conventional oceanographic research at deep-sea hydrothermal systems to date has relied upon ship based sampling and submersible observations, but this approach is limited to the relatively brief periods during which research vessels are able to remain on location and collect samples. The method of discrete sampling, while providing pertinent information about long term dynamics, does not adequately characterize the variability of mid-ocean ridge (MOR) hydrothermal systems on shorter timescales. Such a characterization requires the use of in-situ instruments capable of measuring the chemical properties of high temperature vent fluids at high sampling rates over extended time periods.

There are existing in-situ temperature measurements of high temperature fluids (Fornari et al., 1998; Tivey et al., 2002). Sample collection devices also exist for time series sampling of low temperature fluids (Wheat et al., 2000; Butterfield, 2001), but the composition of these samples reflects end-member dilution and a low temperature reaction overprint (Butterfield et al., 2003), and it is difficult to infer anything about the effects of phase separation under these circumstances. Ding and Seyfried (2001) and Ding et al., (2005) have successfully deployed an instrument in low and high temperature fluids at the Main Endeavour Field (MEF) to measure H_2, H_2S and temperature for periods of time ranging up to several days. In this chapter, we discuss an instrument that enables us to continuously measure conductivity as a proxy for chloride concentration in high temperature fluids, a measurement not possible with previous in-situ instruments. To date our instruments have been deployed for up to 2 months. The sensor measures the electrical resistance of the vent fluid as a proxy for salt content of the fluid, and data gathered thus far have been useful in providing information about the effects of phase separation on vent fluid at the MEF on the Juan de Fuca ridge

2. Instrument Description

Resistivity data were collected with a newly developed instrument that includes a sensor, sensor housing (the wand) and electronics package and its housing.

2.1. Sensor and Wand

The resistivity sensor is composed of gold spheres pressed into the end of a magnesium stabilized ZrO_2 ceramic rod to produce a smooth circular face with four circular gold electrodes (Figure 1). In all but 2 sensors, the gold/ceramic seals maintained their integrity for at least 2 months at a pressure of ~220 bar and temperatures ranging from 365 to 380°C. The sensor extends un-protected from the wand into the surrounding fluid allowing measurement of the fluid's resistivity. Ceramic-insulated wires extend

from the electrodes back through a pressure compensated titanium wand into a reservoir of non-conductive oil within a Tygon-tube. The wires terminate in an electrical feed-through that connects to 10 ft. of deep-sea cable. The wand is composed of grade 2 titanium tubing that enables the introduction of a bend of ~90°, which protects the back end from exposure to high temperature fluid. A type K thermocouple sheathed in 1/16" titanium tubing is positioned within ~ 1/4" of the sensor on the outside of the wand and held in place by titanium wire is. The thermocouple terminates in a polyurethane boot containing a reference thermistor. The wires from theses two temperature monitoring devices feed into another 10 ft. length of deep-sea cable.

2.2. Pressure Case and Electronics

The 10-ft. temperature and resistivity cables extend to an electronics package housed in a titanium pressure case. Signal generation, data acquisition and system control electronics were designed and assembled by the University of Washington Ocean Engineering Services group. Components were chosen for low power consumption. Power and data storage considerations allowed sampling rates up to 12 hr^{-1} during two-month deployments. All signals were digitized as 12 bit voltages. Two of the four gold electrodes are connected to 'drive' terminals on the electronics package and the other two are connected to 'sensor' terminals. The drive electrodes establish an electric field across a packet of fluid, which behaves as a resistor, by sending a constant alternating current of 100 uA at 1 kHz across a 10 kΩ resistor. The resistance of the fluid is dependent on its temperature and salt content (Smedley, 1980) and is measured by monitoring the potential difference across two sensor electrodes immersed in the fluid (Figure 1). This setup is accomplished with a constant current AC drive signal and a synchronously demodulated measurement of fluid resistivity between sensor electrodes. This method of averaging the voltage reading from the equivalent segment in each cycle of a block of 10 cycles in the AC signal enhances the signal/noise ratio.

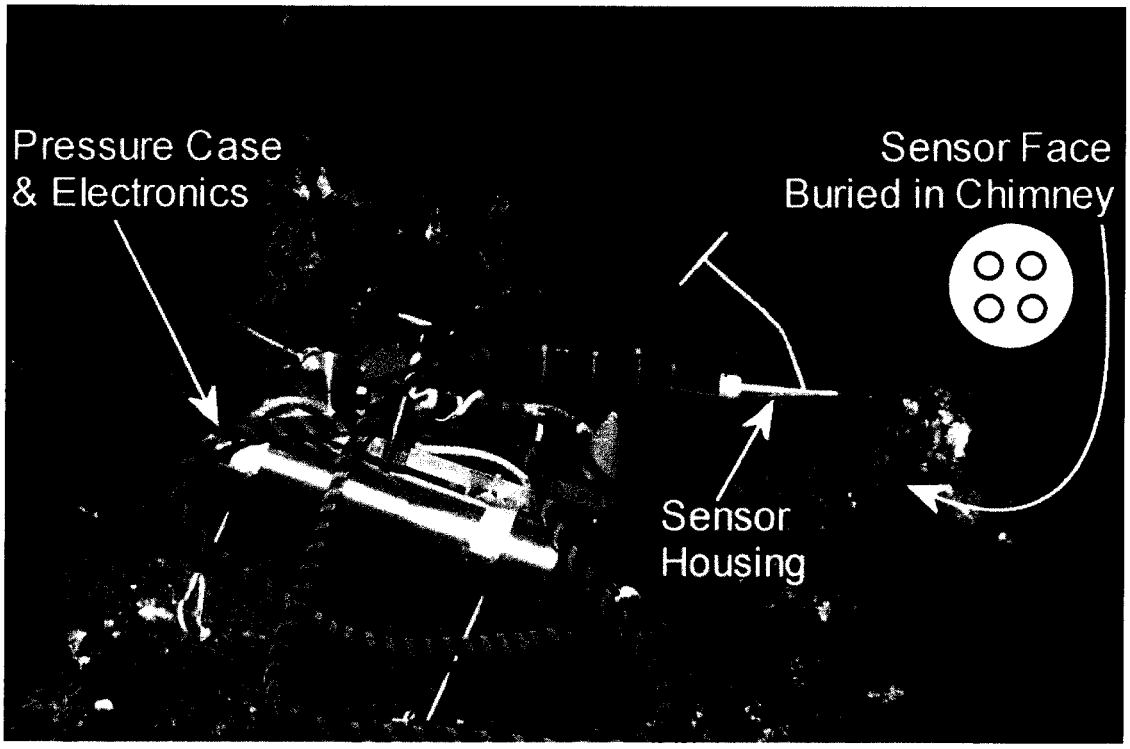

Figure 1. Resistivity-temperature probe deployed at Sully Vent showing the various components including a plan view schematic of the sensor face

2.3. Data Output

As the saline fluid behaves as a resistor, Ohm's Law can be applied to the solution. The relationship between the reciprocal of the probe output, in V^{-1}, and the specific conductance, κ in $ohm^{-1}cm^{-1}$, is given by the following equation:

$$(1) \quad \frac{1}{V} = \left(\frac{1}{I \times \theta} \right) \times \kappa$$

where the cell constant, θ, describes the specific dimensions of a given measurement and is calculated as the ratio of the path length of the measurement, ℓ, to the cross sectional surface area, A (Smedley, 1980). The relationship between V^{-1} and κ is linear if the current, I, and θ are constant (Figure 2). Although the data in Figure 2 are not in the

pressure and temperature range of hydrothermal conditions, they cover the expected range in chloride concentrations. Data shown in Figure 2 also demonstrate that the linear correlation between the instrument readings and conventional conductivity data holds true for concentrated NaCl solutions that do not necessarily obey equations relating conductivity to salt content. For the purpose of simplification, the reciprocal of our instrument's raw data in units of V^{-1} will be hereafter referred to as conductivity.

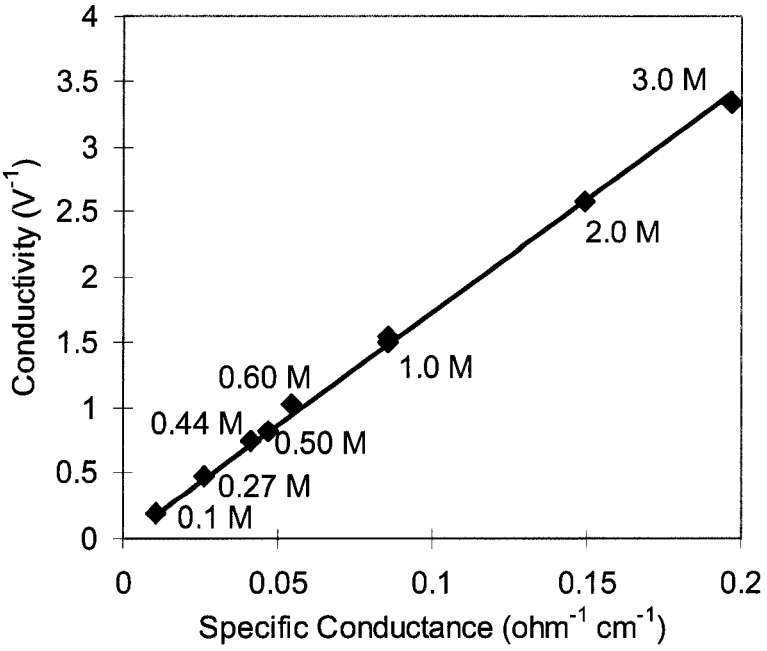

Figure 2. Reciprocal of probe voltage vs. literature specific conductivities for NaCl solutions from 0.1 M to 3.0 M at room temperature and pressure. Specific conductance data are taken from Currie & Gordon (1960) and Bianchi et al. (1989).

3. Laboratory Calibration

3.1. Calibration Apparatus

Hydrothermal conditions were simulated for purposes of sensor calibration using the apparatus shown in Figure 3. The pressure compensation provided by the Tygon tube on the field instrument is replicated in the calibration apparatus by a pair of 1/8 inch

stainless steel coils (one filled with oil, the other with water) and a 3-way connector. This system requires only a single pressure source and pressure regulator and generates equal pressure on the front and back side of the sensor.

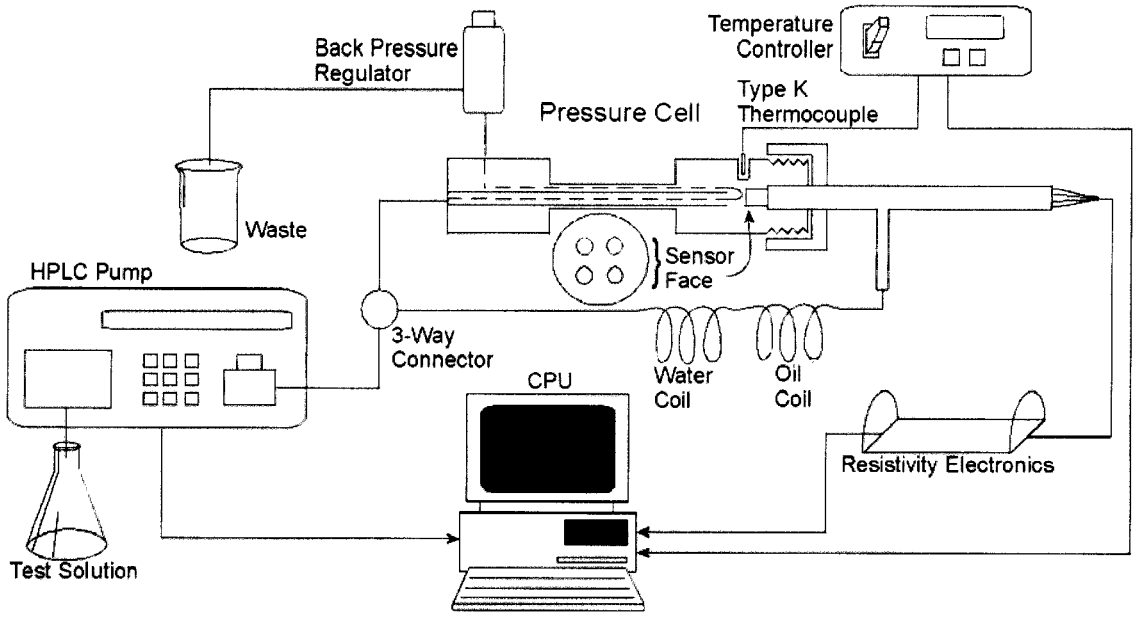

Figure 3. Schematic of experimental setup. See text for discussion.

3.2. Uncertainty in Calibration Experiments

The uncertainty of the conductivity measurement was estimated by using 3 different sensors to make a total of 7 duplicate measurements on a variety of solutions spanning the range of experimental temperature, pressure and composition. For experimental time spans $\leq$ 15 hours, the range of values was no greater than $\pm$ 1.1% of the average for any given sensor and set of experimental conditions. For experimental time spans up to 70 hours, the range was $\pm$ 10.2%. Maximum standard deviation of temperature measured in lab experiments was $\pm$0.1 °C.

Although the uncertainty measured in the lab on longer timescales is comparable to observed changes in the field data on the same timescales (Section 4), comparison of chloride concentrations from pre and post deployment fluid samples with initial and final

conductivity readings, respectively, suggests that drift in the field is minimal (see section 4.2.2). We attribute drift in lab experiments to problems with the pressure compensation components of the laboratory calibration system. We sometimes noted oil on the electrode surface, a likely result of leaks induced by intermittent pressure gradients across the electrodes.

3.3. Fluid Parameters Affecting Conductivity

3.3.1 Salt Content

The main controlling factor of fluid conductivity is the salt content of the fluid. In vent fluids, NaCl is the dominant salt (Butterfield et al., 1994). In experiments we conducted at constant temperature, the dependence of conductivity on NaCl concentration is linear, e.g., for temperatures ranging from 20 °C to 380 °C and for NaCl concentrations ranging from 54 mmol/kg to 3 mol/kg; (Figure 2 &Figure 4a).

3.3.2 Temperature

The second most influential factor affecting fluid conductivity is temperature. The dependence of conductivity on temperature is more complex than the dependence on salt content and exhibits a nonlinear functionality with a conductivity maximum at temperatures ranging from approximately 250 °C for a 634 mmolal NaCl solution to 280 °C for a 54 mmolal NaCl solution (Figure 4b). The temperature range of maximum conductivity is similar to that determined by Quist and Marshall (1968) for more dilute solutions at higher pressures. There is some variation in the temperature of maximum conductivity with the addition of other cations, but the temperatures of most black smokers put the fluids in the section of the calibration curve in which conductivity decreases with increasing temperature.

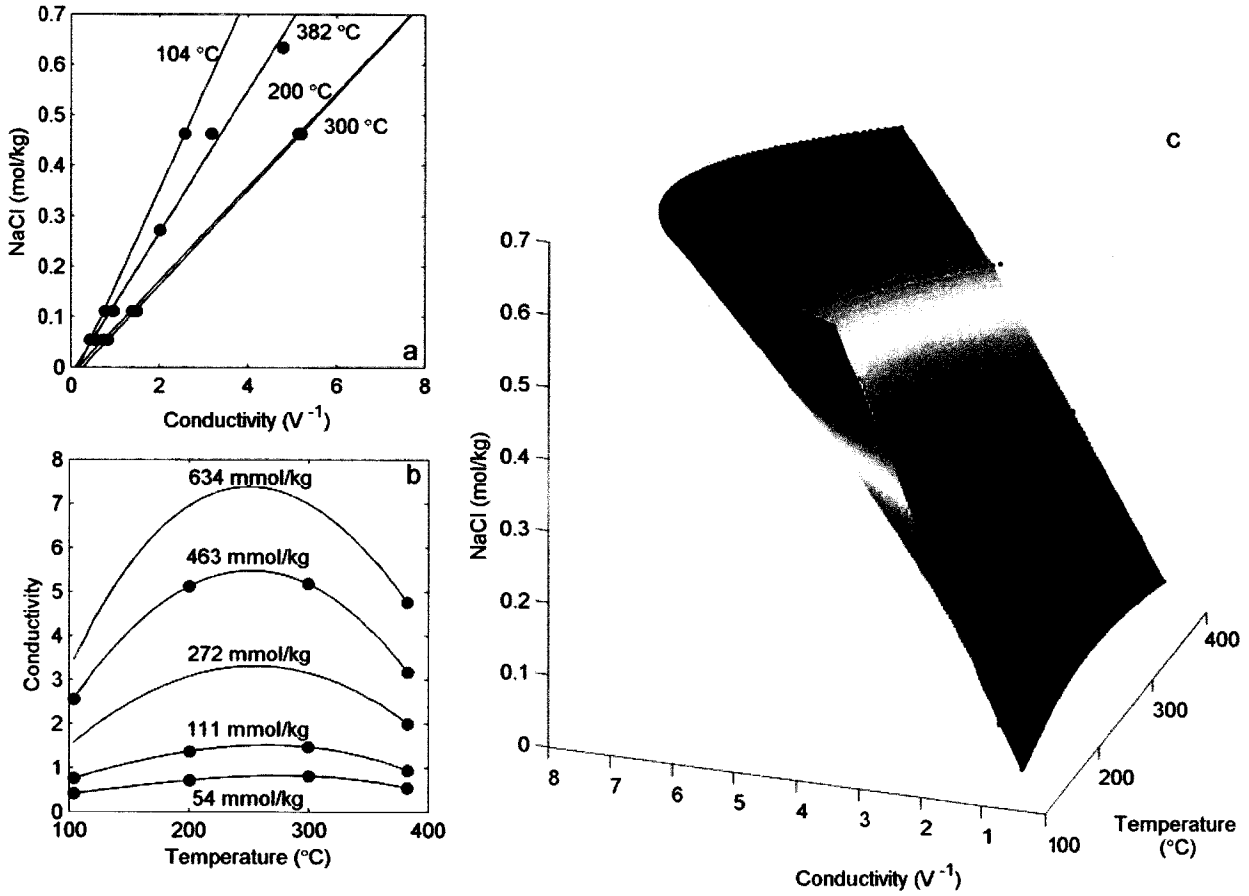

Figure 4. Laboratory generated calibration data at 220 bars with the exception of the 382 °C data which was collected at 300 bars. (a) Chloride vs. conductivity at constant temperature. (b) Conductivity vs. temperature at constant chloride. The 272 mmol/kg and 634 mmol/kg isopleths in the range of 104 -300 °C are interpolated from surrounding data. (c) Surface depicting relationship between calculated NaCl, temperature and conductivity.

3.3.3 Functional dependence of conductivity on temperature and salt content

Conductivity as a function of the two dominant factors, temperature and salt content, is depicted in Figure 4c. The functional dependence of conductivity on temperature was interpolated from experimental data along planes of constant salt concentration using piecewise cubic interpolation (de Boor, 1978). A surface was fit to the resulting two-dimensional curves using the Matlab function 'griddata' which relies on the method of Delaunay triangulation to create a triangular irregular network (Barber et al., 1996). The surface so created provides unique values of conductivity for a fluid with given temperature and NaCl content. Thus, each NaCl (mmol/kg)-temperature (°C) pair can be translated to a unique value for the conductivity (V^{-1}). Similarly, a unique value of NaCl content can be calculated from measurements of conductivity and temperature.

3.3.4 Normalization of conductivity readings to fluid sample data

A complicating factor of the calibration process is that conductivity measurements depend, in part, on the surface area of the electrodes. Variation inherent in the fabrication process results in differences in electrode surface area for different sensors. Such differences, while significant, can be accounted for by pre-deployment calibration or by normalization to chloride concentrations in fluid samples collected before and after sensor deployments. This normalization is accomplished by pairing the first and last conductivity (C_{field})-temperature (T_{field}) readings for each data record with the chloride concentrations (S_{field}) for pre-deployment and post-recovery fluid samples respectively. S_{field} and T_{field} are also paired with their associated conductivity value (C_{lab}) from the calibration surface. Using C_{field} and C_{lab}, a scale factor, f, can be calculated for the beginning and end of each data record:

$$(2) \quad f = \frac{C_{lab}}{C_{field}}$$

Each data point is multiplied by the average scale factor for that deployment prior to conversion to calculated NaCl. In this way, fluid samples are used to anchor each end of a data record to independent laboratory determined chloride measurements. In general, these samples are taken within ~20 mins of the placement or removal of a sensor. On this timescale, tidally driven changes in chloride are less than 2 mmol/kg. Non-tidal changes could be larger and occur more quickly but even the large rapid changes we observe in this data set take place on the scale of hours (see discussion of data below). Thus, we can reasonably make comparisons between pre and post deployment fluid samples with initial and final in-situ measurements.

Scale factors calculated with this procedure are in good agreement at the beginning and end of each data record indicating minimal instrument drift over the length of each deployment (Table 1). Differences between scale factors for any given deployment are less than the 2-3% uncertainty for end-member concentrations calculated from extrapolations of chloride measured in fluid samples to zero Mg. We conclude, therefore, that the relationship between chloride and conductivity is constant throughout the life of the deployment within our ability to detect any change. Calculated NaCl obtained from normalization to fluid sample data as described above will be used in presenting the field data (section 4.2).

Table 1. Scale factors used to normalize field data to fluid sample chloride concentrations. Differences in scale factors are an indicator of instrument drift. Uncertainty in end-member chloride is 2-3%

Vent, deployment #	Sample type	End-member chloride (mmol/kg)	Scale Factor (f)	Calculated NaCl
Milli-Q, # 1	pre-deployment	350	1.380	346.5
	pre-deployment	344	1.359	
Milli-Q, # 2	pre-deployment	358	1.348	358.4
	post-recovery	384	1.354	382.5
Grotto, # 1	pre-deployment	458	0.774	456.7
	post-recovery	444	0.768	446.5

3.3.5 Cation composition

Although salt content and temperature have the most significant impact on conductivity, other factors influence the conductivity of hydrothermal fluids. The most important factor considered besides NaCl concentration and temperature is the ionic composition. In high temperature hydrothermal fluids of interest, chloride is the dominant anion, and other anions are present in trivial amounts (less than 1 mmol/kg). Although sodium is the dominant cation at MEF, ranging from 260 to 391 mmol/kg, K^+ and Ca^{2+} are present in concentrations ranging up to 29 mmol/kg and 43 mmol/kg respectively (Butterfield et al., 1994, Table 3).

A cation replacement experiment was performed with potassium at 22°C and 1 atm. Conductivity increases with increasing mole fraction of K^+ (Figure 5) from 0.75 V^{-1} for a 440 mmolal NaCl solution to 0.97 V^{-1} for a 440 mmolal KCl solution. This observation is in agreement with data from Currie & Gordon (1960), and reflects the higher specific conductance of K^+ with respect to Na^+ for a given equivalent concentration (Table 2). Experiments on 10 mmolal NaCl and KCl solutions by Quist & Marshall (1969) at 500 bars and 300°C and 400°C show that the difference in conductivity between a NaCl solution and a KCl solution is less than the change we observe at atmospheric conditions.

Table 2. Equivalent conductance and concentration range in MEF fluids for relevant ions (Butterfield et al., 1994, Table 3; Vanýsek, 2005)

Ion	Equivalent Conductance x 10^{-4} (m^2 Ω^{-1} equiv.$^{-1}$)	MEF Concentration Range (mmol/kg)
Na^+	50.08	200 – 400
Ca^{+2}	59.47	10 – 40
K^+	73.48	10 – 40
H^+	349.65	$10^{-4} – 10^{-7}$
Cl^-	76.31	10-700
OH^-	198	$10^{-7} – 10^{-11}$

A calcium cation replacement experiment at pressures up to 220 bar and temperatures up to 300°C demonstrated a decrease in conductivity with increasing mole

fraction of Ca^{2+} (Figure 5). These observations are consistent with data from Quist and Marshall (1968) and Frantz and Marshall (1982) for NaCl and $CaCl_2$ solutions respectively. As with K^+, Ca^{+2} has a higher equivalent conductance than Na^+, but dissociation constants calculated by Quist and Marshall (1968) and Frantz and Marshall (1982) suggest $CaCl_2$ is more likely to form non-conducting ion pairs than NaCl at higher temperatures and pressures. As a result, the conductivity for a $CaCl_2$ solution will be lower than for a NaCl solution with the same chloride concentration. The magnitude of the conductivity decrease in our experiments grows slightly with temperature from 100°C to 300°C (Figure 5). The effect of cation replacement on our field conductivity measurements can be calculated for the maximum levels of Ca^{+2} and K^+ in the MEF fluids using the slopes of the appropriate isotherms from Figure 5.

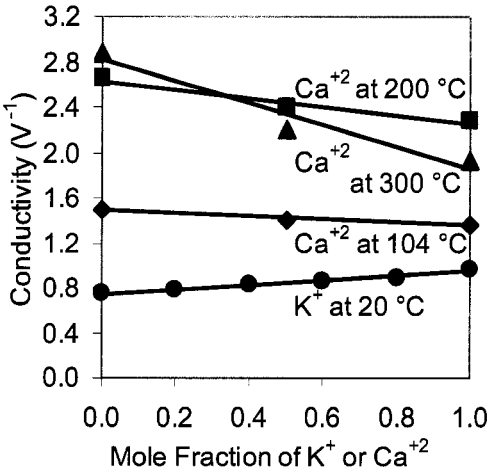

Figure 5. Effect of replacement of Na^+ with K^+ in a 440 mM chloride solution at 21 °C and atmospheric pressure and effect of replacement of Na^+ with Ca^{+2} in a 271 mmol/kg chloride solution at 220 bar.

The results of these calculations suggest that for the concentrations of Ca^{+2} and K^+ in MEF hydrothermal fluids, the difference in conductivity resulting from a change in the cation composition from a pure NaCl solution to a composition similar to MEF hydrothermal fluid is about -3% of the measured value for Ca^{+2} and about +3% for K^+ (Table 3). It should be noted that most fluids sampled at MEF contain both Ca^{+2} and K^+

with Ca:K ratios ranging from 1 to 1.6 (Butterfield et al., 1994) such that the effect of each ion on conductivity will tend to cancel out the effect of the other. Thus, in the context of conductivity, it is reasonable to model the ionic composition of hydrothermal fluid as pure NaCl.

Table 3. Summary of cation replacement experiments

Parameter/quantity of interest	Ca^{+2}	K^{+}
Chloride concentration (mmol/kg)	272	440
Solution temperature (°C)	300	20
Conductivity for pure NaCl (V^{-1})	2.89	0.75
Maximum mole fraction in MEF fluids of indicated cation	0.1	0.1
Conductivity for solution with sodium and maximum amount of indicated alternate cation (V^{-1})	2.79	0.77
Percent difference from pure NaCl solution	-3.3%	+2.7%

3.3.6 Pressure and density

Fluid conductivity is also dependent on pressure due to changes in fluid density. Decreasing density at lower pressures results in a decrease in the density of charge carriers (the Na^{+} and Cl^{-} ions), increased ion pairing as the dielectric constant of water decreases, and an increase in ion mobility as viscous drag is reduced (Quist and Marshall, 1968). The first two processes result in a decrease in fluid conductivity while the third results in an increase. Thus, it is important to determine if these processes have a significant effect on conductivity. To this end, experiments were performed at constant temperature and NaCl concentration and variable pressure (Figure 6).

The magnitude of these effects on conductivity for pressure fluctuations at MEF can be calculated using seafloor pressure data from this region. Data collected by a bottom pressure recorder show that the maximum range in water column height at MEF during the instrument deployments is 4.5 meters. The pressure change associated with this variation in water column height is 0.44 bars.

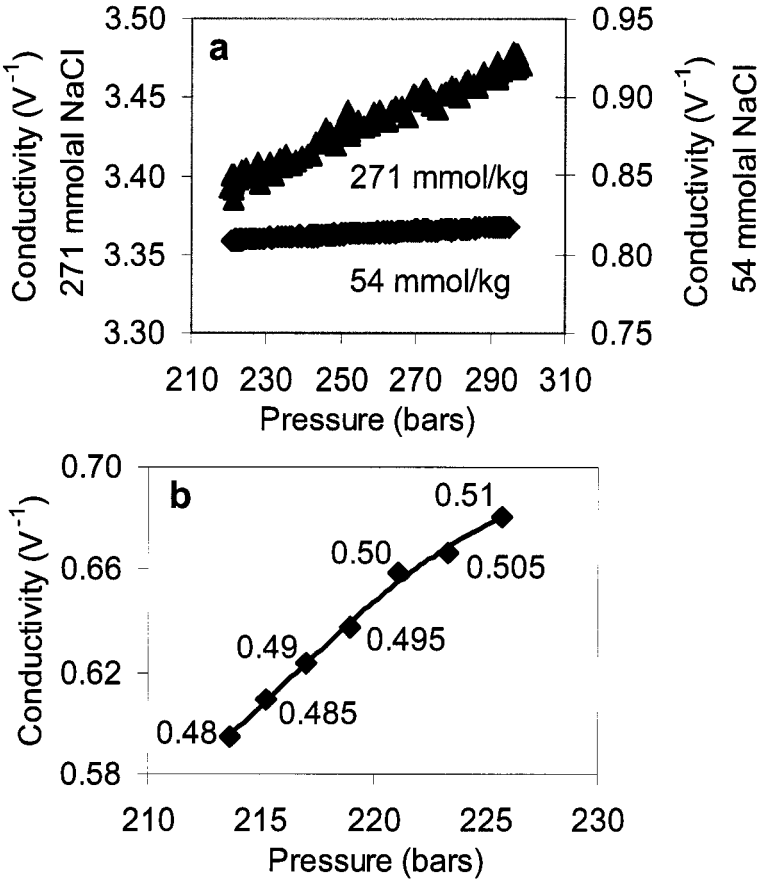

Figure 6. Effect of pressure on conductivity. (a) Conductivity vs. pressure for 271 and 54 mmolal NaCl solutions at 300°C. (b) Conductivity vs. pressure for a 100 mmolal NaCl solution at 370°C calculated using data from Quist & Marshall (1968) and Anderko & Pitzer (1993). Data labels indicate densities of the solution in g/cm^3 at the given pressure.

Using the slope of the line for the more concentrated solution from Figure 6a, the increase in conductivity for this magnitude of pressure change is on the order of 10^{-4} V^{-1}, which is equivalent to a change of 20 μmol/kg. This effect is well within the uncertainty of the measurement. Based on these experiments, we conclude that the dependence of conductivity on pressure at the temperature and pressure of MEF hydrothermal vents is negligible for dilute solutions and very slight for more concentrated solutions (see below and Figure 6b).

One caveat to these experiments is that they were performed at temperatures and pressures well away from the two phase boundary of the NaCl-H_2O system. As a result, the data do not extend above 300°C or below 220 bars. A comparison of density calculations performed at 370°C using the Anderko and Pitzer (1993) equation of state for NaCl-H_2O with data from Rogers & Pitzer (1982) for 300°C shows that density exhibits a smaller dependence on pressure under these laboratory temperatures and pressures than under the field conditions at MEF where the temperature is higher. However, we can calculate the magnitude of the change in conductivity resulting from a change in pressure at temperatures close to the two phase boundary for solutions ranging up to 100 mmol/kg NaCl, which is the maximum concentration considered by Quist & Marshall (1968). First, the dependence of specific conductance (κ) on pressure at the desired temperature can be extrapolated from data collected by Quist and Marshall (1968). The specific conductance can then be converted to our conductivity measurement using the cell constant, and density can be related to pressure for a given NaCl concentration using the Anderko and Pitzer (1993) equation of state (Figure 6b). This plot can then be used to determine the change in conductivity for a given change in pressure. For a 100 mmolal NaCl solution at 370°C, a change in pressure of 0.44 bars would produce a 0.004 V^{-1} (0.6%) change in conductivity. For more concentrated solutions, such as those at MEF, this effect will be less significant (Quist & Marshall, 1968). Thus, tidal pressure oscillations have a minimal direct effect on fluid conductivity at the MEF.

3.3.7 pH

Experimental results demonstrate only a slight dependence of conductivity on pH below pH 7, with a maximum in conductivity at ~ pH 5. This dependence decreases with increasing temperature and is nearly non-existent at temperatures between 300 and 380°C (Figure 7). Although H^+ has a much higher equivalent conductance than any other ion considered here (Table 2), the effect of pH on conductivity is fairly small even for moderately acidic solutions due to the relatively low concentration of free H^+ ion

compared with Na^+. Results of this suite of experiments demonstrate that it is reasonable to use data collected on neutral NaCl solutions to extrapolate to more acidic and compositionally diverse solutions found in hydrothermal systems.

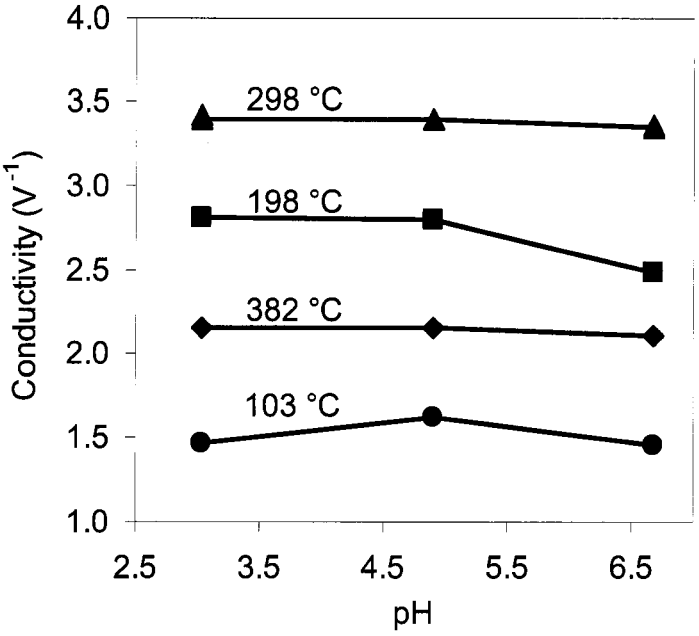

Figure 7. pH Dependence of Conductivity for 271 mmol/kg NaCl solution. In the temperature range of interest, effect of pH is smaller than measurement uncertainty. Experiment conducted at 220 bars with the exception of the 382°C data which was collected at 300 bars.

4. Field Data

4.1. Experimental Site

In the summer of 2000, two separate cruises were undertaken to the Main Endeavour Field (MEF) on the Endeavour segment of the Juan de Fuca Ridge. The Main Field at 47°57' N and 129°06' W is a vigorously venting basalt-hosted system located on the western wall of the axial valley (Delaney et al., 1992). Venting sulfide structures occupy a region about 350 m long and 180 m wide and increase in size and volume from the South to the North, with southern structures venting fluids hotter than those to the

North. Instruments were deployed at four different sulfide structures in the southern portion of the field and at one structure in the northern portion. Data discussed herein are the result of three separate resistivity probe deployments, two at a structure named Milli-Q residing in the southern portion of the vent field, and one at a structure named Grotto in the northern portion of the field. The resistivity data (Figures Figure 8, Figure 9, Figure 10 and Figure 11) are supplemented by chemical data from discrete fluid samples taken at these structures (Lilley et al., 2003) as well as sea-floor pressure data from a Paroscientific model 46K-101 pressure sensor that was deployed at MEF between the two structures. Some of the features of each data set are compared in tabular form (Table 4).

Table 4. Comparison of the experimental parameters and the data from the three resistivity probe deployments at the Milli-Q and Grotto vents. See text for discussion.

Vent/deployment #	Milli-Q #1	Milli-Q #2	Grotto #1
Deployment date	6/16/00	7/7/00	6/16/00
Recovery date	7/5/00	9/15/00	6/26/00
Length of deployment (days)	20	70	10
Avg. Cl^- for pre-deployment fluid samples (mmol/kg)	347	357	458
Avg. Cl^- for post-deployment fluid samples (mmol/kg)	357	384	444
Temperature range (°C)	363-367	358-370	358.4-359.5
Maximum peak-to-peak chloride oscillation (mmol/kg)	21	18	non-oscillating signal
Minimum peak-to-peak chloride oscillation (mmol/kg)	4	7	non-oscillating signal

4.2. Field Data

4.2.1 Milli-Q Vent, deployment #1

The full record of the first deployment at Milli-Q is shown in Figure 8 along with an enlarged portion of part of the record in Figure 9. The break in the pressure record beginning near the end of day 173 reflects the recovery of the pressure recorder for routine maintenance followed by redeployment the following day.

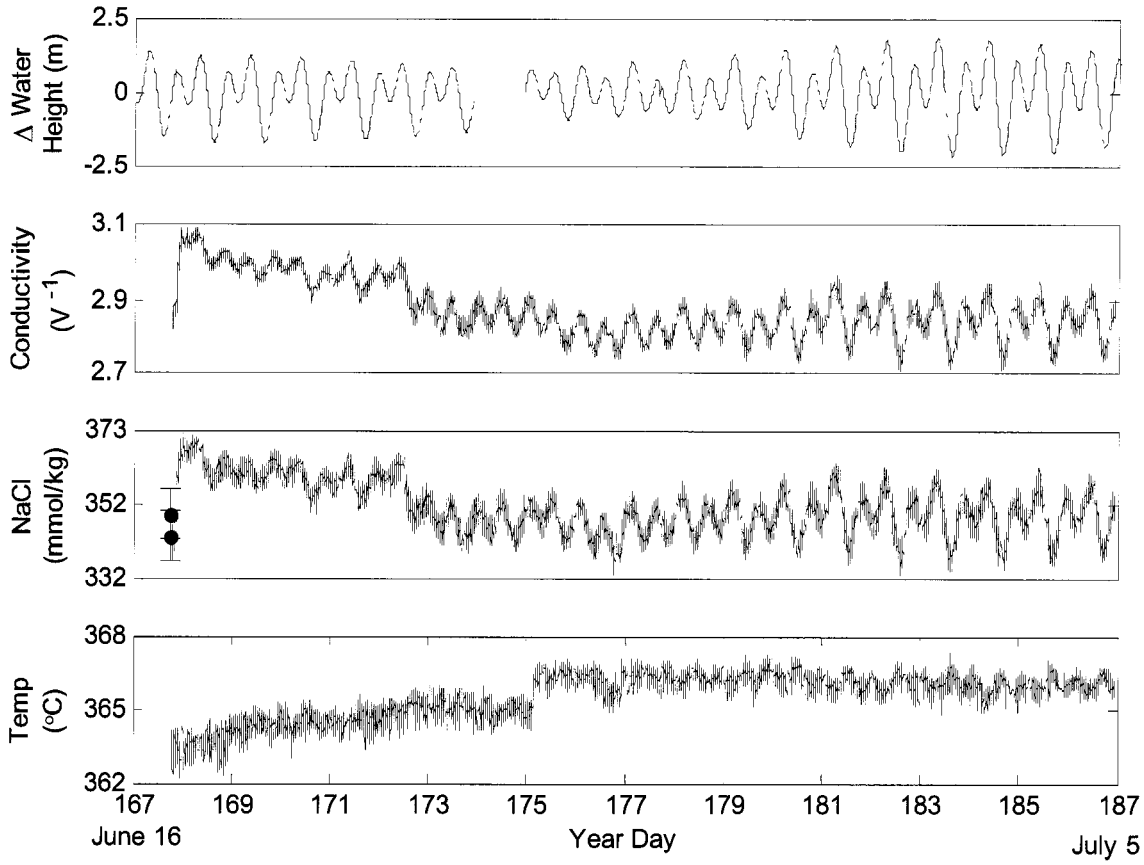

Figure 8. Data from the first of two instrument deployments at Milli-Q vent in the southern half of the MEF vent field. Δwater height is the difference in the height of the water column from the mean value.

After an initial jump, the mean conductivity value decreases from year day 168 to day 176 as the amplitude of the pressure oscillations decreases with the approach of the neap tides. The most striking features of this data record are the diurnal and semi-diurnal oscillations in both the temperature and conductivity records which correlate strongly in both frequency and amplitude with the tidally driven oscillations in pressure. Several investigators have observed a tidal influence on the temperature and other fluid parameters of diffuse hydrothermal effluent (Little et al., 1988; Kadko et al., 1994; Schultz et al., 1996; Tivey et al., 2002), but a lack of tidal influence has been reported for high temperature vent fluid effluent (Tivey et al., 2002; Scheirer et al., 2006). To our

knowledge, these are the first observations showing a tidal influence in high temperature vent effluent temperature and composition.

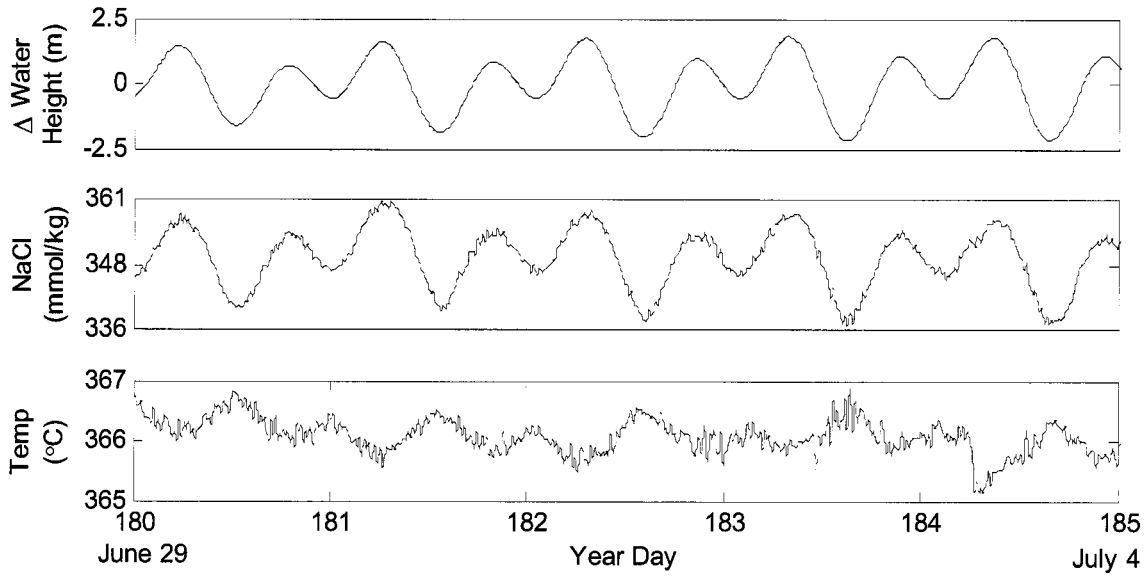

Figure 9. A blown-up 5 day segment of the data shown in Figure 8

The oscillations in conductivity and temperature are relatively small in amplitude at the beginning of the record during which time the pressure oscillations are relatively large. These oscillations remain fairly small in magnitude as the pressure oscillations diminish, but start to increase between year day 176 and day 177 as the pressure oscillations increase with the onset of the spring tides. Also during this time period, the mean temperature increases from 363.8 °C to 366.2 °C with a rapid 2 degree increase starting early in day 175 and occurring over approximately 90 minutes. After a more gradual decrease to 365.2, we see another jump in the mean temperature at the end of day 176 to 366.5 °C occurring over 16 mins followed once again by a more gradual decay, then another 1.3 °C jump 3 hours later to 366.7 occurring over 4 minutes. After this third offset, the mean temperature remains at a higher value for the remainder of the record.

4.2.2 Milli-Q Vent, deployment #2

A second resistivity probe was deployed at the same orifice on Milli-Q on year day 189.5 a few days after the first probe was recovered from there on year day 187 (Figure 10). It is interesting to note that although the data for these two deployments were collected by different probe assemblies, the average scale factors for the two sensors differ by only 1.4%.

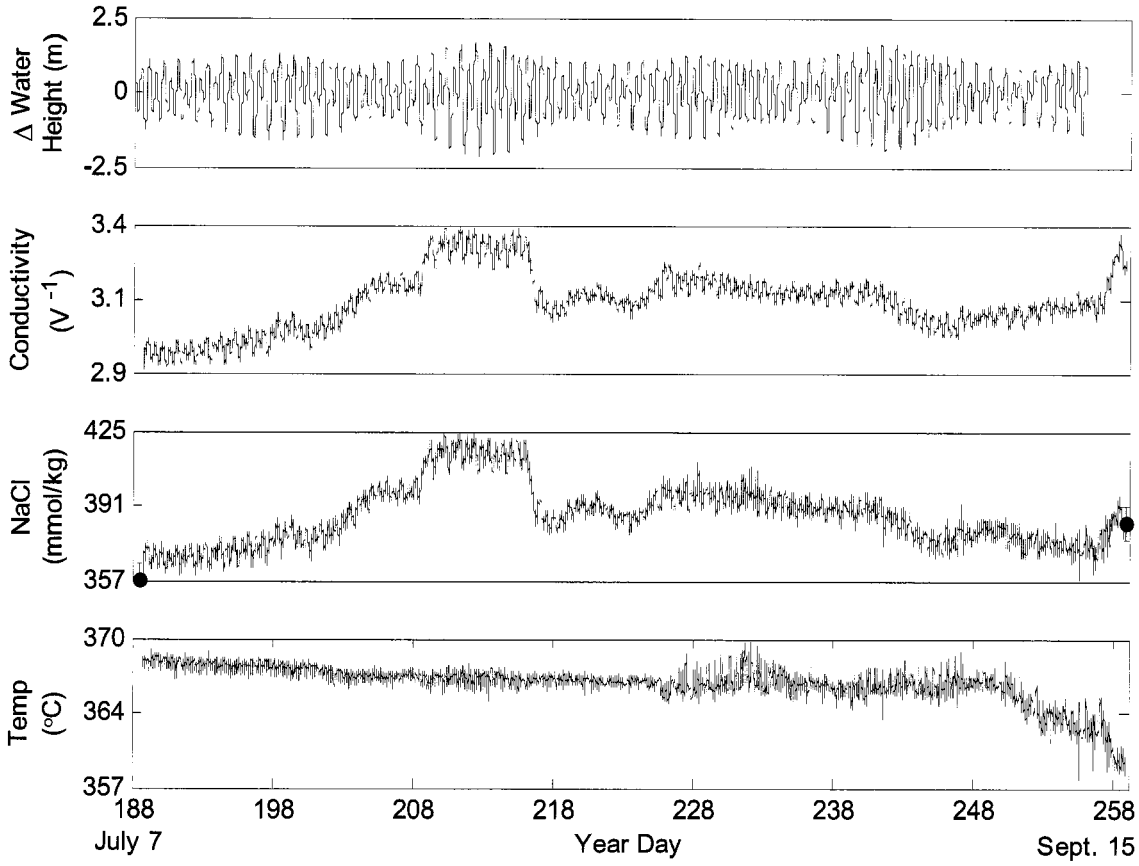

Figure 10. Data from the second of two instrument deployments at Milli-Q vent

The second deployment at Milli-Q represents a longer residence and a wider range in temperature and conductivity than the first Milli-Q deployment. The tidally correlated oscillations manifest themselves again in the conductivity signal with a phase angle of zero with respect to the pressure signal. As with the first Milli-Q data set, the

diurnal and semi-diurnal oscillations in conductivity correlate well in both frequency and amplitude with the pressure oscillations. Temperature oscillations for this record correlate well in frequency with pressure and conductivity oscillations but not as well in amplitude. The amplitudes are smaller in general than the first Milli-Q dataset and gone altogether for some periods of time. Between days 217 and 223, tidal temperature oscillations are dampened beyond our ability to measure them (see supplemental data).

Several other features of this record deserve mention as well. During the onset of the period of maximum oscillation in pressure just after year day 208, there is a rapid increase in the mean conductivity value of about 0.2 volts^{-1} occurring over ~7 hrs which would correspond to an increase in chloride from ~390 mmol/kg to ~ 409 mmol/kg. It should be noted that the change of 0.2 V^{-1} is nearly 10% of the conductivity value at the time of the increase which is notably larger than both the drift measured in the field over 70 days (discussed below) and the ±1.1% of uncertainty measured in the laboratory for the same timescales. Thus, this trend likely reflects actual changes in vent fluid composition. During the next nine days, the amplitude of the conductivity oscillations is also slightly larger than before the jump. Following this nine day period, there is a decrease in the mean conductivity from 3.1 V^{-1} to 2.9 V^{-1} (corresponding to a change in NaCl from ~409 mmol/kg to ~380 mmol/kg), which is lower than the value before the jump. This decrease occurs during the decrease in the amplitude of the pressure oscillations from their maximum to their minimum amplitude. The conductivity remains at this lower value from year day 217 to day 224 during which time, the amplitude of pressure oscillations is at a minimum. As the amplitude of the pressure oscillations increases slightly after the period of minimum oscillation, the mean chloride concentration rebounds close to the initial value before the increase at year day 208.

The temperature for the second deployment exhibits an overall decrease, from ~368 °C at the beginning of the record to ~358 °C at the end of the record, compared to a general increase in the first deployment. The rate of temperature decrease becomes greater at about year day 250 just as conductivity exhibits an increase. The rate of the

temperature drop increases yet again at day 257 coinciding with a change in the rate of the conductivity increase. Chloride concentration measured from water samples taken at recovery was 384 mmol/kg which is 27 mmol/kg higher than the concentration measured at the deployment. This is consistent with the chloride trend observed by the resistivity probe which gave calculated NaCl values of 359 and 383 mmol/kg for the start and end of the record respectively.

In considering the conductivity oscillations, it should be noted that conductivity changes result from changes in both density and in NaCl concentration per unit mass. However, the maximum peak-to-peak change in conductivity for the two Milli-Q deployments ranges from 4.4% to 6.0%, and changes in density might account for only about 0.6% of this fluctuation as discussed earlier. Thus, the oscillations likely represent actual changes in the salt content of the fluid per unit mass and not just in the volumetric concentration. However, the magnitudes of these chloride oscillations should be considered maximum values since the component of the oscillation attributable to density changes can not be accounted for over the entire range of vent fluid compositions and temperatures encountered here.

For changes on longer timescales discussed in the second Milli-Q data set (Figure 10), it should be noted that we observe good agreement between scale factors calculated at the beginning and end of the deployment (Table 1). If we use the scale factor calculated at the beginning of the data record to determine the chloride measured by the probe at the end of the record, we calculate a value at recovery of 382 mmol/kg. This value differs by only 0.5% from the chloride measured in the fluid sample taken at recovery, 384mmo/kg. This agreement indicates that the relationship between temperature, conductivity and calculated NaCl is fairly constant over time such that long term trends in calculated NaCl reflect actual changes in vent fluid composition, not drift in the conductivity reading. This conclusion is consistent with the fact that we did not observe any signs of processes such as erosion or precipitation on the surface of the sensor which is deployed 8" to 10" down within the chimney (Figure 1) where

precipitation due to seawater entrainment is much less significant than at the vent orifice (Goldfarb et al., 1983; Tivey et al., 1990).

4.2.3 Grotto Vent

The data collected from Grotto (Figure 11) show that Grotto fluid is as much as 12 °C cooler in temperature and about 66-117 mmol/kg higher in chloride than Mill-Q. Furthermore, neither temperature nor conductivity at Grotto exhibit a tidal component. Mean calculated NaCl concentration increases from year day 169.5 to 174.5 coinciding with a slight decrease in the amplitude of the pressure oscillations. This increase terminates in a chloride maximum of 483 mmol/kg and is followed by a decrease in chloride.

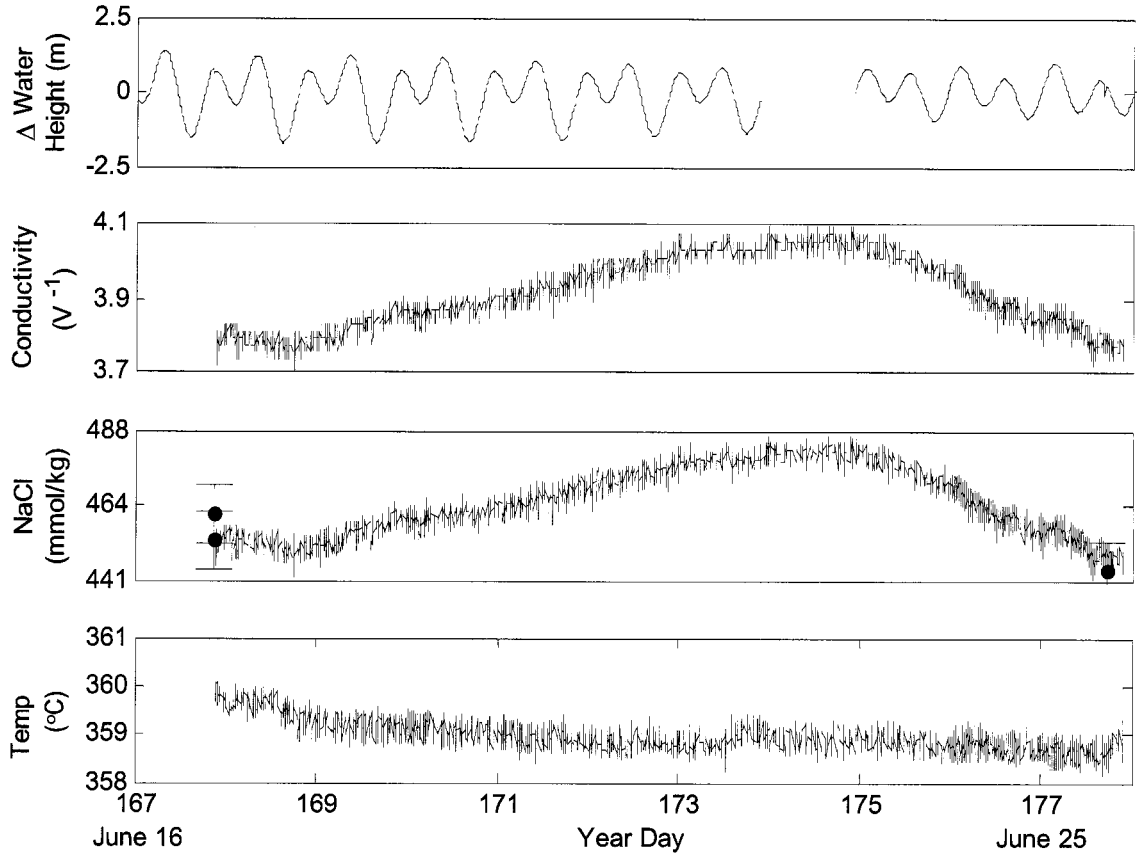

Figure 11. Data from an instrument deployment at Grotto vent in the northern half of the MEF

The temperature during this deployment at Grotto exhibits a slow but steady decrease from 359.2 °C to 358.4 °C, with a small jump in temperature at day 173.5 of ~0.6 °C corresponding to a small dip in chloride of about 9 mmol/kg. Other than this minor excursion, there are no significant or recurring deviations from the mean temperature.

5. Discussion

5.1. Changes on Tidal Timescales

5.1.1 Calculated NaCl correlates well with pressure data

Striking features of the Milli-Q results include oscillations in temperature and chloride that correlate well with tidal oscillations in seafloor pressure. Fourier analysis of pressure and chloride data demonstrates that the four strongest peaks in the frequency domain for Milli-Q chloride and pressure data are identical and represent the S2 and M2 semi-diurnal tidal peaks and the O1 and K1 diurnal tidal peaks (Figure 12). Visual inspection suggests there is no phase lag between the two sets of data (Figure 9). However, calculations using T_TIDE, a tidal analysis software package (Pawlowicza et al., 2002), show that for the M2 tidal constituent, the constituent with the greatest power in the Fourier analysis of Milli-Q (Figure 12), chloride oscillations are shifted by 13° with respect to pressure which equates to a 56 minute lag. Such a shift would not be readily apparent visually for the peak resolution and sampling rate of our data. Given the fact that chloride oscillations likely reflect subsurface processes as discussed below in section 5.1.2., the phase lag calculated by T_TIDE is consistent with numerical modeling results which show that depending on properties of the crust, subsurface pressure perturbations may lag seafloor pressure oscillations (Crone and Wilcock, 2005).

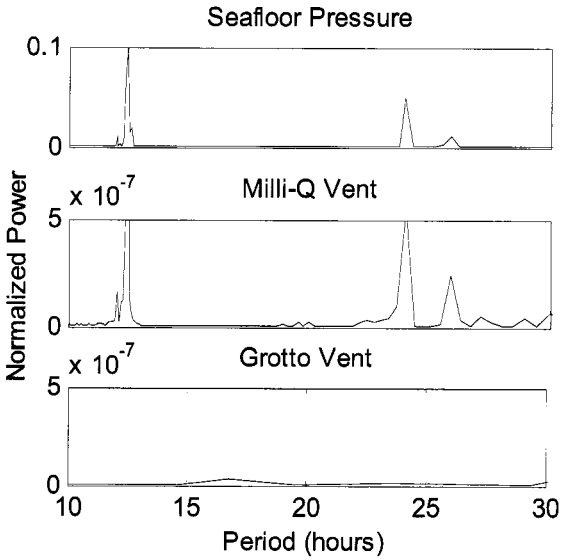

Figure 12. Fourier analysis of seafloor pressure and Milli-Q and Grotto calculated NaCl. The Fourier transform of each data record is computed with the Matlab 'fft' function. Each element of the resulting vector is multiplied by its complex conjugate and normalized to the length of the vector squared. This normalized power is plotted against the inverse of the constituent frequencies.

5.1.2 Seafloor observations reflect subsurface processes

Other investigators have observed tidal modulation of fluid temperature (Kinoshita et al., 1998; Tivey et al., 2005) and flow velocity (Schultz et al., 1996) in diffuse fluids. Some studies attribute the tidal influence on fluid temperature to bottom currents that vary in time with seafloor pressure and change the amount of seawater mixed with buoyant vent fluid exiting the chimney. (Kinoshita et al., 1998; Tivey et al., 2002). However, there is other evidence that the dominant controls on variations in hydrothermal flow are subsurface processes modulated by tidal changes in the pressure of the hydrothermal system (Schultz et al., 1996; Crone and Wilcock, 2005). This latter scenario, that of a subsurface process signature, is the one most consistent with our own observations.

Turbulent mixing at a chimney orifice between hot end-member vent fluid and cold seawater (also called seawater entrainment) results in fluid flow that is spatially heterogeneous such that conductivity and temperature measurements made at a fixed

point within the mixing zone will reflect spatial heterogeneity as temporal variability. If the oscillations in temperature and chloride were due to variable seawater entrainment controlled by bottom currents or pressure fluctuations, we would expect the oscillations to be evident in both the Grotto and Milli-Q fluid chemistry as both vents have end-member fluid compositions that differ measurably from seawater (Table 4). However, there is no tidal signature in the Grotto dataset suggesting the tidal signature at Milli-Q is generated deeper within the crust. However, even if we do assume tidal temperature changes are due to seawater dilution of a hydrothermal end-member at the vent orifice, the associated chloride changes would be too small to explain our observations. As an example, we calculated the expected change in chloride during a half tidal cycle for Milli-Q using the increase in pressure midway between day 181 and 182. During this time, Temperature decreases from 366.3°C to 366.0°C which gives a required mass fraction of seawater of 8 $x10^{-4}$. Using this ratio to calculate the change in chloride gives less than 1 mmol/kg compared to a change in NaCl based on conductivity of 18 mmol/kg.

Although the oscillations do not appear to be due to linear mixing with seawater, we do note a linear trend when chloride concentration is plotted vs. temperature for a five hour section of the Milli-Q data about a third of the way through day 181 (Figure 13). The line through the data has a significantly different slope than the seawater entrainment line, suggesting there is another process at work. Based on the temperatures and chloride concentrations that fall on this line, we postulate that this alternative process involves mixing of non-seawater end-members occurring in the subsurface region of the hydrothermal system. The observation of chloride concentrations ranging from 58 to 172 mmol/kg lower than seawater throughout the duration of the experiment suggests that at least one end-member is the result of ubiquitous and on-going phase separation which is consistent with other studies of the Main Endeavor Field (Butterfield et al., 1994; Seyfried et al., 2003; Seewald et al., 2003).

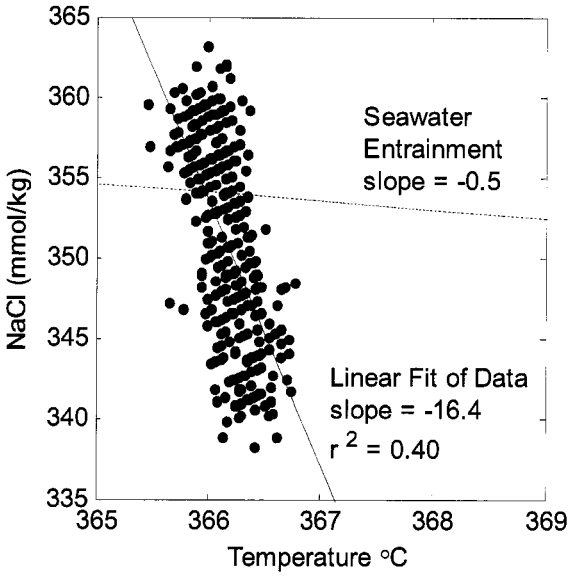

Figure 13. Plot of 5 hour segment of Milli-Q data shown in Figure 10 in NaCl-temperature space showing slope of linear fit to the data and slope of mixing line from seawater entrainment.

During the period from day 217 to day 223 (Figure 10 and supplemental data), we observe a disappearance in the temperature oscillations of the Milli-Q fluid. At the same time, chloride oscillations diminish but do not go away altogether. This pattern is consistent with the differences between re-equilibration times for fluid temperature and fluid chemistry. Namely, a temperature perturbation at depth would be expected to be muted in the vent orifice fluids as the ascending fluid approaches thermal equilibrium with the surrounding rock (Berndt et al., 1989; Wilcock, 1998). However, in the absence of additional phase separation or subsurface mixing, changes in chloride concentration at the vent orifice should reflect changes at depth owing to minimal exchange of chloride with surrounding rock (Berndt and Seyfried, 1990; Seewald and Seyfried, 1990). It should be noted that this re-equilibration of temperature during ascent would change the slope of the mixing line in Figure 13. However, the change would be to larger values, further increasing the difference between the slope for this line and the slope for seawater entrainment.

5.2. Non Tidal Changes Reflect Diversity in Subsurface Processes

5.2.1 Uncoupled NaCl and temperature changes

We also observe trends on non-tidal timescales. Specifically, data from the second Milli-Q deployment span a 70 day period and demonstrate long term variability over the course of the deployment as can be seen in the plot of the data in which a low-pass Butterworth filter has been applied to temperature and calculated NaCl (Figure 14). For some portions of the record, we observe large variability in calculated NaCl with little to no variability in temperature. For instance, the large increase in NaCl just before day 208, coinciding with maximum amplitude in pressure oscillation, occurs while temperature changes are relatively minor. As with the instance of NaCl tidal oscillations without corresponding temperature oscillations, this absence of coupling may reflect perturbations to the fluid chemistry that occur deep within the system resulting in chemical changes that are maintained during ascent while temperature changes are muted by thermal re-equilibration (Berndt et al., 1989; Wilcock, 1998).

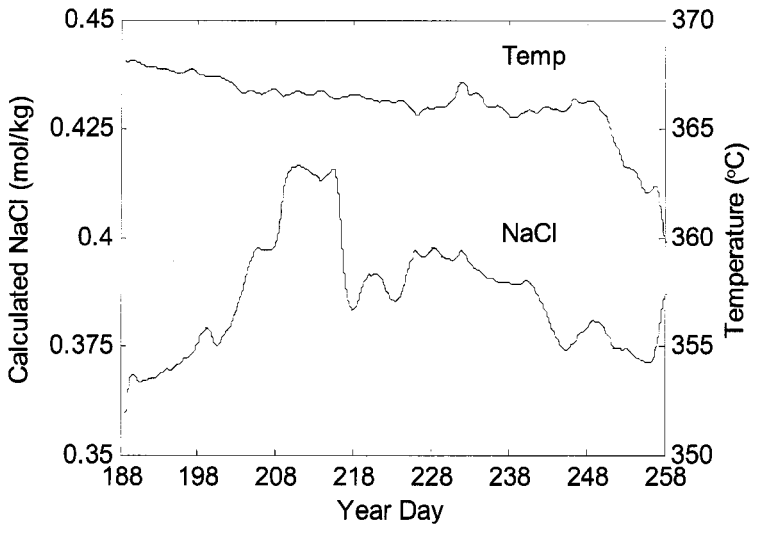

Figure 14. Plot of Milli-Q data from second deployment after application of a low-pass Butterworth filter. Variation on non-tidal timescales implies a variety of subsurface processes affecting vent fluid composition. See text for discussion.

Another possibility is addition of NaCl enriched fluid with temperature similar to the venting fluid. This latter process poses no constraint on the depth at which such brine addition occurs.

Data from the first Milli-Q deployment (Figure 8) illustrates a different scenario. Beginning on day 175, we observe a series of jumps in temperature two of which occur without a concurrent change in conductivity. A re-routing in the circulation of subsurface fluid via the propagation of a cracking front as described by Lister (1974) is consistent with the observed temperature increases. The absence of a coincident change in chloride indicates the fluid was heated in the one phase region of the NaCl-H_2O system (Bischoff and Rosenbauer, 1985), where temperature changes do not induce composition changes. We observe no changes in the tidal signature before and after the jump, but it is not certain whether this putative crack propagation precedes the proposed tidally modulated mixing process or follows it. In the first scenario, the freshly exposed rock would have to heat the mixed hydrothermal fluid at a constant rate to preserve the tidal signature occurring throughout the series of temperature jumps. In the second scenario, the temperature of either end-member may vary independently prior to mixing and we would still observe a tidal signature provided some temperature difference is maintained between end-members.

5.2.2 Coupled NaCl and temperature changes

For other portions of the record, calculated NaCl and temperature co-vary. However, the sign of correlation is not constant. Calculated NaCl data shown in Figure 14 were plotted against their corresponding temperature for four representative segments of the data record. The slope of the best fit line for each of the four segments is listed in Table 5. In two of the segments, we see a direct correlation. In the other two segments, we see an inverse correlation. An inverse correlation is consistent with a temperature perturbation to the conditions of ongoing phase separation. At constant pressure in the

two phase region, an increase in temperature would result in a decrease in NaCl concentration in the vapor phase (Bischoff and Pitzer, 1989). The origin of the temperature perturbation must be sufficiently shallow or the magnitude sufficiently large for the change to be measured at the vent orifice.

Table 5. Variation of slope of calculated NaCl vs. temperature for data from second Milli-Q deployment after removal of tidal signature.

Time Period (Year Day)	Slope (mmolal/°C)	r^2
225.4 – 226.0	-6.8	0.9967
231.0 – 231.9	+2.9	0.9907
250.7 – 251.7	+3.3	0.9943
257.1 – 258.1	-4.4	0.9934

Because increasing temperature results in decreased chlorinity in the vapor phase, a positive correlation between NaCl and temperature increases cannot be explained by a change in temperature of phase separation. One possibility is the interaction of vent fluid with a reservoir of heated brine prior to venting. Fontaine & Wilcock (2006) assert that it is possible for brine to be stored subsurface in rock conductively heated by a magma lens. Release of theses hot subsurface brines into the circulating fluid would result in an increase in both temperature and NaCl.

It should be noted that some of the data segments for which we consider the covariance of temperature and calculated NaCl exhibit changes in temperature and conductivity that are only slightly greater than the uncertainty in our measurement. However, the concurrence of the changes in both temperature and conductivity bolster the case that we are observing actual changes in vent fluid composition and temperature.

5.3. Variability is an Indicator of Complexity

The high degree of temporal variability in vent fluid chemistry at MEF is an indicator of the complexity of hydrothermal response to a magmatic event. Post-eruption behavior predicted by Butterfield et al. (1997) is much smoother and does not predict

some of the trends we observe. However, their model uses discrete fluid samples taken in the immediate aftermath of an eruption rather than in-situ instruments made 12-15 months after an event. In this later phase of hydrothermal response and at a higher temporal resolution, we observe a variety of trends occurring in close temporal proximity, depicting a more jagged evolution of vent fluid chemistry than can be monitored with discrete sampling methods. Further effort needs to be made in constraining the parameters of both tidally correlated processes and other processes, but as our data show, the post-event recovery of a hydrothermal system is highly dynamic.

6. Conclusions

We have developed a prototype resistivity sensor for monitoring chloride concentrations in deep-sea high temperature hydrothermal vents. This instrument has been successfully deployed for periods as long as 2 months and with sampling frequencies as high as 1 min^{-1}. The sensor has been calibrated in the laboratory under simulated hydrothermal conditions. This calibration has been applied to the field data to give chloride concentrations of the vent effluent as a function of time. The conductivity data discussed above demonstrate a correlation with oscillating water column pressure on a tidal time scale (in the case of Milli-Q) as well as other trends that occur over longer time periods (in the cases of both Milli-Q and Grotto). We postulate that the temporal variability in vent fluid chemistry is a result of a suite of subsurface processes including mixing between non seawater end-members and abrupt changes in fluid circulation pathways.

Chapter 3 – Main Endeavour Field at the Juan de Fuca Ridge

Parameters of subsurface brines and hydrothermal processes 12-15 months after the 1999 magmatic event at Main Endeavour Field inferred from in-situ time series measurements of chloride and temperature.

Summary

Phase separation at mid-ocean ridge hydrothermal systems is a widely dsitributed frequently occurring process. It is highly sensitive to dynamic subsurface pressure and temperature conditions and has a significant impact on chloride concentrations of hydrothermal fluid. Although vapor phases produced by phase separation are observed in a variety of hydrothermal settings, observation of conjugate brines that must be produced concurrently are more rare and the fate of subsurface brines is still not well understood. Here we use an array of in-situ chloride sensors deployed at the Main Endeavour Field on the Juan de Fuca Ridge in the wake of a magmatic event to monitor the behavior of hydrothermal vent effluent with high temporal resolution. Our results provide evidence of near-critical chloride depleted fluids within the crust up to 486 m beneath the seafloor. We estimate that a brine reservoir stored beneath the Main Endeavour Field is constrained to temperatures between 131°C and 326°C for chloride concentrations ranging from 6-25 Wt.% NaCl, respectively. Our data suggest that subsurface fluids and circulation pathways vary widely over spatial scales on the order of meters. Under these circumstances, simultaneous measurements of multiple fluid parameters at a high temporal resolution are essential to understanding subsurface hydrothermal processes associated with magmatic events.

1. Introduction

Seafloor spreading at mid-ocean ridges is a discontinuous process with discrete bursts of activity marked by high heat and mass flux (Delaney et al., 1998). The resulting surge of heat to overlying hydrothermal systems can induce periods of intense phase separation wherein chloride-depleted vapors and chloride-enriched conjugate brines are generated from seawater circulating within the crust at high temperature and pressure (Lilley et al., 2003; Seyfried et al., 2003; Von Damm, 2000; Von Damm et. al, 1997; Butterfield et al., 1990).

The hydrothermal response to a magmatic event has been modeled both conceptually (Butterfield et al., 1997) and numerically (Cherkaoui, 2003; Lewis and Lowell, 2004; Wilcock, 2004) and although there are some differences between models, they agree in the general chronology of the hydrothermal response. Immediately following the event, there is a rapid increase in hydrothermal fluid temperature accompanied by a decrease in chloride concentration as low density vapor is produced and vented from the system. Brine is likely segregated and sequestered within the crust (Schoofs and Hansen, 2000; Fontaine and Wilcock, 2006). A slow decrease in fluid temperature is accompanied by a rebound in chloride concentration as the magma intrusion cools and solidifies allowing fluid to circulate deeper within the crust. This pushes the conditions of phase separation to higher pressures (Lister, 1974). The final stage of this process is venting of conjugate brines produced during phase separation in the subsurface immediately following the magmatic event (Schoofs and Hansen, 2000; Lowell and Germanovich, 1997; Von Damm et al., 1997).

Although the results of many studies are in agreement with this model, the fate of produced by subsurface phase separation is still not completely understood. In some systems, brines and conjugate vapors vent from adjacent chimneys (Massoth et al., 1989) or adjacent orifices on the same structure (Von Damm et al., 2003). In other areas, a brine phase is never observed, as in the case at the Main Endeavour Field (MEF) on the Juan de

Fuca Ridge where chloride concentrations in vent effluent were been below seawater concentrations 15 years before a 1999 magmatic event (Butterfield et al, 1994, Lilley et al., 2003) to 6 years after the event (Butterfield, pers. comms).

Several theories have been put forward to account for the 'missing' brines. Bischoff and Rosenbauer (1989) suggested that brines form a convecting layer at the root zone of a hydrothermal cell. Given geophysical constraints on fluid flow, this particular scenario is unlikely. Nevertheless, brines are likely stored within the crust in some form (Fontaine and Wilcock, 2006). Given the finite pore space of mid-ocean ridge basalt and the longevity of phase separation at many hydrothermal fields, the ocean crust eventually should be saturated with brine that must be removed. Michael and Cornell (1998) hypothesize that some of this brine may be assimilated into axial magma chambers. Another possibility is the subsurface lateral movement of brine several kilometers north or south to the Salty Dawg and Mothra vent fields, respectively, where chloride-enriched fluids are observed on a regular basis (Fontaine et al., 2007; Kelley et al., 2002). However, chloride enrichment at these nearby vent fields can not entirely account for the brine produced at MEF based on observed vapor phase composition (Bischoff & Pitzer, 1989; Lilley et al., 2003). Still another explanation is that brine vents intermittently and discrete fluid samples are taken at times when brine is not venting. This last scenario is possible given the temporal variability in fluid chemistry on timescales of days to weeks (Larson et al., 2007; Von Damm, 2000).

In this chapter, we use data collected by in-situ chloride sensors (Larson et. al, 2007) at MEF to provide evidence of the existence of stored subsurface brines. These data also allow us to constrain brine properties and consider a possible mechanism for their partial removal: shallow subsurface mixing. We constrain the depth of linear mixing and end-member properties, calculate the amount of brine that may be removed as part of a mixture and compare it with brine fluxes calculated by other investigators. Finally, we discuss fluid modifications that precede and follow subsurface mixing as the fluid ascends towards and away from the mixing zone, respectively.

2. Experimental Site and Methods

2.1. Experimental Site

In the summer of 2000, two separate cruises to MEF occurred 12-15 months after a magmatic event (Johnson et al., 2000; Lilley et al., 2003). The MEF at 47°57' N, 129°06'W (Figure 15) is located near the western wall of the axial valley (Delaney et. al, 1992). Based on seismic reflection studies, the vent field is located over a thin magma lens, which lies at a depth of ~ 2.6 km (Van Ark et al., 2007). This magma lens is likely located within the plutonic section of the crust and is overlain by sheeted dikes and pillow basalts. (Cudrak and Clowes, 1993).

The locations of sulfide structures at MEF are shown in Figure 15. The field is divided in two portions: a lower temperature northern portion with relatively voluminous vent structures, and a southern portion with smaller more tightly clustered structures that are venting higher temperature fluids (Delaney et. al, 1992).

2.2. Experimental Conductivity Methods

A 32 day cruise to the MEF in June and July of 2000 with the submersible Alvin and the ROV Jason involved fluid sampling and 6-76 day deployments of instrument packages capable of measuring fluid temperature and resistivity. The reciprocal of resistivity, conductivity, serves as a proxy for chloride concentration (Larson et al., 2007). Instruments were deployed in the south in the edifices Bastille, Cannaport, Milli-Q and Sully and in the north at Grotto (Figure 15). Each sensor sampled at a rate of 1 min^{-1}. All instruments were recovered before departing and three more were deployed for the duration of the summer at Milli-Q, Sully, S&M and Puffer. Each of these sampled at a rate of 0.2 min^{-1}. The 18 day follow-up cruise in September with the submersible Alvin involved fluid sampling and recovery of probes previously deployed. An additional probe was placed at Grotto with a 1 minute sampling interval. All of the probe deployments

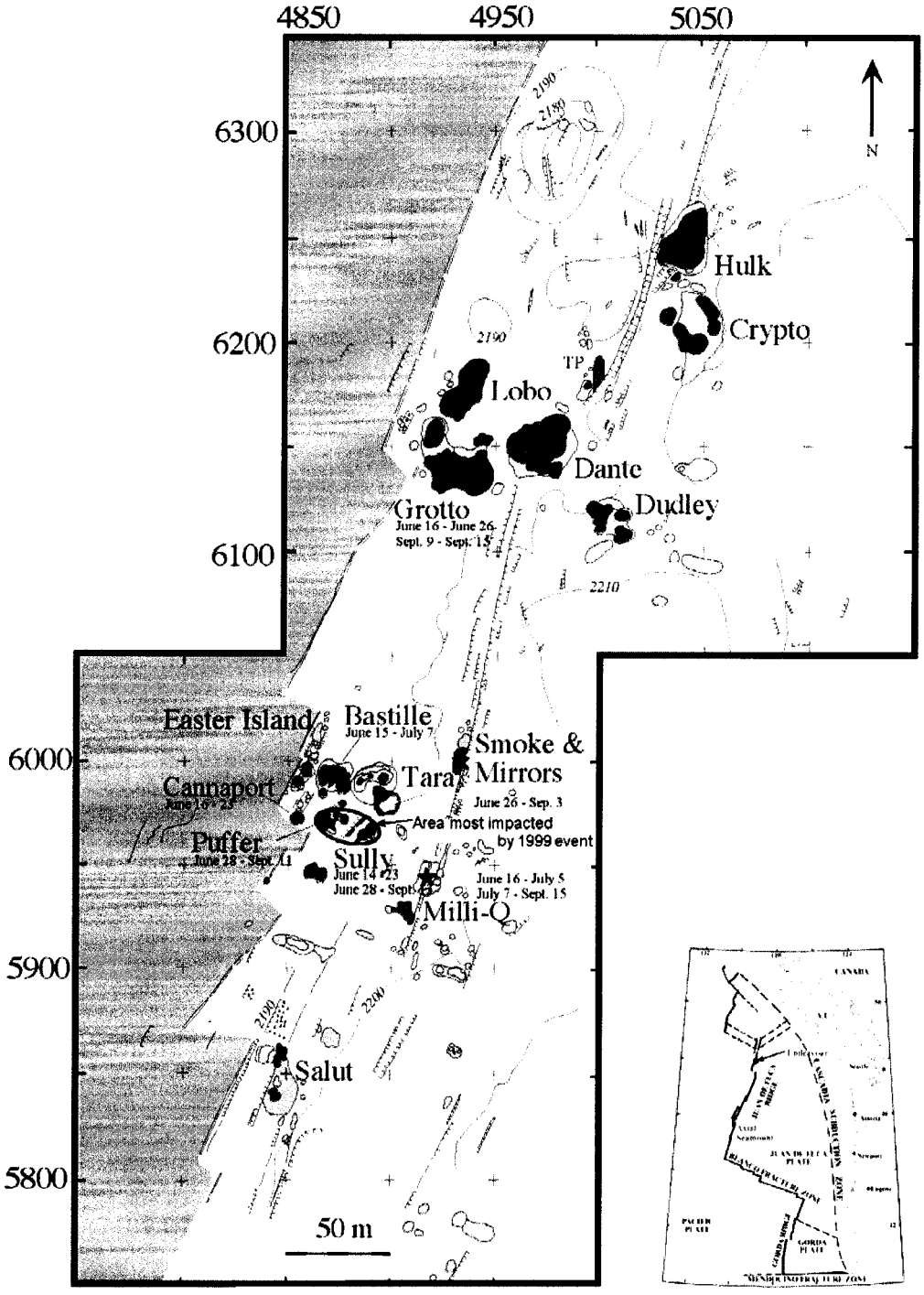

Figure 15. Experimental site, the Main Endeavour Field (MEF) on the Juan de Fuca ridge. Central map (courtesy of D. Kelley) shows arrangement of vent structures within the MEF. Blue stars show locations of deployed instruments and green circle shows the area where the hydrothermal response to the 1999 magmatic event was most pronounced. Deployment date ranges are shown next to vent name. Lower right inset shows regional location of the ridge.

yielded reasonably good data with the exception of the probes deployed at Puffer and S&M which produced resistivity data consistent with cracking of the ceramic sensor housing. For these two vents, only temperature data are reported. Temperature for all instrument packages is good to within 0.1°C.

Before and after each probe deployment, fluid samples were collected with evacuated 150 mL gas tight titanium bottles and 750 mL titanium syringe major samplers. Each sample was analyzed for chloride and magnesium concentration as described in Butterfield et al., 1994. End-member chloride concentrations in fluid samples reported here are calculated from linear extrapolation to zero Mg and are used to normalize conductivity readings for a given sensor (Table 6) as described in Larson et al. (2007). Seafloor pressure was measured by a Paroscientific pressure sensor placed in a central location of the vent field just northeast of Bastille (Figure 15) for the duration of the cruise program with the exception of a short break on day 174 for instrument maintenance.

Table 6. Scale factors calculated with equation (2) are used to normalize field data to fluid sample chloride concentrations. Differences in scale factors for a given deployment are an indicator of instrument drift. This parameter is quantified in the right-most column by comparing calculated chloride at the end of a deployment with chloride measured in post-recovery fluids samples. For Sully #2, calculated chloride values are determined using the scale factor from the pre-deployment sample only because the sensor was likely compromised prior to recovery. Uncertainty in end-member chloride is 2-3%.

Vent, deployment #	Sample type	Avg. end-member chloride (mmol/kg)	Scale Factor (f)	Calculated NaCl (mmol/kg)	% Drift
Bastille	pre-deployment	386	2.066		
Cannaport	pre-deployment	327	0.798		
	post-recovery	339	0.789	344	1.5
Sully, #1	pre-deployment	312	1.486		
	post-recovery	309	1.539	296	4.2
Sully, #2	pre-deployment	303	1.566		
	post-recovery	350		251	28.3
Grotto, #2	pre-deployment	442	0.435		
	post-recovery	468	0.440	463	1.1

3. Field Data

Data from 7 of 10 instrument packages are shown in Figure 16–Figure 20. The remaining 3 data sets were previously reported in Chapter 2 in Figure 8–Figure 11 along with a description of the instrument, the resistive measurement and the calibration process. Figure 16–Figure 20 show seafloor pressure, fluid temperature and chloride concentration, where available, as calculated from temperature and conductivity using the method described in Larson et al. (2007). Deployment dates and chloride and temperature ranges for each data set are compared in Table 7.

3.1. Bastille vent

Chloride concentrations at Bastille (Figure 16) range from 271 to 439 mmol/kg, well below a typical seawater value of 542 mmol/kg. Chloride also exhibits a clear correlation in both amplitude and frequency with tidal oscillations in seafloor pressure. There is a decrease in the mean chloride from 360 to 310 mmol/kg from day 167 to day 171. During this time, overall temperature increased from 375.6°C to 377.2°C, however, the trend is not smooth. The temperature rapidly increases from 376°C to 377°C in just over an hour starting on day 168.4. Just before day 169, there is a temperature decrease from 377.2°C to 376.2°C over the course of nearly 6 hours followed by a gradual return to 377.2°C over the next several hours.

At day 171.2, mean chloride begins a rebound while the temperature continues to exhibit highly variable behavior. A dip in temperature to a minimum value of 376.3°C occurs around day 171.5, and then the temperature quickly increases to 377.7°C, followed by a relatively slow 0.8°C decrease. At day 172.1, temperature jumps 1.6°C to 378.6°C. Another decrease in temperature occurs around day 172.5 before the temperature drops to 377.7°C. Temperature then exhibits an overall slow and steady decline over the remainder of the record to 377.1°C. Mean chloride variation is less rapid

Table 7. Comparison of the experimental parameters and the data from the resistivity probe deployments vents in Main Endeavour Field (MEF). Characteristics of the tidal signature for each vent are shown in the last two rows.

Vent/deployment #	Bastille	Cannaport	Sully, #1	Sully, #2	Grotto, #2	S & M	Puffer
Deployment date	6/15/00	6/16/00	6/14/00	6/28/00	9/9/00	6/26/00	6/28/00
Recovery date	7/7/00	6/23/00	6/23/00	9/13/00	9/15/00	9/3/00	9/11/00
Length of deployment (days)	23	8	10	78	6	70	76
Avg. Cl^- for pre-deployment fluid samples (mmol/kg)	386	327	309	303	442	469	401
Avg. Cl^- for post-deployment fluid samples (mmol/kg)	379	339	309	356	468		434
Temperature range (°C)	375-379	360-363	369-367.5	370-372	363-364	367-369	369-372
Maximum peak-to-peak tidal chloride oscillation (mmol/kg)	36	12	34	58	non-oscillating signal	no chloride data available	no chloride data available
Minimum peak-to-peak tidal chloride oscillation (mmol/kg)	12	8	14	28			

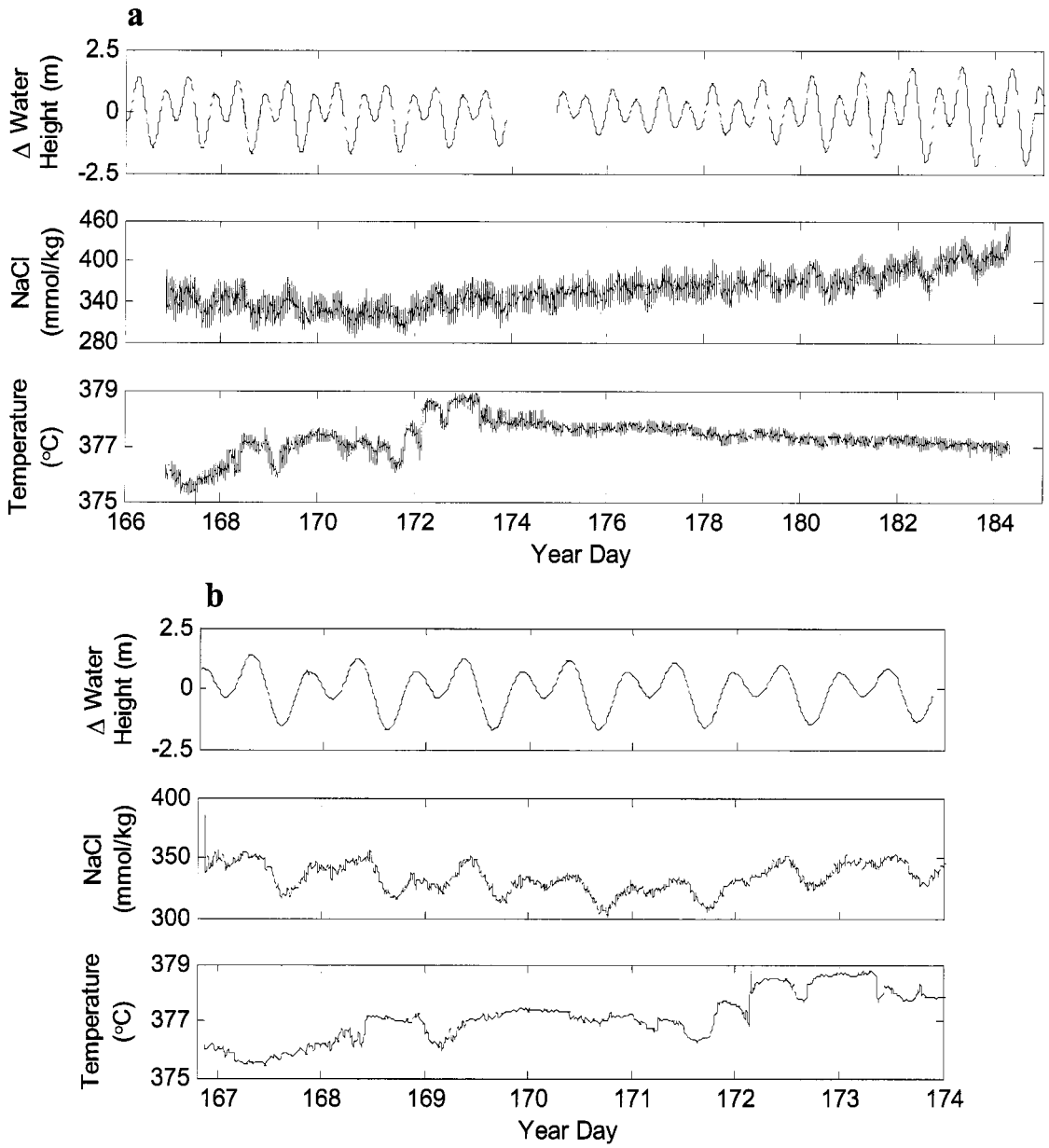

Figure 16. Pressure, temperature and calculated chloride for (a) full record from Bastille vent and (b) blown up section of Bastille data after application of a low-pass Butterworth filter with frequency cutoff of 48 day^{-1}. Panel 1 shows seafloor pressure at MEF. Panels 2 and 3 show fluid temperature and calculated chloride concentrations of vent effluent. Pressure is shown as difference in water column height from the mean at the site of the pressure sensor (see text for description). Chloride concentrations are calculated as described in Larson et al. (2007) using scale factors from Table 6.

than temperature. Chloride steadily climbs just before the 2.3°C temperature increase on day 172.1 and ends at 392 mmol/kg, ~30 mmol/kg higher than the start of the deployment and ~80 mmol/kg higher than the observed minimum value. Simultaneous appearance of highly erratic behavior in both the temperature and chloride signals at day 184.3 (not shown) indicate that data transmission was compromised at this point, consistent with the observation upon recovery that the sensor housing was destroyed. For this reason, only pre-deployment fluid samples are used in normalizing conductivity values from this vent.

3.2. Cannaport vent

Chloride concentrations at Cannaport (Figure 17) range from 274 to 346 mmol/kg. Although chloride variations exhibit a correlation in frequency with seafloor pressure oscillations, the dependence on pressure is much less pronounced than in other vents. However, Cannaport is one of three vents (along with Milli-Q and S&M) that exhibits well defined tidally correlated temperature oscillations 180° out of phase with

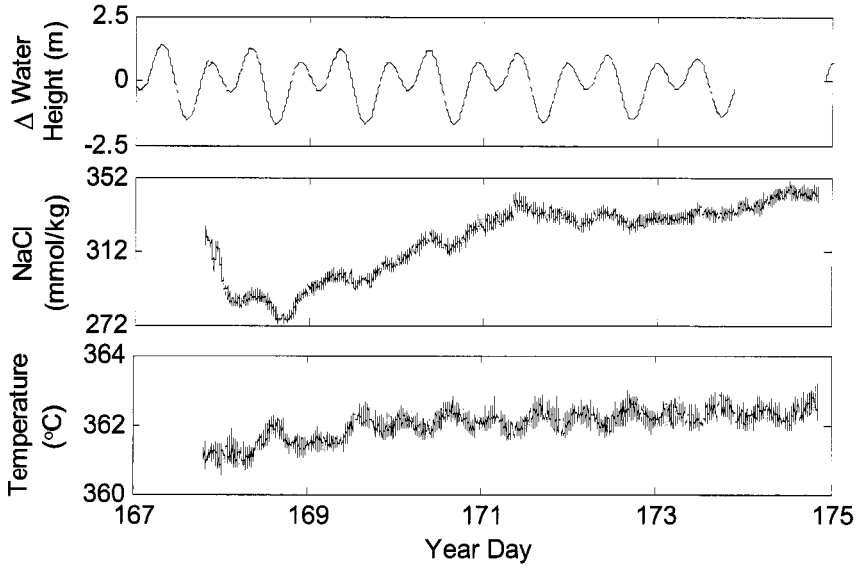

Figure 17. Pressure, temperature and calculated chloride for Cannaport vent. Panels are as described in Figure 16 caption.

pressure oscillations (Larson et al., 2007). The amplitude of temperature oscillations at Cannaport is ~0.5°C.

Mean chloride at Cannaport decreases from 315 to 284 mmol/kg from day 167.8 to 168.7, then steadily increases to 333 mmol/kg over the next 3 days. Mean chloride exhibits another minor dip over the next 3 days then climbs to 341 mmol/kg by the end of the record. One small 10 mmol/kg jump in the chloride concentration occurs at day 171.4 but, there is nothing in the temperature signal that corresponds to this change. Mean temperature exhibits a slight increase from 361 to 363°C over the course of the 8 day record.

3.3. Sully vent

3.3.1 Deployment #1, year days 165.8 – 174.9

Chloride concentrations during the first deployment at Sully (Figure 18) range from 316 to 358 mmol/kg and exhibit a correlation in both frequency and amplitude with pressure oscillations. The mean chloride concentration shows little variation during the course of the deployment with the exception of a 20 mmol/kg dip occurring over the course of the first day of the deployment. This is apparent only after the tidal signature was filtered out. The mean chloride then rebounds to ~335 mmol/kg and remains steady for the rest of the deployment.

Fluid temperature at the start of this deployment is ~368.3°C. There is a 0.5°C dip starting around day 166.3 and lasting ~ 4.5 hours. The temperature then drops to ~367.9°C starting at day 167.3 and lasting for about 1.5 days and interrupted only once at day 167.7 by a 0.4°C positive excursion. At day 168.8, there is a rapid increase in temperature to 368.7°C over the course of ~80 minutes. The temperature slowly declines back to ~367.8°C, then climbs at a steady pace for the remainder of the record to end at approximately the same temperature as at the start of the record.

The dip and rebound in temperature between days 167.3 and days 168.8 is preceded by a dip and rebound in the mean chloride concentration between days 166.1 and 168.2. Another noteworthy feature of the temperature record is the appearance of small (< 0.4°C) temperature oscillations at approximately day 172.8 and visible only after application of a low-pass filter (Figure 18b).

3.3.2 Deployment #2, 179.7 – 256.9

Chloride concentrations for the second deployment at Sully (Figure 18) range from 377 to 524 mmol/kg and exhibit a correlation in frequency and amplitude with seafloor pressure oscillations. However, this signal is significantly more variable than most of the other data records. Although the correlation with tidal pressure is still evident, the decreased signal to noise ratio compared with other data records complicates determination of oscillation magnitude (Table 7). Mean chloride concentration exhibits an overall increase from 302 mmol/kg to 385 mmol/kg over the course of the 1.5 month deployment. However, the rate of increase varies, with chloride increasing more rapidly between days 180 and 206.3. Following this increase, the chloride dips slightly at day 206.8, then again at day 235.8. The chloride rebounds after day 235.8, reaching a maximum value of 428 mmol/kg at day 247.6 then dropping again slightly before rebounding to a value of 434 mmol/kg at day 254.5.

Just after day 254.5, chloride variability intensifies and we see a much wider range of chloride than observed throughout the preceding record. If we use chloride measured in the pre-deployment fluid sample to normalize conductivity data from this sensor, then differences between calculated chloride and chloride measured in post-recovery fluid samples indicate that sensor integrity was compromised (Table 6). However, agreement to within 16% between what we suspect is the last viable calculated chloride measurement before sensor failure (405 mmol/kg) and average chloride measured in fluid samples taken 2.5 days later (350 mmol/kg) indicates that sensor integrity remained intact until this point (Figure 18). Although a 16% difference is

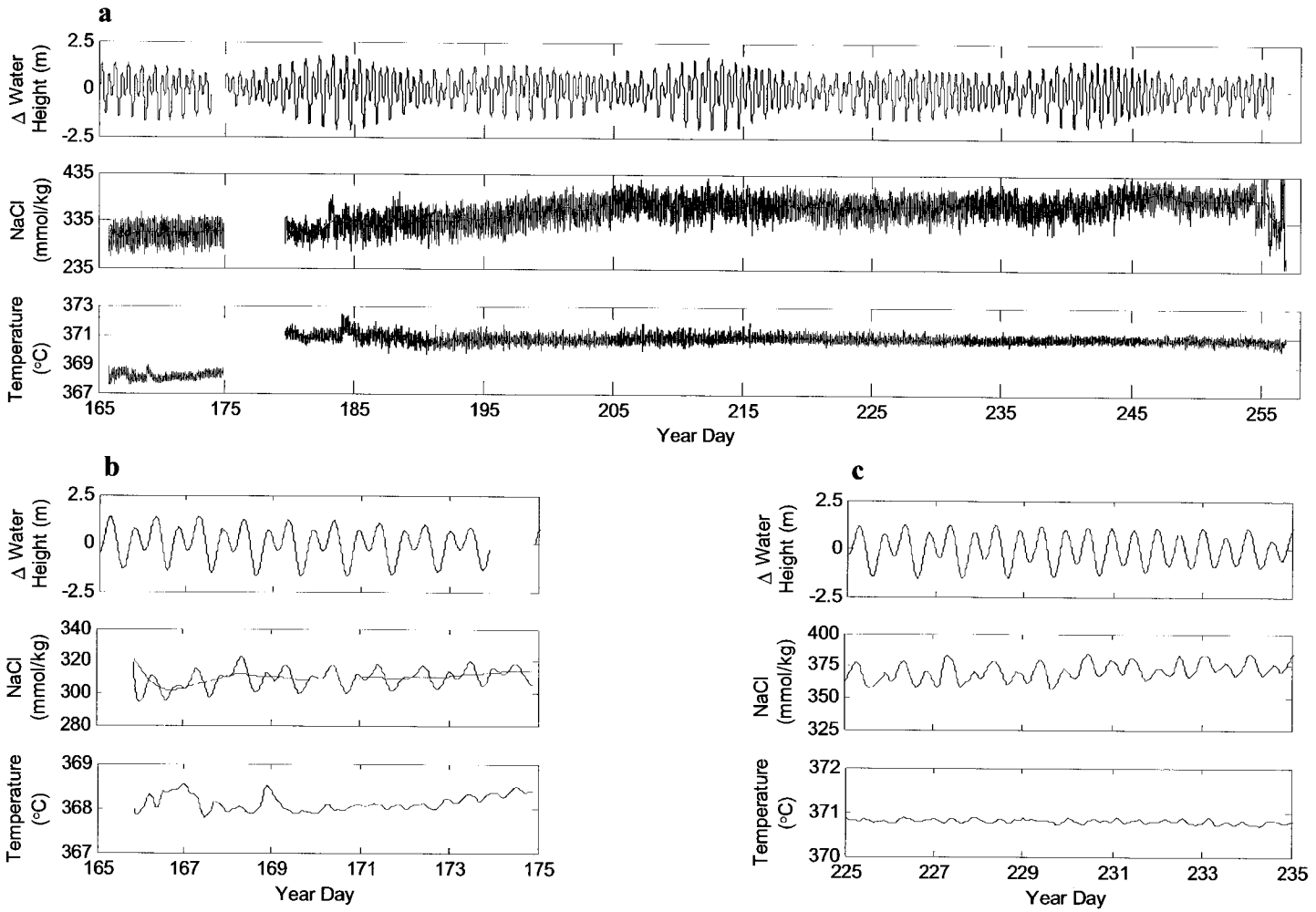

Figure 18. Pressure, temperature and chloride for (a) both deployments at Sully vent. (b) Blown up section of first deployment at Sully after application of a low-pass filter with frequency cutoff of 4 day^{-1} (black trace) and 0.5 day^{-1} (red trace). (c) Blown up section of second deployment at Sully after application of low-pass filter with frequency cutoff of 4 day^{-1}. Panels are as described in Figure 16 caption.

outside the uncertainty of the measurement, it is within the range of chloride variability observed elsewhere in MEF over the course of 2.5 days.

Throughout, the record, the temperature remains fairly constant at ~370.7°C with the exception of a 1.8°C jump at day 184 occurring over 24 minutes. The temperature then decreases over the next 6.5 days to ~370.3 before rebounding to 370.7°C, where it remains relatively steady for the remainder of the record. The spike in temperature at day 184 is preceded by a 40 mmol/kg increase in chloride occurring over approximately 30 minutes and remaining elevated for nearly 7 hours. Afterwards, chloride concentrations are comparable to the range of values seen before the increase.

3.4. Grotto vent

Chloride concentrations from Grotto (Figure 19) range from 420 to 567 mmol/kg. Unlike other vents, Grotto does not exhibit tidally-correlated oscillations in either temperature or chloride. However, there are a series of positive chloride excursions in the first 2 days of the deployment. These excursions generally occur as clusters of spikes. One such cluster occurs near the start of the record just before day 253, lasting 5.7 hours with the spike magnitude ranging from 40-60 mmol/kg and spike duration ranging from 1-8 minutes (sampling rate for this deployment was 1 sample/minute). There is another shorter cluster at day 253.25 lasting 46 minutes with the spike magnitude ranging from 35-56 mmol/kg and duration ranging from 1-3 minutes. A much longer cluster starts at day 253.7 and lasts almost 9 hours, with spike magnitude ranging from 32-94 mmol/kg and spike duration ranging from 1-6 minutes. A cluster beginning just before day 254.4 exhibits short lived spikes similar to preceding clusters but in this case, we also observe a sustained 22 minute elevation in chloride concentration of 41 mmol/kg with respect to chloride concentrations before and after the cluster. Two more such offsets start at days 254.44 and 254.85, last 71 minutes and 133 minutes, respectively, and exhibit elevations with respect to surrounding values of 15 and 10 mmol/kg. Chloride remains steady for the remainder of the record.

Temperature remains relatively stable during this deployment with the exception of the period between days 254 and 255. This is around the time when we observe several clusters of chloride spikes, including the 9 hour cluster described above. At day 254, temperature increases 0.5°C over 79 minutes from 363°C to 363.5°C. At day 254.4,

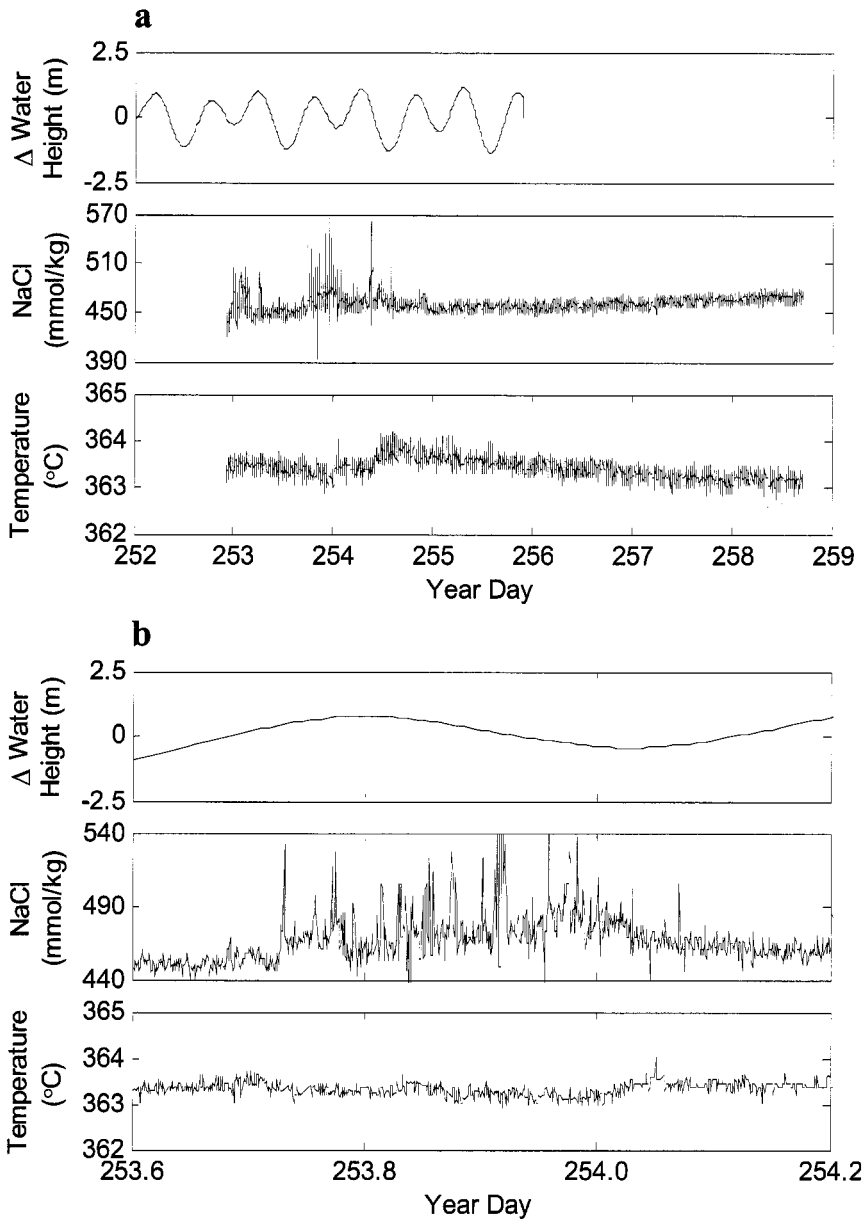

Figure 19. Pressure, temperature and calculated chloride for (a) full record from Grotto vent and (b) Blown-up section of data. Panels are as described in Figure 16 caption.

temperature increases more slowly from 363.5 to 363.9°C. This 0.4°C increase occurs over ~7 hours.

After this increase, temperature exhibits a steady decline throughout the remainder of the record. Although chloride spikes and increased temperature variability at Grotto take place within the same window of time, the variability of the two parameters is not synchronized. This lack of synchronization contrasts to the correlated chloride and temperature oscillations in fluid from southern vents at MEF.

3.5. Smoke & Mirrors (S&M) temperature record

Chloride data from the instrument deployed at S&M is not available due to sensor failure during deployment. Chloride measured in a fluid sample take at this site just prior to the instrument deployment was 469 mmol/kg, higher than any other vent discussed in this paper except the northern vent, Grotto, where some spikes in chloride reached a maximum value of 567 mmol/kg.

At S&M (Figure 20), temperature oscillations correlate with tidal pressure oscillations, with amplitudes ranging from 0.3-0.5°C. These amplitudes are larger than all other southern vents where instruments were deployed with the exception of Milli-Q where the amplitude of temperature oscillations is comparable to those at S&M (Larson et. al, 2007). Mean temperature shows little variability over the course of the deployment.

3.6. Puffer temperature record

Chloride data from the instrument deployed at Puffer are not available due to sensor failure during deployment. Chloride concentration measured in a fluid sample taken just prior to deployment was 403 mmol/kg and the average chloride concentration measured in samples taken just after instrument recovery was 434 mmol/kg.

Temperature at Puffer (Figure 20) exhibits significant temporal variability that is unique compared to all other vent fluid temperature records. Generally, temperature variability occurs in clusters of recurring features that emerge throughout the temperature

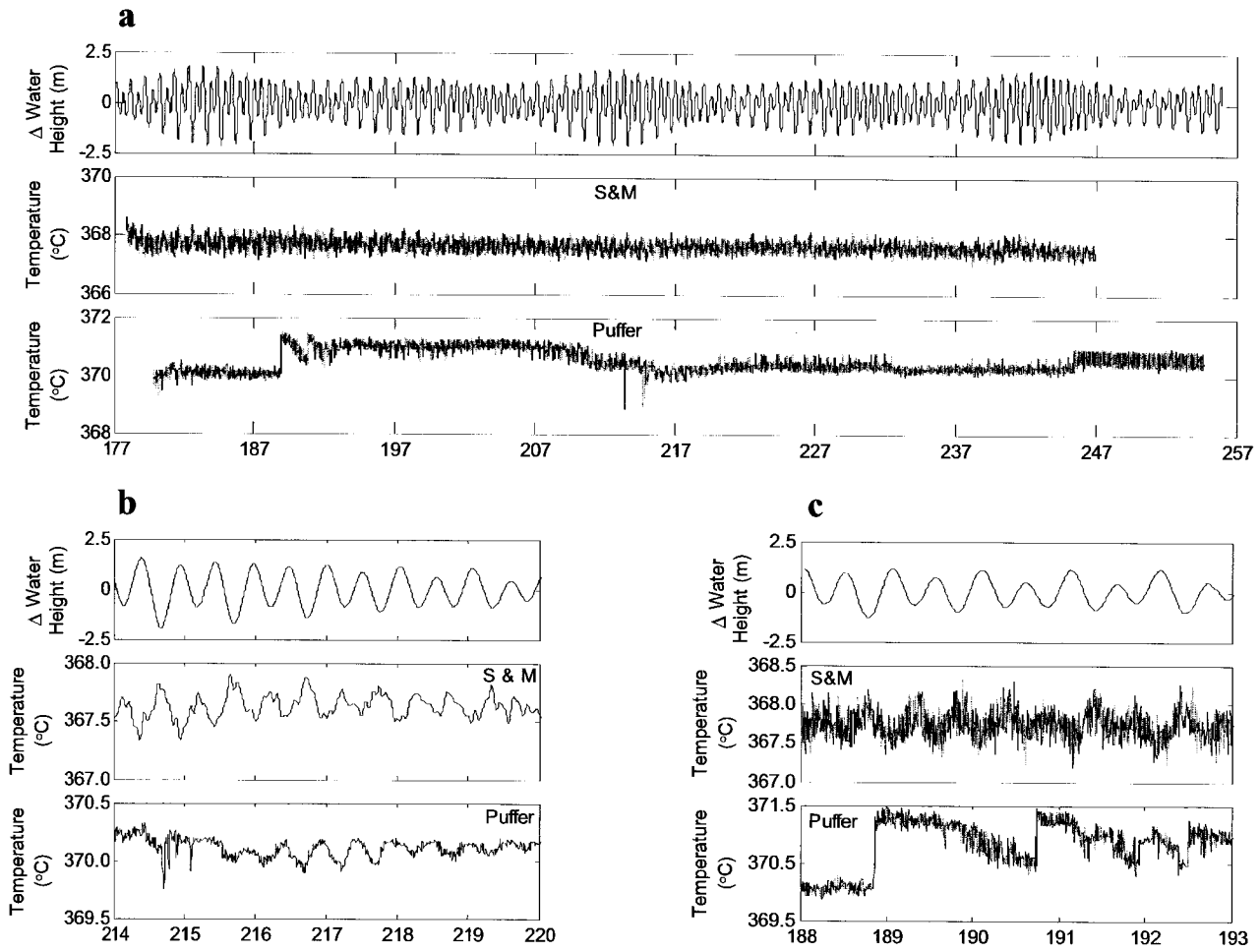

Figure 20. Pressure and temperature for (a) full records from Puffer and Smoke & Mirrors vents, (b) blown up portions of temperature records after application of a low-pass Butterworth filter with frequency cutoff of 12 day^{-1} (c) blown up portions of unfiltered temperature records. Pressure and temperature panels are as described in Figure 16 caption.

record. In addition, near the beginning of the deployment, at day 180.9, we note 2 cycles of temperature oscillations approximately 0.5°C in magnitude. However, unlike temperature oscillations at other vents, those at Puffer are nearly in phase with pressure oscillations.

At day 188.8, there is a rapid increase in temperature from 370.2 to 371.3°C occurring over 15 minutes followed by a slower decline to 370.5°C occurring over 1.9 days (Figure 20c). Then, there is another rapid increase from 370.5 to 371.5°C occurring over 5 minutes followed by a decrease to 370.5°C over 28 hours. Mean temperature levels off at ~371.1°C for the next 15 days. During this time, Recurring negative temperature excursions range up to 0.8°C in magnitude. These excursions generally occur at or around high tide but this is not always the case.

Just after day 209, mean temperature decreases slowly from 371 to 370.2°C over the course of ~7 days. During this period, temperature is highly variable including a series of negative excursions beginning just after low tide at day 214.7 and ranging up to 1°C in magnitude. About 1 day later after mean temperature has begun to rebound, there are roughly 6 cycles of temperature oscillations with a maximum amplitude of 0.4°C. Similar to temperature oscillations at day 180.9, these oscillations exhibit a positive correlation with seafloor pressure rather than the inverse correlation observed at other vents.

Beginning at day 219.9 and lasting for 12.5 days, we observe recurring but random positive temperature excursions ranging up to 0.5°C and set atop a baseline value of ~370.3°C. At day 232.6, there is a 0.2°C decrease in mean temperature followed by a 0.2°C increase in mean temperature ~13 days later. During this sustained dip in temperature, we continue to see temperature spikes, though less frequently than before the offset. Mean temperature remains steady at ~370.5°C for the remainder of the record but the temperature reading is still highly variable with a span of ~0.5°C.

4. Discussion

4.1. Characteristics of tidal signature

4.1.1 Fourier analysis

For each vent in the southern portion of the MEF where time series measurements of chloride concentration were made, there is a tidal signature in the data. Visual inspection indicates that the strength of the tidal component is not uniform for all vents so Fourier analysis was used to more quantitatively explore the variation. The 'psd' function in the Matlab signal processing toolbox (Welch, 1967) was used to estimate the power spectral density of tidal frequencies in our time series chloride, temperature and seafloor pressure data. The results of these analyses are shown in Figure 21 and Figure 22.

With the exception of Grotto, the spectrum for each vent (Figure 21b-e) has peaks in both the diurnal and semi-diurnal frequency bands that match the position of the analogous peaks in the spectrum for the pressure signal (Figure 21a). For the second deployment at Sully, the longest chloride record analyzed (Figure 21d), peak resolution is sufficient to identify all four tidal constituents that appear in the power spectrum of the pressure data: S2, M2, O1 and K1. Resolution for the shorter records is only good enough to separate the diurnal from semi-diurnal constituents. It is also worth noting that the power of diurnal and semi-diurnal tidal peaks in the spectrum for Cannaport is ~1 order of magnitude lower than for all the other vents in the southern portion of MEF for which we have chloride data. This result is consistent with the fact that chloride oscillations are much less visually apparent in the Cannaport data record (Figure 17) than in the other southern vents (Figure 16,Figure 18).

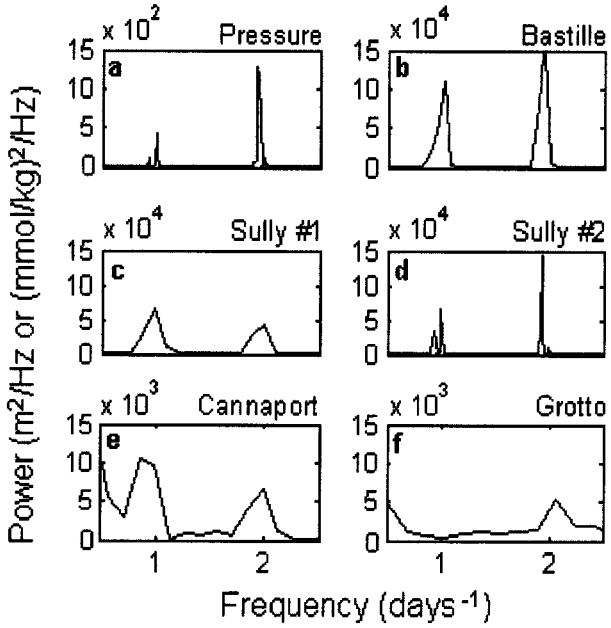

Figure 21. Estimates of power spectral density in pressure and chloride data calculated using the method of Welch (1967) as applied in the Matlab function, psd.m to (a) seafloor pressure (b) Bastille chloride (c) Sully chloride from first deployment (d) Sully chloride from second deployment (e) Cannaport chloride and (f) Grotto chloride.

For Grotto, the only vent in the northern portion of the MEF for which we have data, the power spectrum (Figure 21f) shows a small poorly resolved peak in the semi-diurnal frequency band despite no obvious tidal signature in the raw data. The magnitude of the peak is comparable to peak heights in the power spectrum for Cannaport which is the only southern vent with temperatures as low as those observed at Grotto.

A Fourier analysis was also performed on the temperature records and these results are shown in Figure 22. Cannaport and S&M exhibit readily visible temperature oscillations and their respective power spectra have diurnal and semi-diurnal peaks (Figure 22b, g) with better resolution and higher power than in spectra for all other vents (Figure 22c, d, e, f, h). There is also a well resolved peak in the semi-diurnal band of the Puffer spectra with power approximately half the magnitude of the analogous peaks in the Cannaport and S&M spectra.

The results of the foregoing spectral analyses are consistent with similar calculations performed by Larson et al. (2007) on data from Milli-Q and a previous deployment at Grotto with the exception that for earlier Grotto data there is no power in either the diurnal or semi-diurnal frequency bands. Our results and those of Larson et al. (2007) indicate that observed chloride and temperature oscillations are coupled to tidal loading of the hydrothermal system.

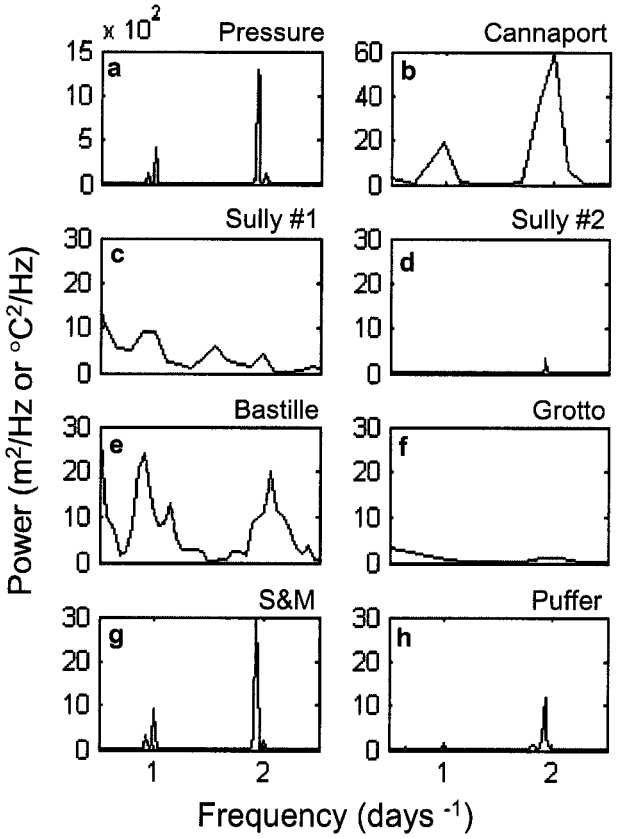

Figure 22. Estimates of power spectral density in pressure and temperature data calculated using the method of Welch (1967) as applied in the Matlab function, psd.m to (a) seafloor pressure (b) Bastille temperature (c) Sully temperature from first deployment (d) Sully temperature from second, deployment (e) Cannaport temperature and (f) Grotto temperature.

4.1.2 Tidal harmonic analysis

We now consider the phase angle of oscillating chloride and temperature with respect to oscillating seafloor pressure. To better determine these phase angles, we use the T_Tide software package from Pawlowicza et al. (2002). This program calculates the Greenwich phase for a given tidal constituent frequency. This quantity is the time shift between the peak value of an oscillating signal and the time when the equilibrium forcing for the chosen constituent is at its largest positive value at 0° longitude (Figure 23).

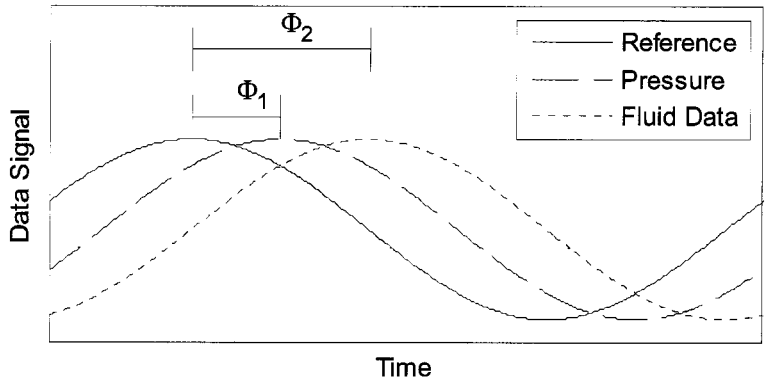

Figure 23. Phase angles, Φx, calculated for oscillating signals using the Matlab toolbox developed by Pawlowicza et al., (2002)

The Greenwich phase for any signal has the same reference point, so we can compute the difference between the Greenwich phase for pressure, Φ_1, and the Greenwich phase for chloride or temperature, Φ_2, to determine if there is any phase lag between the two oscillating signals (Figure 23):

$$(3) \quad \Delta\Phi = \Phi_2 - \Phi_1$$

For our phase angle analysis, we select the tidal constituent M2 because it has the greatest power in the frequency spectrum of the pressure signal. Next we chose the three longest data sets with the most pronounced tidal signatures: Sully #2, S&M and Puffer. Under

these circumstances, M2 peaks in the frequency spectra (Figure 21, Figure 22) are better resolved than records with a short duration or weak tidal signature. These selection criteria enable more precise determination of phase angle (Table 8).

Oscillations in chloride at Sully during the second deployment exhibit a phase shift of 9° with respect to seafloor pressure (1° for the M2 constituent is equivalent to 4.3 minutes). However, this shift is only slightly higher than the combined 95% confidence intervals (8.7°) for pressure and chloride (Table 8). Thus, at this level of certainty, the phases for these two signals are almost indistinguishable. Oscillations in temperature at S&M exhibit a shift of -182° indicating temperature oscillation here are almost exactly out of phase with respect to seafloor pressure such that we see a minimum in temperature at high tide.

At Milli-Q, the phase shift is larger than can be explained by uncertainty in the calculation (Larson et al., 2007) suggesting there is some lag between seafloor pressure and the hydrothermal response at this vent. Implications of this phase lag as well as the absence of a phase lag at Sully are discussed in more detail in the following section.

Table 8. Comparison of phase angles, Φ, calculated by T_Tide (Pawlowicza et. al, 2002) for the M2 tidal constituent in seafloor pressure and selected data records. Differences between Φ for a given data record and Φ for pressure are an indicator of delays in hydrothermal response to oscillating pressure. Calculations for Milli-Q #2 chloride are taken from Larson et al. (2007).

Data Signal	Φ (degrees)	ΔΦ w.r.t. pressure	2σ	s/n
Pressure	241	——	1.3	2200
Milli-Q chloride from deployment #2	254	13	2.9	390
Milli-Q chloride from deployment #2	51	-190	17.1	11
Sully chloride from deployment #2	250	9	7.4	66
S&M Temperature	59	-182	3.5	250
Puffer Temperature	215	-25	21.4	6.6

The results of tidal harmonic analysis at Puffer are unique. Although the power of the M2 constituent at this vent is much lower than for other vents (Figure 22h), the M2 peak is still well defined indicating there is some tidal influence in the signal. The phase shift for the M2 constituent is -25°, which is only slightly less then the combined 95%

confidence intervals (22.7°) for pressure and Puffer temperature (Table 3). This indicates the phase angle could be much smaller. Thus, peaks in temperature oscillations at Puffer occur around the same time as peaks in pressure which is consistent with sections of the Puffer temperature record (Figure 20b).

4.2. Tidal loading coupled to vent effluent composition through subsurface mixing

On the basis of a best fit line of calculated chloride vs. temperature for data from Milli-Q (Figure 24a, b), Larson et al. (2007) attribute tidally correlated temperature and chloride oscillations to linear mixing between non-seawater end-members. A linear fit of calculated chloride vs. temperature data from Cannaport (Figure 24c, d) yields a similar result indicating that subsurface mixing is not limited to Milli-Q. Cannaport is the only other vent where both chloride and temperature oscillations have been observed. Absence of temperature oscillations in vents where we observe chloride oscillations does not preclude subsurface mixing but it does indicate differences in properties of end-member fluids. Here, we attempt to constrain the properties of both vapor and brine end-members.

It is important to note that because the tidal signature is much less pronounced in Cannaport than in Milli-Q (Figure 21, Figure 22 and Larson et al., 2007), it was necessary to apply a low pass filter with a cutoff frequency of 12 hr^{-1} (Parks and Burrus, 1987) to quantitatively examine the relationship between chloride and temperature oscillations. Furthermore, the section of Cannaport chloride data we have used in Figure 24c, d represents the portion where the tidal signature is the strongest; for most of the Cannaport record, the tidal signature is much less pronounced.

4.2.1 Brine properties

Crone and Wilcock (2004) demonstrated that tidal loading of hydrothermal systems can result in lateral pressure gradients that drive lateral fluid flow near the upflow zone. Brines may line the walls hydrothermal upflow zones as well as the

surrounding rock while vapors flow through the center of the upflow zone (Fontaine and Wilcock, 2006, Fox, 1990; Goldfarb and Delaney, 1988).

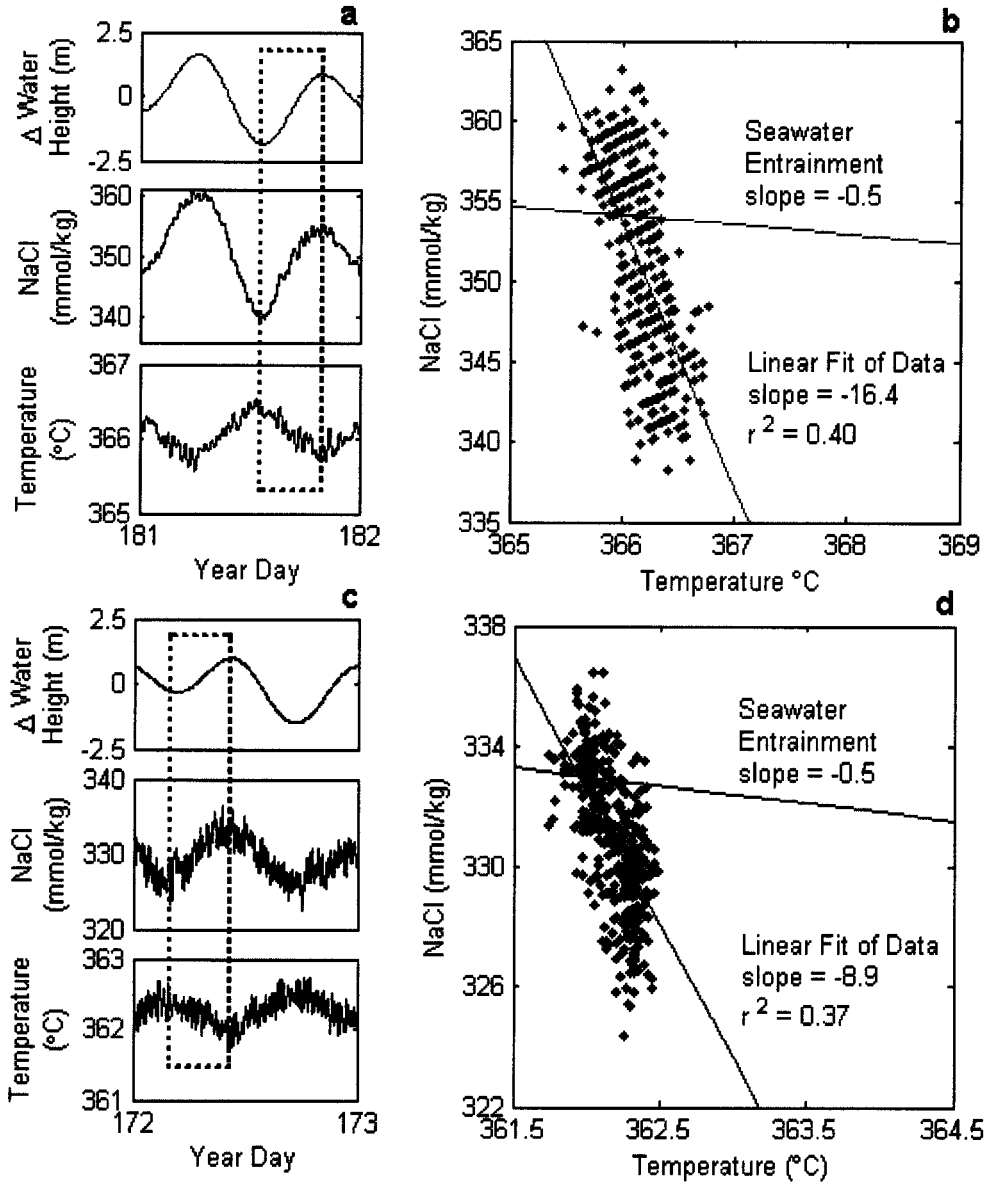

Figure 24. Selected portions of in-situ data from (a) Milli-Q and (c) Cannaport plotted in chloride-temperature space for each vent in panels (b) and (d) respectively. A linear regression has been applied to data from each vent. Milli-Q data in parts (a) and (b) are taken from Larson et al. (2007).

Our data are consistent with a process in which tidally driven horizontal subsurface flow results in mixing of chloride-depleted vapors with chloride-enriched brines to produce tidally coupled oscillations in vent fluid chloride and temperature.

We can constrain the temperature of brine end-members in the following manner. First we assume that the minimum chloride during an oscillation represents the vapor end-member and that the maximum chloride concentration represents a mixture of vapor and brine. Next, we estimate salinity of the brine end-member. Fontaine and Wilcock, (2006) estimate a range between 15-65%. Other investigators have shown that phase separation immediately after a magmatic event may occur at or just beneath the seafloor (Lilley et. al., 2003; Seyfried et al., 2003). Under these conditions, brines produced by phase separation may be as low as 6 Wt.% NaCl (Bischoff and Pitzer, 1989). Here, we consider the full range of postulated brines (6-65%). We calculate the brine mixing fraction (X_b) required to produce the observed increase in chloride over the course of one half tidal cycle using equation (4).

$$(4) \quad X_b = \frac{S_f - S_v}{S_b - S_v}$$

S is Wt.% NaCl and subscripts b, v and f indicate brine, vapor and observed vent fluid respectively. As an example, the half tidal cycle at Milli-Q from year day 181.5 to day 181.8 is examined. During this period, chloride concentration increases from approximately 330 to 350 mmol/kg (1.95 to 2.02 Wt.% NaCl) and temperature decreases from 366.5 to 365.7°C (Figure 24a). For brines ranging from 6-65%, X_b ranges from 0.02 to 0.001 respectively (Table 9).

We use these mass fractions and the analogous version of equation (4) for temperature to calculate brine temperatures that range from 326°C for 6 Wt.% NaCl to 136°C for 25 Wt.% NaCl (Table 9). The small mass fraction required for a brine of 65 Wt.% NaCl implies a temperature below freezing.

Table 9. Mixing fraction and temperature of vapor and brine end-members as calculated using equation (4) and the specified parameters for the half tidal cycle at Milli-Q from day 181.5 to day 181.8 and at Cannaport from day 172.2 to day 172.5.

Parameter	Milli-Q			Cannaport		
S_b (Wt.% NaCl)	6	25	65	6	25	65
S_v (Wt.% NaCl)	1.95	1.95	1.95	1.92	1.92	1.92
T_v (°C)	366.5	366.5	366.5	362.5	362.5	362.5
S_f (Wt.% NaCl)	2.03	2.03	2.03	1.92	1.92	1.92
T_f (°C)	365.7	365.7	365.7	362	362	362
X_v	0.9802	0.9965	0.9987	0.9879	0.9978	0.9992
X_b	0.0198	0.0035	0.0013	0.0121	0.0022	0.0008
T_b (°C)	326.0	136.0	-264.0	321.2	131.2	-268.8

However, the presence of highly concentrated brines cannot be ruled out because hotter brines would produce chloride oscillations without coincident temperature oscillations. This is consistent with data from Bastille and Sully (Figure 16 andFigure 18). Results of analogous calculations for a selected portion of Cannaport data (Figure 24b) yield temperatures ranging from 131-321°C for brines ranging from 6-25 Wt.% NaCl respectively (Table 9). A caveat to the calculation of brine temperature is that temperature oscillations at the seafloor are likely muted during ascent (Wilcock, 2004). Thus, brine and vapor temperatures may be cooler and hotter respectively.

4.2.2 Mechanism and depth of mixing

For subsurface mixing to be coupled to tidal loading, the mixing process must be highly sensitive to pressure. This is because pressure changes over the course of a tidal cycle (less than 0.5 bar) are less than 0.2% of seafloor pressure and they represent an even smaller percentage of hydrostatic pressure deeper within the crust. Pressure sensitivity is most pronounced if the vapor end-member is at or near its critical point where a fluid becomes infinitely compressible such that small pressure changes result in large volume changes (Johnson and Norton, 1991).

It is important to note that lateral pressure gradients may exist even when subsurface fluids are not in the critical region (Crone and Wilcock, 2005). However, the elevated compressibility of critical fluids would enhance lateral pressure gradients and augment subsurface mixing that may be ongoing. Furthermore, the observation of critical fluids at the seafloor in southern MEF in 1999 (Lilley et al., 2003, Seyfried et al., 2003) is consistent with the presence of subsurface critical fluids less than a year later. This scenario may also explain why the hotter vents in the southern MEF exhibit tidal mixing, while the cooler vent to the north does not. However, we cannot rule out the possibility that the physical properties of local upflow zones, such as permeability, vary from north to south and that this variance accounts for the absence of tidal mixing at Grotto.

At the MEF, fluids with chloride concentrations between 1-3 Wt.% NaCl and temperatures of ~400°C are very close to their respective critical points at 550 m beneath the seafloor (Povodryev et al., 1999) which approximately coincides with the layer 2A/2B transition (Cudrak and Clowes, 1993; Van Ark et al., 2007). Under critical conditions, fluid compressibility increases dramatically (Johnson and Norton, 1991) and we can expect mixing involving critical fluids to be extremely dependent on pressure fluctuations. It is important to note that in estimating brine temperature in section 4.2.1, we assumed a vapor temperature 32°C lower than the critical temperature for fluids with chloride ranging from 1-3 Wt.% NaCl (Table 9). We address this discrepancy in more detail below in section 4.2.3.

Numerical modeling indicates that the layer 2A/2B interface is the maximum height within the crust at which subsurface brines are likely stored (Fontaine and Wilcock, 2006) so mixing at this depth is consistent with brine distribution. This interface is also the point at which rock permeability increases dramatically (Cudrak and Clowes, 1993; Van Ark et al., 2007) such that tidally driven mixing within this region is likely to show only a minimal lag with respect to pressure (Crone and Wilcock, 2006; Larson et al., 2007) or no lag at all (Table 8). Thus, we postulate that mixing involving a near-critical, chloride depleted vapor may occur at or just beneath the layer 2A/2B interface.

The mixing depth is calculated for each vent assuming critical conditions for the vapor phase. Critical conditions for each vent are calculated using the average chloride measured in the fluid samples from the given vent (Povodryev et al., 1999). Depth of the critical point for the range of observed chloride concentrations ranges from 486 to 695 m below the seafloor (Table 10).

Table 10. Temperature (Tc), pressure (Pc) and depth below the seafloor (dc) of the critical point as calculated for the average chloride measured in fluid samples at each vent using the equation of Povodryev et al. (1999). Average Milli-Q chloride concentration was calculated from chloride measurements reported in Larson et al. (2007)

Vent	Avg. Chloride (mmol/kg)	T_c (°C)	P_c (bars)	d_c (m)
Bastille	386	400	280	585
Cannaport	331	397	273	516
Milli-Q #1	347	398	275	536
Sully #1	309	396	270	486
Sully #2	341	398	275	528
S&M	469	405	291	695
Puffer	423	402	285	636
Grotto #2	455	404	290	678
3.2 Wt.% NaCl	566	408	301	789

A schematic of the mechanism and location of the putative mixing process is shown in Figure 25. The spatial context of the mixing is shown in Figure 25a and a cartoon of what this section of rock might look like has been modified from Fontaine and Wilcock (2006) and is shown in Figure 25b. An idealized plan view of a cross section of the upflow zone is shown in Figure 25c along with a cartoon of the relative volumes of vapor and brine at low and high tide. At low tide, the vapor end-member has a volume, V_0, and is surrounded by a film of brine. At high tide, an increase in pressure relative to low tide results in a reduction of the more compressible vapor by a volume ΔV which is compensated by an influx of cooler and less compressible brine, thus generating the chloride and temperature oscillations we observe.

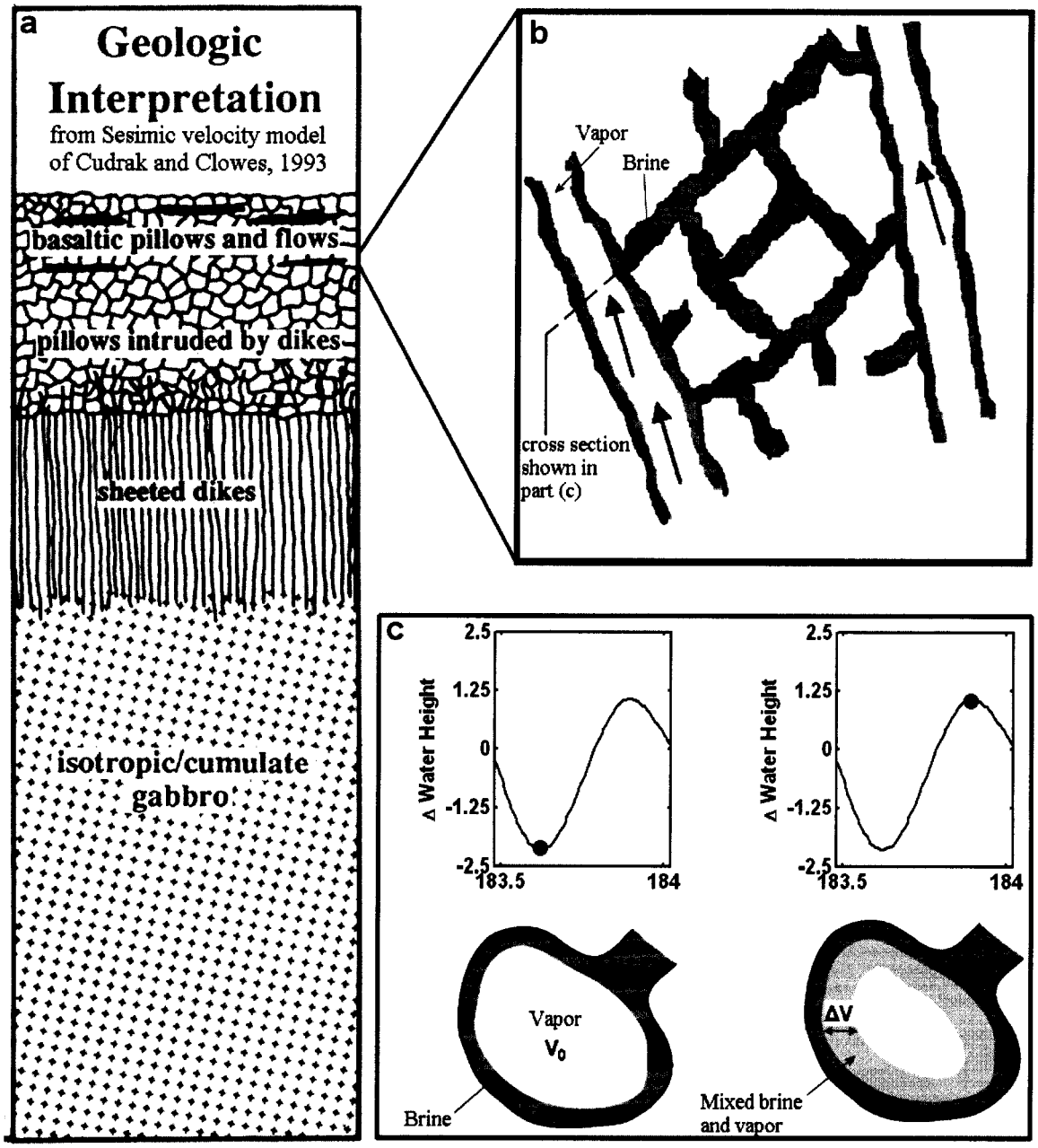

Figure 25. (a) Schematic of crust beneath MEF modified from Cudrak and Clowes (1993). (b) Cartoon of subsurface vapor and brine distribution at layer 2A/2B interface modified from Fontaine and Wilcock (2006). (c) Cartoon of subsurface mixing between brine and critical vapor end-members for the slice denoted by the line in the upper left portion of panel (b)

4.2.3 Differences between subsurface and seafloor fluid temperature

In calculating brine temperature, we used the maximum temperature observed during an oscillation as the vapor temperature (366.5°C in our example) but the criterion of pressure sensitivity requires a critical vapor temperature for 2 Wt.% NaCl of ~398°C. The discrepancy is likely due to the fact that fluid temperature measured at the seafloor is cooler than fluid temperature 550 m beneath the surface. A 2 Wt.% NaCl fluid with 2100 J/g intersects it's critical temperature of 398.3°C at 275.7 bar (Figure 26). Adiabatic cooling of the fluid as a result of decompression from 276 to 220 bars during ascent results in a 22°C decrease in fluid temperature (Figure 26). The fluid would have to be cooled an additional 10°C for fluid temperature to match observations in our example. This amount of cooling is consistent with estimates of conductive cooling in chimneys (Seewald and Seyfried, 1990) and subsurface upflow zones (Baker et al., 2004).

Using a value of 398 °C for the vapor, calculated temperatures from Table 9 for the various brines, and mass fractions comparable to those in Table 9, the temperature version of equation (4) yields an amplitude of ~2°C for temperature oscillations at their point of origin. This result is ~1°C higher than the observed maximum amplitude at the seafloor. A 50% reduction in oscillation amplitude is consistent with the dampening of subsurface temperature oscillations during ascent by equilibration with wall rock (Wilcock, 2004). If temperature oscillations are sufficiently dampened, they could disappear altogether, which could be one explanation for why some vents exhibit no temperature oscillations. However, the phase lag predicted to accompany oscillation dampening is not apparent (see section 4.1.2). Cleary, this bootstrapping method of calculating brine temperature can only give very rough numbers due to the non conservative nature of temperature in hydrothermal upflow zones.

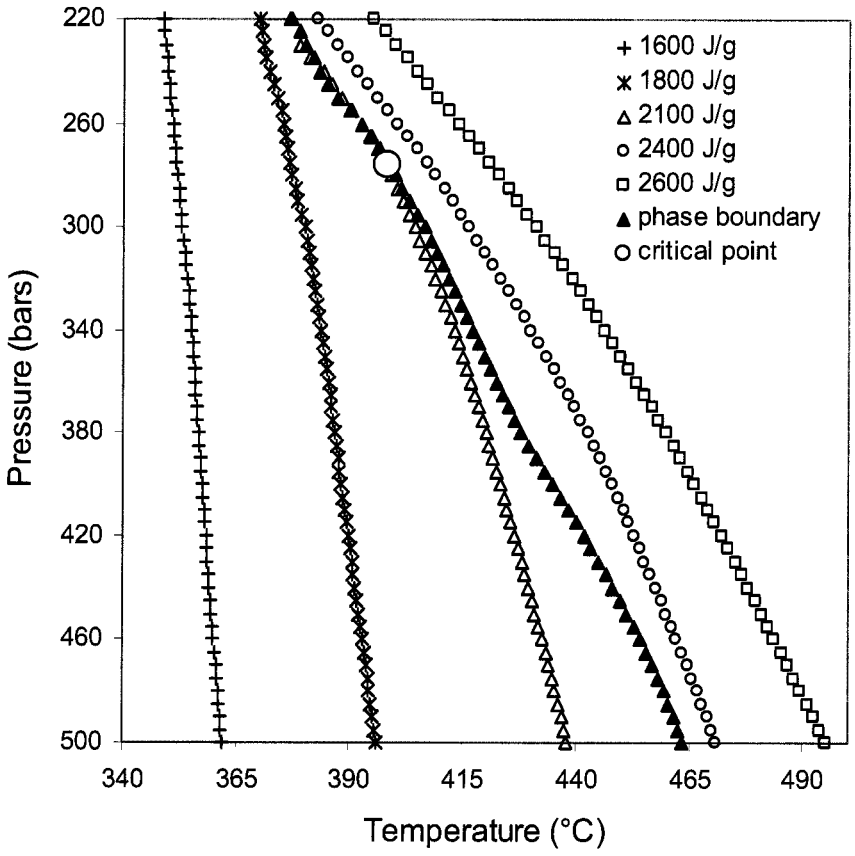

Figure 26. Isenthalps, two-phase boundary and critical point for 2.0 Wt.% NaCl calculated with the program developed by Berndt et al. (2001) and plotted in pressure-temperature space.

4.2.4 Vapor properties

We can use brine fractions and properties calculated in section 4.2.1. to calculate isothermal compressibility, β, of the vapor end-member (1.95 Wt.% NaCl for our example), and thus proximity to its critical point, using the equation given by Johnson and Norton (1991).

(5) $$\beta = \frac{-\Delta V}{V_o \times \Delta P}$$

ΔV represents change in volume of a fluid with initial volume V_0 for a given change in pressure ΔP. If we assume that 1 kg of vent fluid is a linear mixture of a vapor end-member and a brine end-member, then V_0 is the initial volume of the vapor and the change in volume, ΔV, is compensated by an influx of brine for a change in hydrostatic pressure, ΔP.

Equation (5) as written gives only a rough estimate of fluid compressibility because it assumes an instantaneous pressure change and a static parcel of fluid. In reality, tidal pressure changes occur over time in a flow-through system. Rigorous numerical treatment of such a system is beyond the scope of this research. Nevertheless, we use the approximation as a first order to way to probe the possibility that critical or near-critical fluid exists in the upper crust many months after a heat pulse. Rewriting this equation with the mass fractions and brine properties calculated in section 4.2.1. yields an equation relating isothermal compressibility to parameters that can be either measured or calculated:

$$(6) \quad \beta = \left(\frac{m_b}{\rho_b}\right) \times \left(\frac{\rho_v}{1-m_b}\right) \times \frac{1}{\Delta P}$$

where m is fluid mass, ρ is fluid density and b and v indicate brine and vapor respectively. Brine masses for a given chloride concentration are taken from Table 9 assuming 1 kg of vent fluid. For vapor density, we assume our example fluid (1.95 Wt.% NaCl) is near its critical point of 275 bar and 398°C and we calculate fluid density with a program developed by Berndt et al. (2001). For brine density, we use the critical pressure for the vapor end-member and assume temperatures as calculated in section 4.2.1. The measured pressure change for this time period, 0.27 bars, is used for ΔP.

For the conditions we've described, compressibility ranges from 3.92×10^{-2} to 1.30×10^{-3} bar^{-1} for 6 to 65 Wt.% NaCl respectively (Table 6). An analogous calculation was performed for Cannaport for the half tidal cycle from day 172.2 t o172.5 and results

are comparable to Milli-Q (Table 11). Calculated compressibility values in Table 11 are an order of magnitude higher than non-critical fluids (Rogers and Pitzer, 1982) and are within the range of values measured for critical water (Johnson and Norton, 1991). Thus, the existence of subsurface near critical fluids is a reasonable supposition.

Table 11. Properties of vapor and brine end-members. Brine mass is calculated from mass fraction of brine in Table 6 assuming a 1 kg parcel of vent fluid. Vapor densities are calculated using code developed by Berndt et al. (2001) and assuming critical conditions of 275 bars and 398°C. Brine densities are calculated assuming 275 bars and appropriate temperatures from Table 9. Isothermal compressibility is calculated using equation (6) and the specified parameters for the half tidal cycle at Milli-Q from day 181.5 to day 181.8 and at Cannaport from day 172.2 to day 172.5.

Parameter	Milli-Q			Cannaport		
S_b - (Wt.% NaCl)	6	25	65	6	25	65
ΔP (bars)	0.27	0.27	0.27	0.13	0.13	0.13
m_b (g)	19.8	3.5	1.3	12.1	2.2	0.8
ρ_v (g/cm^3)	0.4	0.4	0.4	0.4	0.4	0.4
ρ_b (g/cm^3)	0.75	1.10	1.43	0.75	1.10	1.43
$\beta \times 10^{-2}$ (bars^{-1})	3.92	0.46	0.13	4.90	0.59	0.17

This calculation was repeated for all vents where oscillations in chloride concentrations were measured (Table 12). For vents without clear temperature oscillations, no constraints can be placed on brine temperature, which limits our ability to estimate brine density. This limitation can be tolerated given the fact that brine density does not vary significantly over a wide range of temperatures (Berndt et al., 2001). Calculated compressibility values for effluent from Bastille and Sully, assuming 25 Wt.% brine, are ~2× higher compared with Milli-Q and Cannaport (Table 11). This indicates subsurface conditions at Bastille and Sully are closer to the critical point than conditions at Milli-Q and Cannaport.

This calculation assumes the vapor end-member bears the full pressure change observed during the course of a tidal cycle. However, Crone and Wilcock (2005) show that tidal loading is distributed between both rock matrix and pore fluid with distribution coefficients for each medium ranging from 0 to1. If a portion of a pressure perturbation is born in part by the rock matrix, then vapor compressibility would need to be even higher

to yield the required volume change while bearing a smaller portion of the pressure change.

Table 12. Isothermal compressibility calculated using equation (6) and specified parameters for selected portions of data from vents at which we observe chloride oscillations but no temperature oscillations.

Parameter	Bastille	Sully #1	Sully #2
Time (year days)	181.6-181.9	167.6-167.9	239.5-239.8
ΔP (bars)	0.28	0.22	0.27
S_b - (Wt.% NaCl)	25	25	25
X_b	0.0070	0.0043	0.0057
m_b (g)	7.0	4.3	5.7
ρ_b (g/cm^3)	0.95	0.95	0.95
ρ_v (g/cm^3)	0.40	0.40	0.40
$\beta \times 10^{-2}$ (bars^{-1})	1.07	0.83	0.82

4.2.5 A unique mixing regime

A 2.0% NaCl fluid at 398°C and 275 bars is very near its critical point (Figure 26) and has a density of ~0.4 g/cm^3 (Table 11) and volume changes are less than 2% of the 2.5 L occupied by 1 kg of near-critical fluid. Thus, the picture that emerges from this analysis is a chloride-depleted vapor ascending from the hydrothermal root zone and approaching its critical point at the interface between layers 2A and 2B. The resulting near critical fluid is especially sensitive to pressure changes such that increases in hydrostatic pressure compress vapor slightly and drive lateral flow of very small amounts of surrounding cooled brine into the upflow zone where vapor and brine are mixed to vent as a homogenized fluid at the seafloor. Time series measurements at an orifice venting such a mixed fluid would show chloride and temperature changes that vary in concert with tidal pressure oscillations, while chloride concentrations could remain below seawater values. In this way, brine may be slowly removed from a hydrothermal system without vent fluid chloride ever exceeding seawater concentrations.

4.3. Temporal Context and Chloride flux

4.3.1 Temporal context

Six months after the 1999 event at the MEF, other investigators measured chloride concentrations of 10 mmol/kg chloride and temperatures of 380°C (Lilley et al., 2003; Seyfried et al., 2003). Seafloor pressure at the MEF is ~220 bars such that a nearly freshwater fluid at 380°C is very close to its critical point (Bischoff and Pitzer, 1989). Twelve to fifteen months after the event, we hypothesize that critical fluids are circulating at depths between 486 and 695 m (Table 10). This apparent downward shift in the vertical position of the critical point occurred at the same time that a shift in PT conditions of subsurface phase separation produced vapor phases with increasingly higher chloride concentrations (Lilley et al., 2003).

Thus, in the summer of 2000, we speculate that increasingly saline vapors encountered near critical PT conditions in a part of the crust where brines accumulate (Fontaine and Wilcock, 2006) and permeability increases (Cudrak and Clowes, 1993). These unique circumstances enabled tidally sensitive subsurface mixing. However, as the heat pulse from the magmatic intrusion subsided, fluids move away from the critical region. Although mixing may continue to occur, we expect the process to be much less sensitive to tidal pressure oscillations. This expectation is consistent with time series chloride observations made at Sully in 2004 (Lilley, unpublished data).

4.3.2 Chloride flux

Estimates of the rate at which brines accumulate beneath the MEF have been calculated by Fontaine and Wilcock, 2006. Here, we use brine mass fractions from Table 9 and Table 12 in conjunction with estimates of hydrothermal mass flux to approximate the quantity of brine extracted via subsurface mixing. The amount of brine mixed with vapor per kilogram of vent fluid at high tide is given by equation (4). Assuming a 25 Wt.% brine, we use an average brine mass fraction for all southern vents of $X_b = 0.005$. At low tide, vent fluid is assumed to be pure vapor such that over the course of a tidal

cycle, the amount of brine removed is roughly half the amount removed at high tide. Thus, for fluid venting from structures in the southern portion of MEF, approximately 2.5 g of 25 Wt.% brine is removed per kilogram of vent fluid.

Total hydrothermal mass flux, Q_m, is given by the equation (7) from Turcotte and Schubert, 2002:

$$(7) \quad Q_m = \frac{Q}{H}$$

where Q is total hydrothermal heat flux for MEF and H is enthalpy of the fluid. Heat flux for MEF has been measured by Veirs et al (2001) as 600 MW but we use one quarter of this value to represent heat flux from southern MEF because previous research suggests distinct subsurface plumbing beneath southern and northern portions of MEF (Tivey and Johnson, 2002) and equal distribution of local heat flux between focused high temperature flow and diffuse flow (Veirs et al., 2006).

For fluid enthalpy, we use mixing zone conditions to estimate mass flux within this region. The median pressure of mixing from Table 10 is approximately 279 bars and the mean temperature of critical fluids with chloride concentrations from Table 10 is approximately 400°C. Although heat capacity is not available for the chloride concentration range of interest, Bischoff and Rosenbauer (1985) report a heat capacity of approximately 1944 J/g for a 3.2 Wt.% NaCl solution at 279 bars and 400°C.

With parameters as outlined above, we calculate a hydrothermal mass flux through the mixing zone of 77 kg/s. which is about half the mass flux measured by Converse at al. (1984) for seafloor chimney structures. This difference is consistent with a lower permeability in subsurface upflow zones compared with seafloor vent structures. Based on this mass flux and the amount of brine removed per kg of vent fluid, we calculate that 25 Wt.% brine can be removed at the rate of 192 g/s from each of the

southern structures. Assuming a brine density of 1000 kg/m^3 for fluids in the 5 vent structures where we observe chloride oscillations, this removal rate equates to 9.6×10^{-4} m^3/s. This is only 14% the estimated accumulation rate for 25 Wt.% brines (Fontaine & Wilcock, 2006). Because the phenomenon is likely transient, this mechanism of brine removal can account for only a small portion of brines produced and stored subsurface. Thus, in the absence of evidence of chronic brine venting at MEF, brines must either have long residences times or migrate within the crust to vent at other locations.

4.4. Fluid circulation prior to mixing

From the depth and temperature constraints imposed by the putative mixing process, we can also speculate about other portions of the fluid circulation pathway prior to mixing. Conditions for the root zone of the MEF hydrothermal system have been estimated by several studies. Seyfried et al. (2003) place the temperature of initial phase separation at 418°C just after the 1999 magmatic event. At this temperature, a 3.2 Wt.% NaCl solution (a seawater analog) intersects the two phase boundary at 327 bar (Bischoff and Pitzer, 1989). The maximum depth of hydrothermal circulation is limited by the depth of the feeder magma lens which has been placed by seismic reflection studies at ~2.6 km beneath the surface (Detrick et al., 2002). This depth equates to a pressure of 480 bars at which seawater must be 477°C to undergo phase separation. Although more recent research indicates a shallower depth of the axial magma lens (Van Ark et al., 2007), here we consider the deep end of the range of possible conditions at which seawater may first enter the two-phase region, 480 bars and 477°C.

A 2.0% NaCl solution intersecting its critical point at 276 bars and 398°C has an enthalpy of 2100 J/g (Figure 26). Assuming the fluid has ascended adiabatically from the root zone, fluid temperature at 480 bars will be 435°C (Figure 26). However, seawater at 480 bars must be 42°C hotter to phase separate (Figure 27). For phase separation to produce a 2.0% NaCl solution from a seawater precursor, the temperature at 480 bars must be 490°C (Figure 27). A 2.0% solution at 490°C and 480 bar has an enthalpy of

2600 J/g (Figure 26). Decompression of this fluid to 275 bars results in an adiabatic temperature decrease from 490°C to 421°C. Thus, in order for a 2.0% NaCl solution at 490°C and 480 bars with an enthalpy of 2600 J/g to intersect its critical point at 275 bars and 398°C with an enthalpy of 2100 J/g, the fluid must loose approximately 500 J/g, which equates to 23°C of non-adiabatic cooling. This estimate is consistent with research by Baker et al. (2004) which holds that conductive cooling in the wake of a magmatic event can account for a significant amount of heat loss.

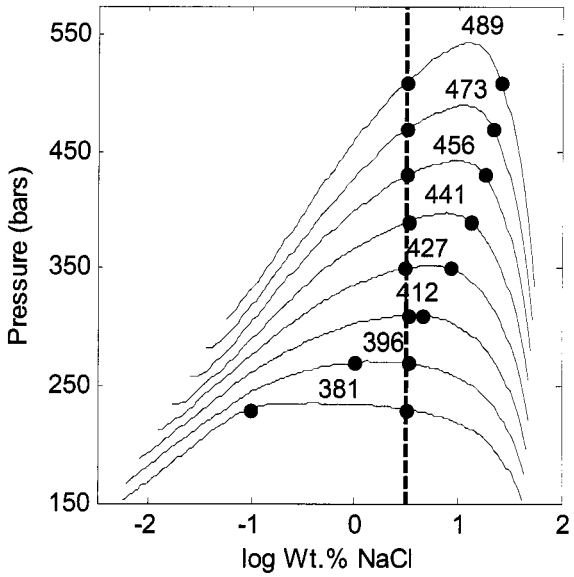

Figure 27. Isotherms showing composition of conjugate vapors and brines produced by phase separation of 3.2 Wt.% NaCl (modified from Bischoff and Rosenbauer, 1989). Isotherm labels are in units of °C and the dashed line shows the concentration of seawater analogue, 3.2 Wt.% NaCl. Subcritical phase separation, or boiling, generates a vapor phase depleted in chloride with respect to seawater. Supercritical phase separation, or condensation, generates a brine phase enriched in chloride with respect to seawater.

The foregoing analysis assumes that once a 2.0% solution has been produced by phase separation of seawater and segregated from its conjugate brine, the resulting fluid maintains a constant NaCl concentration during ascent to the point of mixing. However, because the 2.0% fluid in the example above remains in the two phase region until mixing occurs at 275 bars, phase separation and segregation is likely ongoing during

ascent (Seyfried et al., 2003). Furthermore, enthalpy of a bulk fluid partitions preferentially into the vapor phase (Berndt et al., 2001). Thus, a more robust estimate of the magnitude of conductive cooling would require numerical modeling similar to the study performed by Seyfried et al. (2003) but with boundary conditions representing the mixing zone rather than the seafloor.

These complications do not affect our analysis of fluid ascent after mixing as the addition of small amounts of cooled brines (in the case of Milli-Q and Cannaport) shifts the resulting mixture off the two-phase curve. Even for fluids where the brine end-member may not have been substantially cooler (as with Bastille and Sully), the adiabatic cooling path coincides with the phase boundary (Figure 26) such that any amount of conductive cooling shifts the mixture to the one-phase region.

4.5. Spatial variability in time series measurements

Thus far, we have concentrated on numerical analyses of tidal oscillations in chloride concentration and, in some cases, temperature of vent effluent. However, as is clear from sections 3 and 4.1, variability is observed not only in the character of the tidal signature at each vent, but also in non-tidal changes measured at each vent. Below, we consider this variability and its implications for vapor and brine distribution.

4.5.1 North-South variation

One of the most pronounced differences between data from the northern portion of the MEF and data from the southern portion is the absence of a tidal signature in the northern vent, Grotto (Larson et al., 2007 and Figure 19,Figure 21 and Figure 22). The absence of a tidal signature indicates that subsurface mixing is not occurring beneath Grotto. One explanation is that ascending hydrothermal fluid beneath Grotto does not intersect its critical point. Fluid from the first Grotto record has a lower temperature and higher chloride concentration than any other vent for which we have data (Larson et al., 2007 and Figure 16–Figure 20). The critical point occurs deeper within the crust and

requires a higher temperature than fluids with a lower chloride concentration (Table 10). Under these conditions, the absence of shallow near critical fluids would make the Grotto fluids less sensitive to tidal loading.

It is important to note that there are southern vents with either chloride concentrations or temperatures comparable to Grotto where we do observe a tidal signature, but none of these have both lower temperatures and higher chloride concentrations than Grotto. Chloride in a fluid sample taken at S&M is 469 mmol/kg (Table 7) which is higher than mean chloride at Grotto, but the temperature at S&M is also 4-9°C higher than at Grotto. For portions of the data records from Cannaport and Milli-Q (Figure 17 and Larson et al., 2007), temperatures fall within the range observed during the second deployment at Grotto (Figure 19) but chloride concentration at these vents ranges from 61 to 137 mmol/kg lower than chloride at Grotto. Essentially, critical fluids may not have been viable at Grotto given its chloride concentrations and inferred subsurface PT conditions (Table 10).

The north-south variation in tidal character may depend on physical characteristics of the upflow zones rather than on subsurface fluid properties. Based on the observations that fluid perturbations were greatest at Sully and Puffer after the 1999 magmatic event (Lilley et al., 2003), it's possible that the permeability in the south may have been more agitated than plumbing in the north. Under these circumstances, we might expect lateral pressure gradients in the south to be more responsive to tidal loading than in the north. The result would be a tidal signature in southern vents that is not readily apparent in northern vents.

4.5.2 Variation within the southern portion of MEF

Differences in the nature of the tidal signatures and in non-tidal changes at each vent are observed in all vents in the south part of the MEF. The most notable difference is that temperature oscillations occur at Milli-Q (Larson et al., 2007), Cannaport and S&M (Figure 17 and Figure 20) but not at Bastille and Sully (Figure 16Figure 18). Two of the

vents where we observe a tidal signature in temperature (Milli-Q and S&M) are located in the eastern part of the southern MEF and lie along the same fault line (Figure 15). These vents are also the furthest removed from the area most impacted by the 1999 magmatic event, Puffer and Sully (Lilley et al., 2003).

A strong tidal signature in temperature at Milli-Q and S&M may reflect the fact that brines produced near the site of the magmatic intrusion had more opportunity to cool before arriving at distal subsurface mixing zones beneath Milli-Q and S&M. Brines involved in subsurface mixing beneath Sully and Bastille would have originated much closer to their respective mixing zones and cooled less prior to mixing. This scenario implies a short residence time for subsurface brines (less than 15 months), which is consistent with results of Kadko and Butterfield (1998) who calculated brine residence times of 3 years or less. It must also be assumed that all brines originate from a common point. This is unlikely because variation in chloride across the field indicates different subsurface PT conditions for each vent.

Other investigators have estimated residence times from years to centuries (Lowell and Germanovich, 1997). Thus, it may also be possible that brines had been stored within the crust for an unspecified time prior to the 1999 event. In this case, brines located beneath Bastille and Sully would be heated more by the proximal magmatic intrusion than brines located further away beneath Milli-Q and S&M. The hotter brines would cool the hydrothermal mixture less than brines with lower temperatures. The result would be the dampening of temperature oscillations at Bastille and Sully. Given the similar temperatures for all these vents, it must be assumed that the dominant vapor phase at each vent undergoes relatively uniform cooling during ascent to the mixing zone despite spatial variability in the temperature of brines stored in the rock

Cannaport is close to the area most influenced by the 1999 event and it also exhibits tidal oscillations in temperature (Figure 22b). The tidal signature in Cannaport's chloride concentration record is weaker (Figure 21e) and the fluid temperature lower than other southern vents (Figure 16 and Figure 20). This indicates a cooler brine end-member

in the subsurface than nearby Bastille and Sully. Such dramatic differences over distances less than 50 m are consistent with research by Lilley et al. (2003), which shows that adjacent vents may exhibit different hydrothermal responses to a magmatic event. For instance, chloride concentration at Bastille increases slightly from 1998 to 1999 while chloride concentration at Puffer about 20 m away drops off dramatically during the same period.

4.6. Non-tidal temporal variability

4.6.1 Northern MEF

The most pronounced variability at Grotto occurs in September of 2000. Positive Non-tidal chloride excursions coincide with the portion of the record when we observe the greatest variability in temperature (Figure 19). These chloride variations were recorded after a 4°C increase in mean temperature from the June deployment at Grotto (Larson et al., 2007). However, there is no record of when and how the temperature increase occurred. Chloride spike magnitudes are comparable to or only slightly above seawater chloride concentration and may reflect propagation of a cracking front (Lister, 1974) and coincident release of either heated seawater or brine inclusions that may be stored in the host basalt (Fornari et al., 1998; Sohn et al., 1998).

4.6.2 Southern MEF

Non-tidal temporal variability in southern vents can be classified as one of two types: 1) rapid changes that disrupt the tidal signature, such as the spike in chloride at Sully on day 183 (Figure 18) and 2) changes occurring over longer time scales, such as the gradual rise in chloride at Sully at the beginning of the record (Figure 18). In the second type, the tidal signature is superimposed on the overall trend.

One example of the second type is the gradual chloride increase at Sully from day 180 to day 206 (Figure 18) where mean chloride rises from 309 to 396 mmol/kg (1.77 to 2.26 Wt.% NaCl). This observation can be explained by a shift in the temperature or

pressure of subsurface phase separation of seawater (Figure 27). This increase equates to a 4°C decrease at 480 bars from 493 to 489°C, a 7 bar increase at 490°C from 474.5 to 481.5 bars, or some combination of both increased pressure and decreased temperature. This shift is consistent with increasingly deeper penetration of hydrothermal flow into a cooling magmatic intrusion.

Examples of the first type are the rapid increases in Puffer temperature before and after day 190 (Figure 20), each of which is followed by a more gradual decline. These features, which also occur at Bastille (Figure 16) Sully (Figure 18), may represent propagation of a cracking front and subsequent hydrothermal cooling of freshly exposed hot rock (Fornari et al., 1998; Sohn et al., 1998; Lister, 1974).

Although the Puffer temperature record has features similar to other vents, it is also unique. In addition to temperature oscillations that correlate directly with seafloor pressure, rather than inversely as with other vents, Puffer exhibits both positive and negative temperature excursions throughout the data record. These observations suggest that fundamentally different processes are at work within the hydrothermal system feeding Puffer compared with neighboring vent structures. However, without coincident chloride measurements or other chemical data we are unable to determine the cause of this unique temperature variability at Puffer.

4.7. Crustal heterogeneity

In general, differences in the tidal signature of effluent issuing from the MEF vents and the lack of coherence in non-tidal variability over spatial scales as small as a few meters indicate highly complex fluid circulation pathways and a heterogeneous crustal structure beneath MEF. Our results also indicate that the response of a hydrothermal system after a magmatic event manifests itself not only in dramatic event plumes (Baker et al., 1998) but also in local processes, like subsurface mixing, that change over timescales on the order of months and years.

5. Conclusion

An array of in situ chloride sensors were deployed at the MEF 12-15 months after an intrusive magmatic event occurred there. The intrusion produced profound changes in the chemistry of 360-380°C hydrothermal fluids from the southwestern part of the vent field. A strong tidal signature in effluent from several of these vents is likely the result of subsurface mixing between non-seawater end-member fluids at or just beneath the interface between crustal layers 2A and 2B.

One end-member fluid may be a compressible near-critical chloride-depleted vapor phase at a temperature of approximately 400°C. The other end-member fluid is likely a pre-existing chloride-enriched brine with temperatures ranging from 131°C to 326°C for brines ranging from 6 Wt.% NaCl to 25 Wt.% NaCl. These temperatures likely represent only approximate values. Brine properties may vary across the MEF with those hosted closer to the site of magmatic intrusion being heated to a greater extent than less proximal brines.

Absence of a tidal signature in the northern portion of MEF suggests subsurface conditions in the North were not sufficiently perturbed to enable tidally sensitive subsurface mixing. Spatial and temporal variability in non-tidal changes in fluid temperature and composition are consistent with a highly heterogeneous upper crust in which subsurface controls for Puffer vent are different than for the neighboring vents. Further observation of this variability using high resolution time series measurements is essential to elucidating properties of subsurface fluids and micro-scale structure of circulation pathways.

Chapter 4 – The East Pacific Rise at 9°50'N

Evidence of brine expulsion and constraints on pressure and temperature of hydrothermal circulation inferred from in-situ measurements of chloride and temperature 9-14 months before the 2006 eruption at 9°50' N on the EPR

Summary

An in-situ conductivity sensor was deployed to measure chloride and temperature of high temperature flow from Bio 9' vent at 9°50'N along the East Pacific Rise 9-14 months prior to an eruption. Phase separation is a dominant control on chloride at this fast spreading ridge and in situ measurements are necessary to thoroughly characterize the behavior of fluids within the dynamic Bio 9 hydrothermal system. Here we report chloride and temperature data collected at 1 min intervals showing unprecedented temporal detail of the hydrothermal response to periods of intense seismicity on Nov. 27. and Dec. 17, 2004. We observed a maximum chloride value of 720 mmol/kg, the highest chloride yet measured at this vent. Using maximum and minimum chloride concentrations, our calculations suggest that phase separation is occurring at 288 bars and 403.5 °C. Changes in chloride in the wake of Dec. 17 seismicity suggest a drop in pressure and temperature (PT) conditions to 269 bars and 396.7°C. The shift occurs over a period of 6 days then rebounds over a period of 2 weeks, indicating only a transient change in flow patterns. We also observe recurring chloride spikes throughout the record ranging from 1.5x to 3x higher than typical baseline values and lasting anywhere from 1 min to 7 mins. This pattern is consistent with continuing but intermittent brine venting.

1. Introduction

It has long been hypothesized that episodic dike intrusions and seafloor eruptions are the primary mechanism through which seafloor spreading occurs at mid-ocean ridges (Delaney et al., 1998; German and Lin 2004) and hydrothermal response to these events has been shown to be highly dynamic (Baker et al., 1998, Butterfield et al., 1997, Lilley et al., 2003; Von Damm et al., 1995). In the case of the fast-spreading East Pacific Rise between 9-10° North latitude (9N), two such periods of activity have been observed, one in 1991-1992 (Von Damm et al., 1995; Von Damm, 2000; Fornari et al. 2004) and another more recently in 2005 (http://ridge2000.org/science/tcs/epr06activity.html; Tolstoy et al., 2006). The hydrothermal response to each of these events has been thoroughly characterized by measurements made in the immediate aftermath of the event (Von Damm, 2000; http://ridge2000.org/science/tcs/epr06activity.html). However, much less hydrothermal chemical data is available for the period of time preceding a diking event.

Although spreading events are episodic (Delaney et al., 1998; Haymon et al., 1991; Henstock et al., 1993), seafloor spreading is unpredictable and it is difficult to observe the hydrothermal activity prior to an event with discrete fluid samples. Thus, long term in situ chemical measurements are needed to increase the likelihood of monitoring fluid chemistry before during and after a diking event. To this end, we deployed an in situ device capable of measuring chloride and temperature of 'black smoker' fluids (Larson et al., 2007) in a high temperature vent along the EPR for a period of time 9-14 months prior to the 2005 eruption at 9N. The data collected by this instrument package provides unprecedented detail of the activity at a ridge-hosted hydrothermal vent leading up to an extrusive event.

We can also use our data to address an observed chloride imbalance. Over the 15 years preceding the 2006 eruption, hydrothermal fluid leaving the Bio 9' system had

much lower chloride concentrations than the seawater entering the system (Von Damm, 2000; Von Damm, 2004; Von Damm, pers comms). Better temporal resolution may help to resolve the issue of the apparently missing chloride. In addition, the dominant control on chloride, phase separation, is influenced primarily by pressure and temperature (Bischoff and Pitzer, 1989). Thus chloride measurements can be used to elucidate portions of the fluid circulation pathway prior to venting.

In this paper, we discuss measurements of chloride and temperature collected at 1 minute intervals by an instrument deployed in Bio 9' vent at 9°50'N from November 2004 to March 2005. This dataset represents the most detailed record to date of the temporal variability of high temperature hydrothermal fluid chemistry. On the basis of this data and co-recorded measurements of ridge seismicity made by M. Tolstoy, we are able to infer removal mechanisms for chloride enriched brines previously unobserved at this vent. We also constrain pressure and temperature (PT) conditions of hydrothermal circulation and discuss residence time of subsurface brines within the upper crust. Finally we discuss evidence of incomplete phase segregation and implications of this phenomenon for root zone conditions inferred from PT conditions of phase separation.

2. Experimental Site

2.1. Experimental site

Bio 9' Vent is located at 9°50'N and 104°17'W along the fast spreading magmatically robust East Pacific Rise (Figure 28). The portion of the EPR hosting Bio 9' vent is characterized by an axial high at 2500 m depth. An axial summit trough (AST), measuring 70 m wide and up to 5 m deep, runs through the middle of the summit and is thought to be the result of drainback and collapse of lavas extruded during eruptions occurring from 1991 to 1992 (Fornari et al., 1998). The Bio 9' orifice (Figure 28b) is located on the floor of the AST within a group of several chimneys collectively identified as the Bio 9 complex.

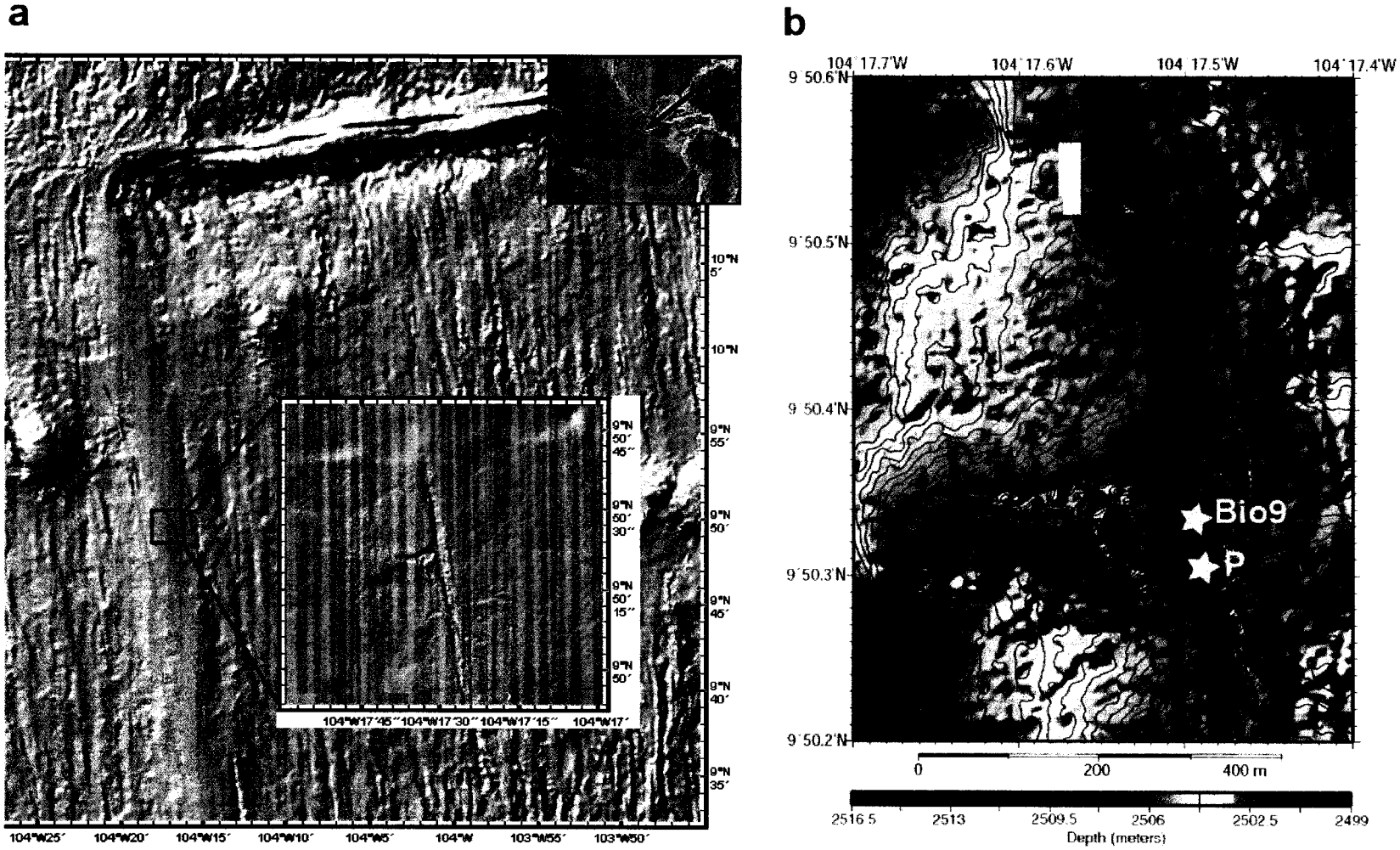

Figure 28. Map of East Pacific Rise showing (a) global and local position created using Ridge 2000 GeoMapApp software and (b) the portion of the ridge hosting the high temperature vent (Von Damm, 2004) where an in-situ sensor was deployed.

This section of ridge also exhibits a discontinuity in the wall of the AST, likely the result of erupted lava breaking through the wall (Fornari et al., 2004) which is consistent with the estimated location of lava extrusion.

The uppermost layer of crust beneath the seafloor consists of highly permeable extrusive volcanic rock (geologic layer 2A) extending down between 200 and 400 m (Sohn et al., 2004). This layer overlies a layer of sheeted dikes which, in turn, sits atop a magma lens that has been imaged at ~1.4 km beneath the seafloor (Detrick et al., 1987). An extensive description of ridge morphology and seismic structure can be found in papers by several other investigators (Detrick et al., 1987; Fornari et al., 2004; Fornari et al., 1998; Haymon et al., 1991; Kent et al., 1993; Sohn et al., 2004).

2.2. Site history

In 1991, the EPR at 9°50'N was the site of a volcanic eruption followed shortly by another in 1992 (Fornari et al., 2004; Von Damm et al., 1995). Since the 1991 eruption, the chemistry of hydrothermal venting in this area has been intensively monitored (Lilley et. al., 2003; Oosting and Von Damm, 1996; Scheirer et al., 2006; Von Damm et al., 1995; Von Damm, 2000; Von Damm, 2004; Von Damm and Lilley, 2004).

2.2.1 Post-eruptive period

When measurements were made in 1991, vent fluids were greatly depleted in chloride with respect to seawater and decreased even further in 1992 accompanied by a coincident increase in temperature in keeping with the intense phase separation usually observed in the wake of a magmatic event (Butterfield et al., 1997; Von Damm et al., 1997; Von Damm et al, 1995). After 1992, chloride concentrations began to rebound over the next 4 years, accompanied by a decrease in temperature, before topping out at values very close to seawater chloride, enriched for some vents, depleted for others (Von Damm, 2000). The rebound is consistent with deepening of hydrothermal circulation and cooling of the crustal magma body. However, it is worth noting that during the rebound, an

increase in CO_2 observed in late 1993 by Von Damm and Lilley (2004) suggests magma was re-supplied to the upper crust though no such signature was evident in the major and minor element chemistry.

2.2.2 Pre-eruptive period

After 1996, chloride concentrations in vent fluids issuing from the Bio 9 complex declined for almost ten years before leveling of at ~250 mmol/kg in 2005 (Von Damm, 2004; Von Damm, pers comms). This trend in chloride is suggestive of the upwards migration of magma within the crust (Von Damm, 2004) which is consistent with the timing of the extrusive event sometime between November 2005 and January 2006 (http://ridge2000.org/science/tcs/epr06activity.html). Temperature measurements made within this time frame showed a perturbation of fluid temperature at high temperature vents in November 1997, possibly the result of a short-lived perturbation of crustal permeability brought on by continuing magma migration (Scheirer et al., 2006).

2.2.3 Ridge Seismicity

Ridge seismicity was also measured during this time frame (Sohn et al., 1998; Tolstoy et al., 2006). A seismic event in 1995 and the ensuing temperature increase is likely the result of cracking in the rock and a deepening of hydrothermal circulation (Fornari et al., 1998; Sohn et al., 1998). Constraints from seismic observations indicate cracking occurred at a depth of 1.1 km (Sohn et al., 1998). However, it is not clear whether the cracking is hydrothermal or magmatic in nature since both scenarios can induce seismicity (Fornari et al., 1998; Lister, 1974; Van Ark et al., 2007).

Seismic measurements made in late 2004 and overlapping our in-situ chemical measurements show a very seismically active ridge (Tolstoy et al., 2006) in keeping with the chemical evidence of an impending eruption (Von Damm, 2004). Seismicity was not the only manner in which these instruments recorded the event. Several ocean bottom

seismometers were immobilized by lava flows originating from the 2005-2006 eruption (http://ridge2000.org/science/tcs/epr06activity.html).

2.2.4 Evolution of an active spreading center

The chemical and temperature evolution of venting and coincident seismic measurements paint a picture of a very active divergent boundary in which eruptions and dike injections in 1991-1992 were followed by a relatively quiescent period during which hydrothermal processes dominated (Von Damm, 2004; German and Lin, 2004). Beginning in 1996, magma began an upward migration within the crust, eventually extruding onto the seafloor in an eruption likely occurring Jan. 22, 2006 (Tolstoy, 2006; http://ridge2000.org/science/tcs/epr06activity.html).

3. Experimental Methods

3.1. Data collection

3.1.1 Resistivity-temperature data

It is within the pre-eruptive phase, during the upward movement of magma in the crust and prior to the extrusive event, that on November 21st, 2004, we deployed our instrument in Bio 9' vent at 9°50'N along the EPR (Figure 29) to make in situ measurements of chloride for a 5 month period. Chloride data discussed in this paper was collected with a sensor capable of measuring solution resistance the reciprocal of which, conductivity (V^{-1}), is a proxy for chloride (Larson et al., 2007). An Omega thermocouple, model TRC-III was situated next to the resistivity sensor to record fluid temperature.

3.1.2 Supplementary fluid chemistry data

Fluid samples were collected on November 23rd at the Bio 9 complex two days after instrument deployment during a fairly quiet portion of the data record. Samples were analyzed for chloride and magnesium (K. Von Damm, pers comms) and the end-

member chloride concentrations calculated by extrapolation to zero Mg. Our conductivity readings were normalized to these end-member chloride values for Bio 9' (averaging 260 mmol/kg). Instrument components, sensor calibration and conductivity normalization are described in detail in Larson et al. (2007). However, as described below, some sensor improvements have been made since the publication of that article.

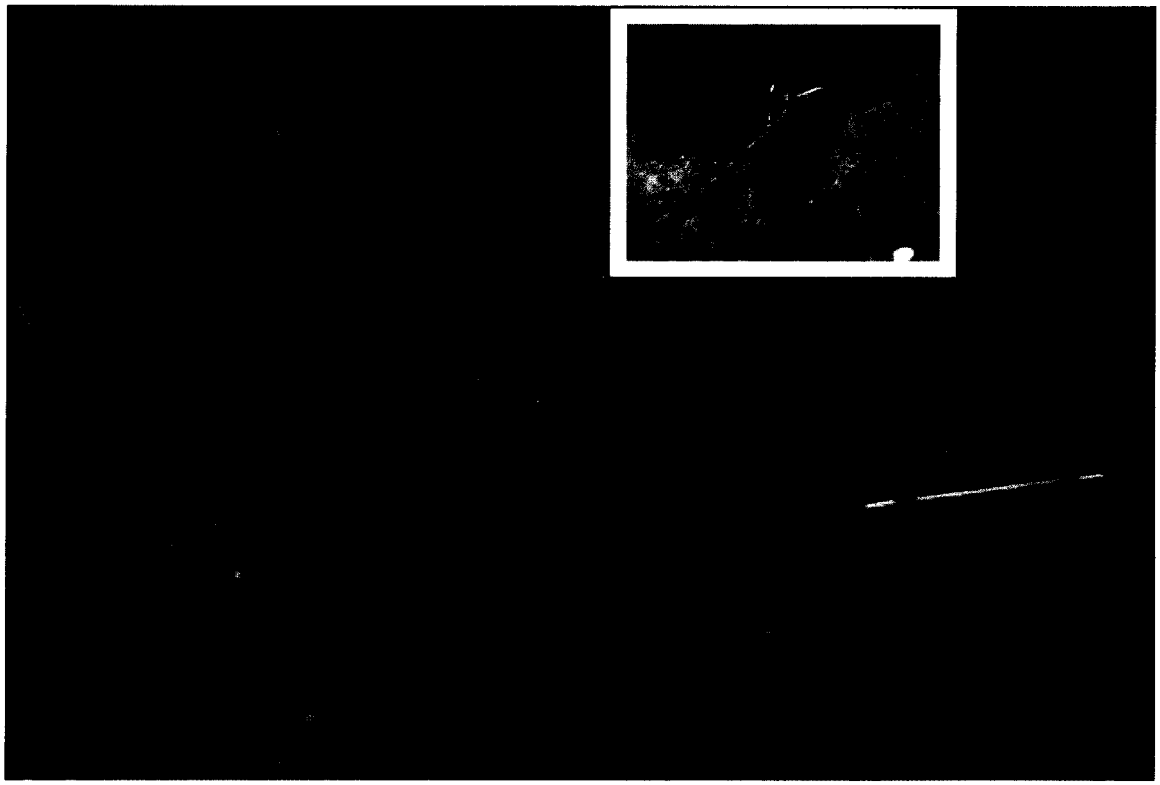

Figure 29. Photograph of the instrument package deployed at the experimental site. The inset shows a blown up image of the position of the sensor housing.

3.2. Instrument upgrades and sensor re-calibration

3.2.1 Instrument improvements

The 2000 version of the sensor originally consisted of 4 gold electrodes embedded in a zirconium oxide (ZrO_2) housing with 4 cylindrical cavities (Figure 30) and pressure

compensated by an oil reservoir. The upgraded sensor used in the Bio 9' deployment (2004 version) had 4 cone shaped titanium electrodes embedded in a ZrO_2 housing in which the cylindrical cavities were machined to a cone shape complimentary to the electrodes. A cone-shaped gold collar was also added to improve the metal/ceramic seal. All the electrode faces were then gold-plated (Figure 30).

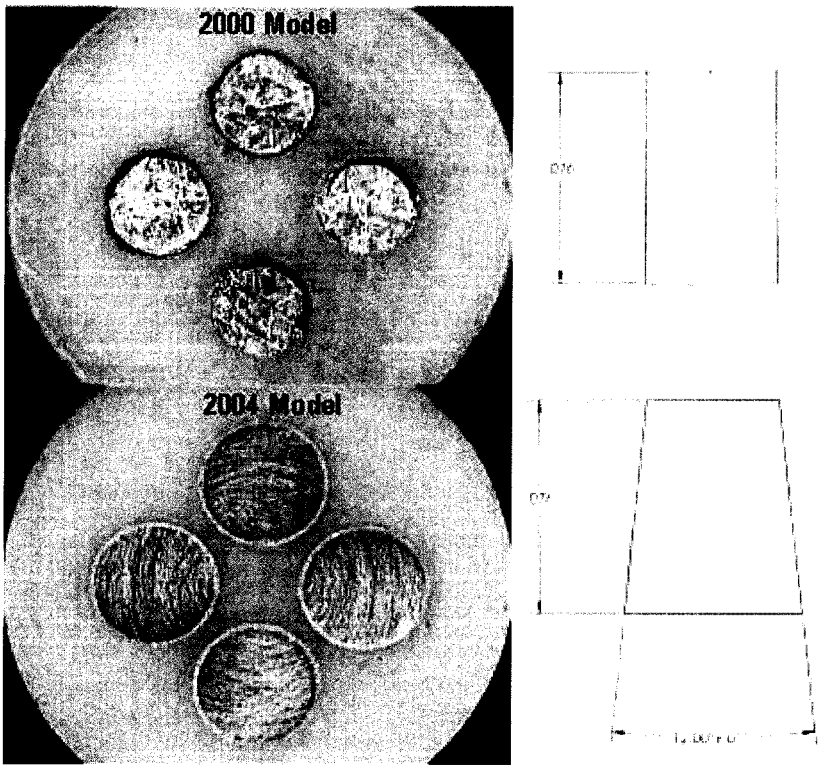

Figure 30. Photograph of sensor face and schematic of electrode cavity for 2000 and 2004 version of high temperature conductivity sensor. Improvements in the face seal from 2000 to 2004 eliminated the need for oil compensation.

The oil was removed such that the pressure gradient across the sensor face between ambient deep sea pressure and atmospheric pressure improved the seal by forcing the electrodes into their cone-shaped seats. The Bio 9' sensor was verified to be He-leak tight to at least 1×10^{-9} mL/min at atmospheric pressure and passed repeated pressure cycling between atmospheric pressure and 10,000 psi.

Instrument components were also upgraded to include the Tattle Tale version 8 processor which enables the use of flash memory cards and much larger data storage capacity than previously used Tattle Tale version 4 processors. The sensor housing was also upgraded to include thicker titanium to withstand the pressure gradient. In the instance of the Bio 9' instrument, however, a pure titanium tube bypass was placed at the corner of the sensor housing to facilitate instrument construction. It was overheating of this component as hydrothermal precipitation sealed the housing in high temperature flow that cause the tube to collapse and the instrument to fail after 5 months. We have since completely redesigned the sensor housing to eliminate this problem.

3.2.2 Sensor calibration

The 2004 sensor was calibrated as described in Larson et al. (2007) with the exception that the pressure and temperature conditions were chosen to represent seafloor hydrothermal conditions at 9°50'N. Pressures ranged from 250-300 bars, temperatures ranged from 200-396°C and NaCl formality (mmol/kg solution) ranged from 100-1500 mmol/kg. Experimental results are shown in Figure 31.

For all but the most concentrated solution at 387°C, pressure and temperature (PT) conditions put test solutions very near or squarely in the two-phase region where measurement of bulk fluid conductivity with our laboratory apparatus becomes difficult. Since we are not currently equipped to measure conductivity of each phase independently, we measured solution conductivity at conditions slightly away from the phase boundary and extrapolated the conductivity of the bulk two-phase fluid from these measurements.

After stabilizing pressure at 250 ± 2 bars, we measured conductivity for a range of solutions at 202, 251, 300, 350, 380, 383 and 387 ± 0.1°C (Figure 31a). We repeated the 380°C isotherm again at 300 bars.

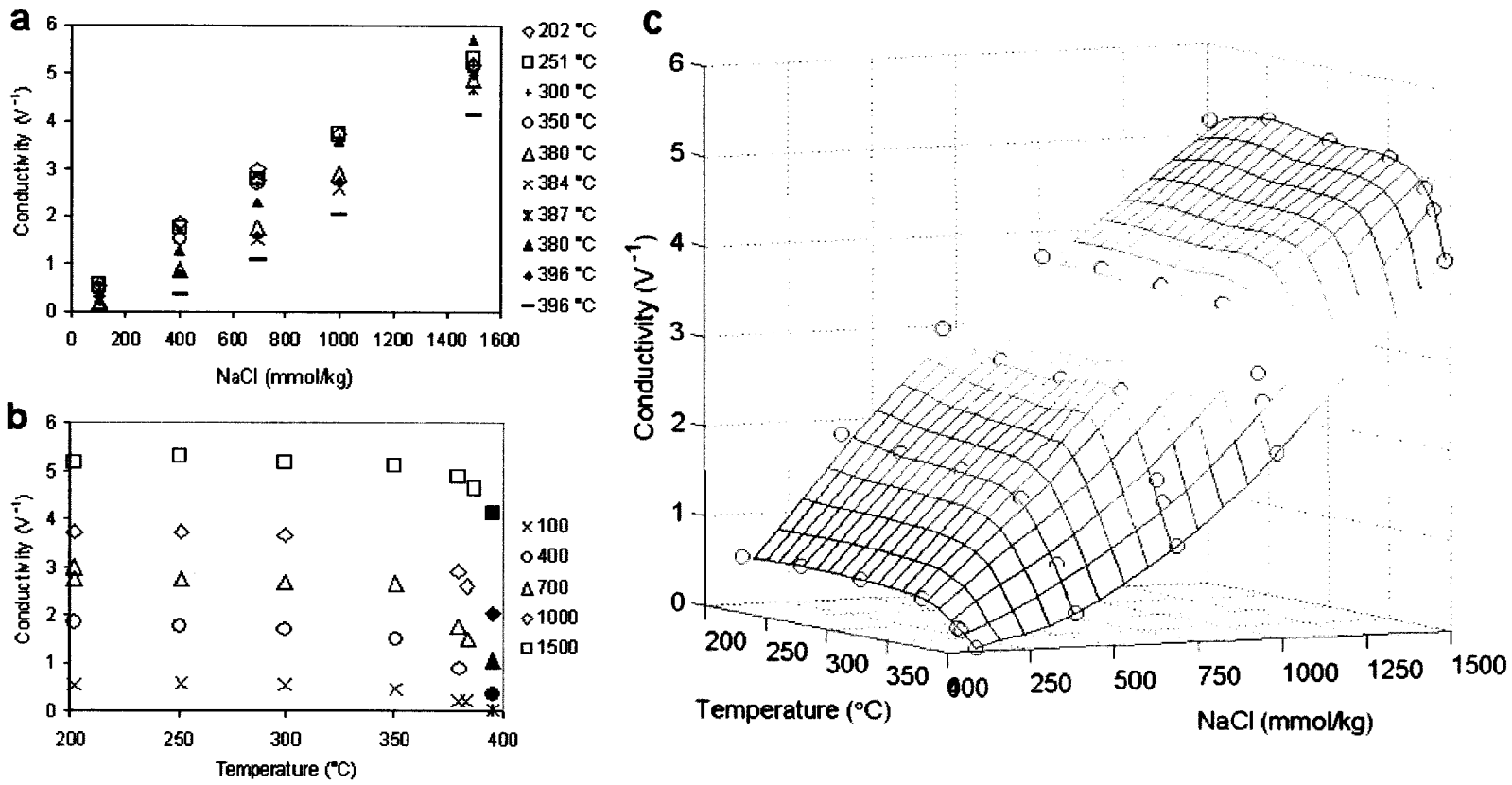

Figure 31. Calibration data for the 2004 version of the sensor using the experimental setup described in Larson et al. (2007). Data plotted (a) as isotherms of conductivity vs NaCl concentration (b) as isopleths of conductivity vs temperature and (c) as a three dimensional surface. All data were collected at 250 bars with the exception of the 395°C isotherm which was extrapolated from data at 395°C and 300 bars by applying the observed pressure effect on each solution at 380°C.

Measurements were then taken at 396°C and 300 bars and the observed pressure effect on conductivity at 380°C was applied to each solution at 396°C to extrapolate bulk fluid conductivity values in the two-phase region at 396°C and 250 bars (Figure 31b).

Between 200 and 350°C, conductivity depends linearly on NaCl and we see almost no temperature dependence (Figure 31a). At higher temperatures, we observe a non-linear dependence of conductivity on NaCl and conductivity begins to decrease with temperature (Figure 31b). Data shown in Figure 31b form the basis of a data grid used to create a calibration surface (Figure 31c) via spline interpolation (de Boor, 1978). Under similar conditions, Larson et al. (2007) modeled a relationship between conductivity and temperature with a maximum at 270°C for solutions ranging from 54 to 634 mmol/kg. Data from Larson et al. (2007) included measurements at 100°C where conductivity for a given solution is much lower than at 200°C (the minimum of the current study). Fitting the curve to these lower values, introduced an artificially inflated maximum. Results from the present study with more data suggest the peak has a broader flatter shape.

It is important to note that both studies observe invariance between conductivity at 200 and 300°C, but due to the shifted range and increased resolution in temperature from one study to the next, the shape of the modeled surface differs. Nevertheless, both surfaces depict decreasing conductivity with increasing temperature beyond 350°C which is the temperature range relevant to our measurements.

3.2.3 Uncertainty in temperature and conductivity

The surface from the present study (Figure 31c) is used to infer NaCl concentrations from conductivity-temperature data pairs collected at Bio 9'. It should be noted that while conductivity measurements at the experimental site reflect a 10 cycle average of the AC voltage measurement which reduces noise from variation in the drive voltage, (Larson et al., 2007) no such averaging scheme was applied to temperature, resulting in more high frequency variability in temperature than may truly exist.

The combination of temperature variability and conductivity dependence on temperature results in the conversion of a fairly flat conductivity baseline into a more uneven chloride profile (Figure 32). For a typical section of data (Figure 32), this effect translates to a chloride range that is approximately 2% greater than the associated conductivity range. In our laboratory setup, individual temperature measurements are based on an average of 10 thermocouple voltages. Isotherm temperatures in Figure 31a reflect the average of individual measurements for the entire time temperature was held constant, usually about 1.5 hours.

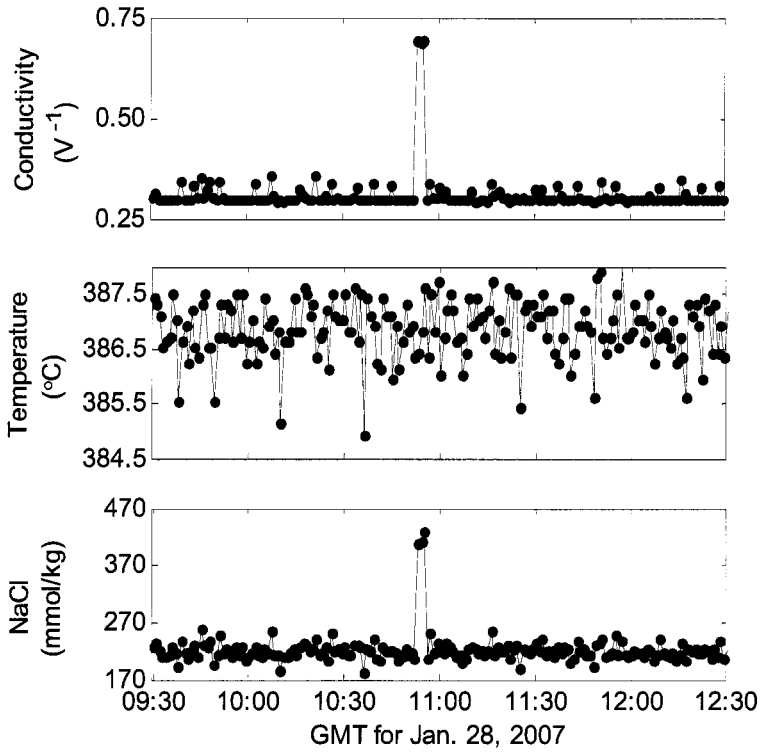

Figure 32. Conductivity and temperature data are used in conjunction with the calibration surface to convert conductivity values into NaCl concentrations. Data shown here are from a section of the full data record collected at Bio 9'.

3.2.4 Two-phase measurements

Although we can not measure properties of each phase of a two phase fluid independently in our laboratory calibration setup, we did observe the results of crossing

the two-phase boundary in our experimental setup by increasing the temperature of a 1000 mmol/kg solution to 396°C at 250 bars (Figure 33a).

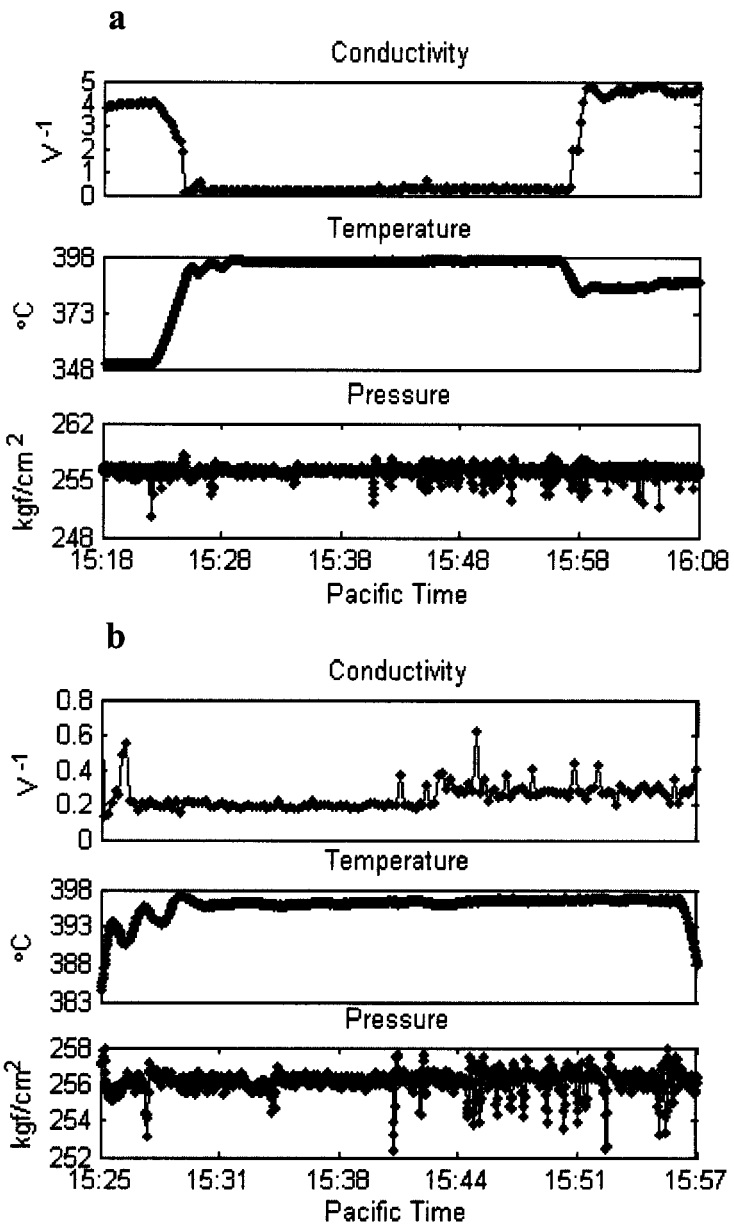

Figure 33. (a) Conductivity response under simulated hydrothermal conditions as a NaCl solution crosses the two-phase boundary. (b) a blown up section of data shown in part (a).

At ~386°C and 15:25 Pacific time, conductivity decreases rapidly in keeping with the onset of phase separation and subsequent expulsion of mostly vapor phase. We also observe occasional spikes in conductivity as the brine phase periodically moves through the flow cell and across the sensor face, generating a somewhat 'jumpy' signal with a fairly constant baseline value (Figure 33b).

4. Field Data

In the 9-14 months prior to the 2006 eruption, we deployed an instrument to measure temperature and conductivity, as a proxy for chloride, of Bio 9' vent effluent over an interval of time lasting approximately 5 months (Figure 34). Our data is complimented by measurements of ridge seismicity (Figure 35) recorded with nearby ocean bottom seismometers (Tolstoy et al., 2006).

The most significant periods of sustained variability in chloride and temperature occur between the beginning of the deployment in November of 2004 and the end of December 2004. During this interval, the number of seismic events varied between 200 and 600 events/day with the exception of two days when the number of seismic swarms was in excess of 800 events (Figure 35). Both days were accompanied by noteworthy changes in chloride and temperature. One swarm occurs on November 27, 8 days after the instrument deployment and one occurs approximately 3 weeks later on December 17.

We will structure our discussion around two key sections of the data: 1) 2 days before and 8 days following the intense seismic swarm on Nov. 27 and 2) 1 day before and 2 weeks following another intense seismic swarm on Dec. 17. We use chloride and temperature measurements from these two periods of intense variability in fluid composition to infer PT conditions of hydrothermal circulation prior to venting.

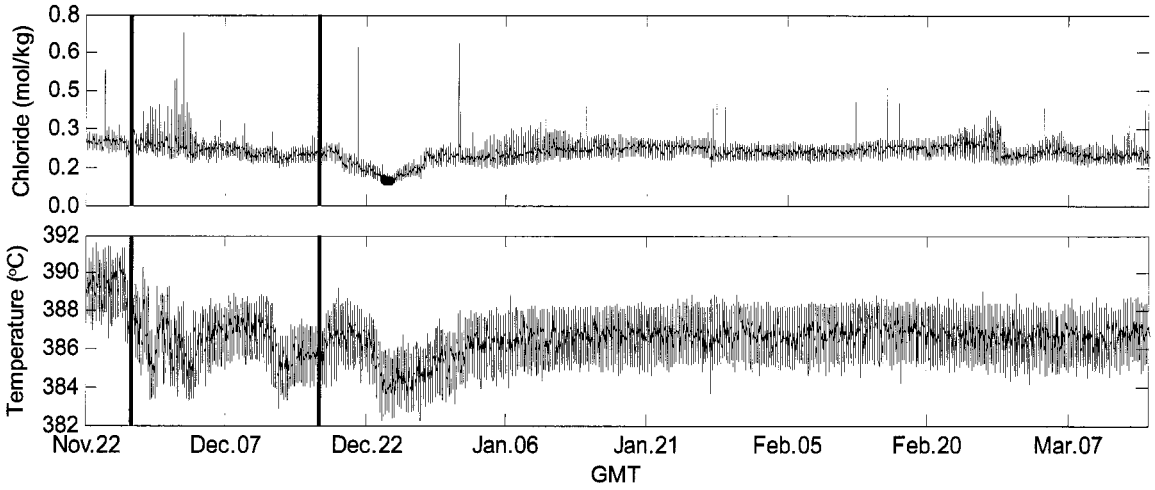

Figure 34. Full data record of NaCl and temperature for instrument deployment at Bio 9' from Nov. 22, 2004 to Mar. 15, 2005. The red lines indicate midnight on each of two days with intense seismicity: Nov. 27 and Dec. 17, 2004 (see Figure 35). NaCl concentrations are calculated as described in Larson et al. (2007) using conductivity and temperature measurements in conjunction with the surface shown in Figure 31c.

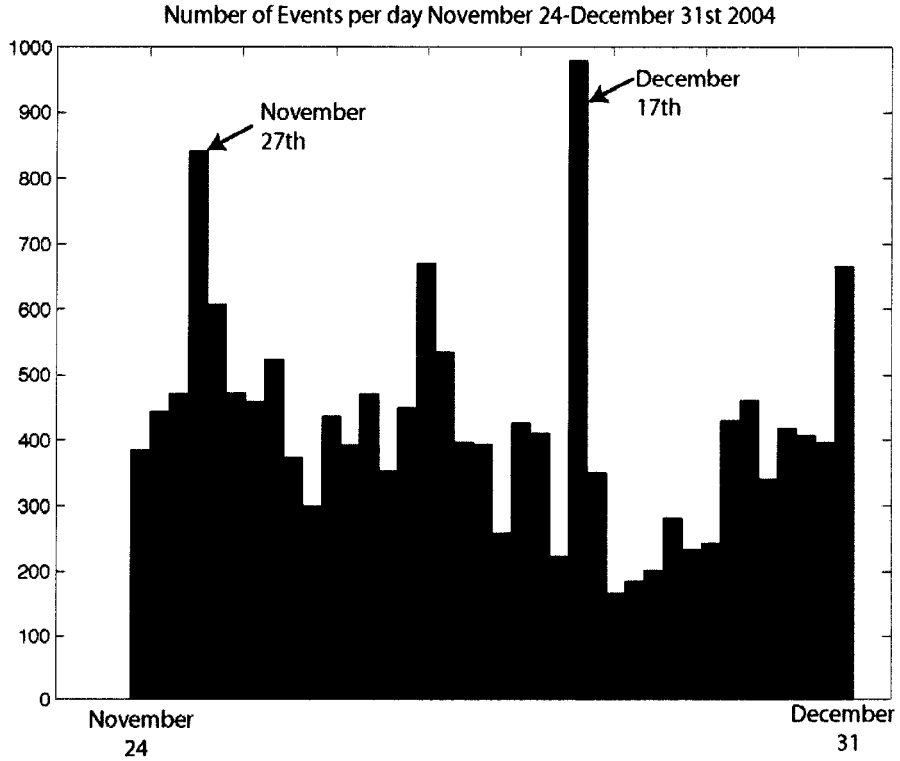

Figure 35. Number of seismic events per day as recorded by nearby ocean bottom seismometers for the portion of the EPR ridge axis at which Bio 9' is located. Modified from Tolstoy et al (2006).

4.1. Variability in fluid composition surrounding the Nov. 27 seismic swarm

On November 27, the number of seismic events peaked at over 850 (Figure 35) and on the same day, we observe the beginning of a significant hydrothermal response lasting for over a week (Figure 36). Temperature in Figure 36 has been filtered using a running average with a 10 min. window size.

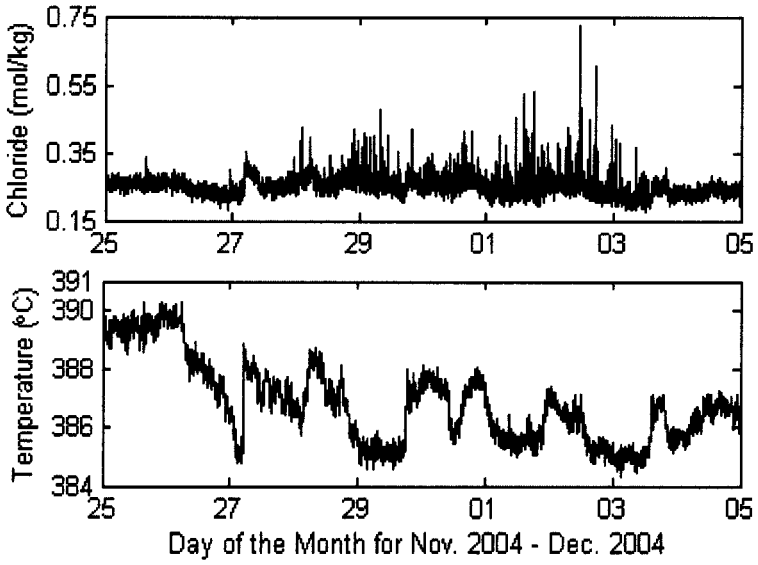

Figure 36. Expanded view of data in Figure 34 showing chloride and temperature variability from 2 days before the Nov. 27 seismic swarm to 8 days after the event. Temperature has been filtered using a running average with a 10 min window size.

4.1.1 Temperature variability

On Nov. 26, the day before the seismic swarm, temperature decreases slowly from 390°C to 385°C leading up to a 4°C jump to 389°C occurring over 19 minutes (Figure 36). We see this general pattern of temperature decay followed by a temperature increase repeated several times from Nov. 27 to Dec. 3 with temperature fluctuating between 385 and 388°C amid an overall decrease in temperature over 7days to ~387°C. The rates of temperature increase and decay vary over this interval but temperature decreases typically occur more slowly than subsequent temperature increases. Similar

temperature variability in high temperature focused flow from the Bio 9 complex and neighboring vents was also observed in Nov. 1997 and was attributed to a perturbation of the permeability structure of the local hydrothermal plumbing (Scheirer et al., 2006).

4.1.2 Chloride variability

The 4°C jump in temperature occurring part way through Nov. 27 is accompanied by an increase in chloride from 237 to 315 mmol/kg occurring over 1 hour (Figure 36). Chloride then decays to the baseline value over the next 6.5 hours. We see a similar coincident increase in chloride and temperature on Dec. 3 just before chloride stabilizes. Both temperature and chloride changes in this instance are much smaller than on Nov. 27. In the Dec. 3 instance, temperature increases from 385°C to 387°C over ~1 hour. The increase in chloride from 220 to 247 mmol/kg also takes about 1 hour but does not start until ~40 minutes after the beginning of the temperature increase.

Over the 6 days between these coincident chloride and temperature increases, we observe frequent, recurring and short lived positive excursions in chloride coinciding with large swings in temperature. The magnitude of these chloride spikes ranges from 400 to 720 mmol/kg, spike duration ranges from 1 min to 7 min and the interval between spikes ranges from a few minutes to several hours. Meanwhile, baseline chloride over this interval changes very little such that chloride always returns to a relatively constant value (between 240-260 mmol/kg) after an excursion. We also note a slow overall decrease in baseline chloride from 280 mmol/kg at the beginning of the deployment to 240 mmol/kg 1 week after the Nov. 27 seismic swarm

Although chloride excursions during the 8 days following the Nov. 27 swarm are short lived, peak shape does exhibit some variability. Peaks vary from single data points set above the baseline chloride (Figure 37a) to peaks with a rapid onset and gradual decay (Figure 37b) to more well defined peaks (Figure 37c). The most notable example of this latter type occurs on Dec. 2 at 11:30 over a period of 7 mins, exhibits a gradual onset, reaches a maximum of 721 mmol/kg then gradually decays (Figure 37).

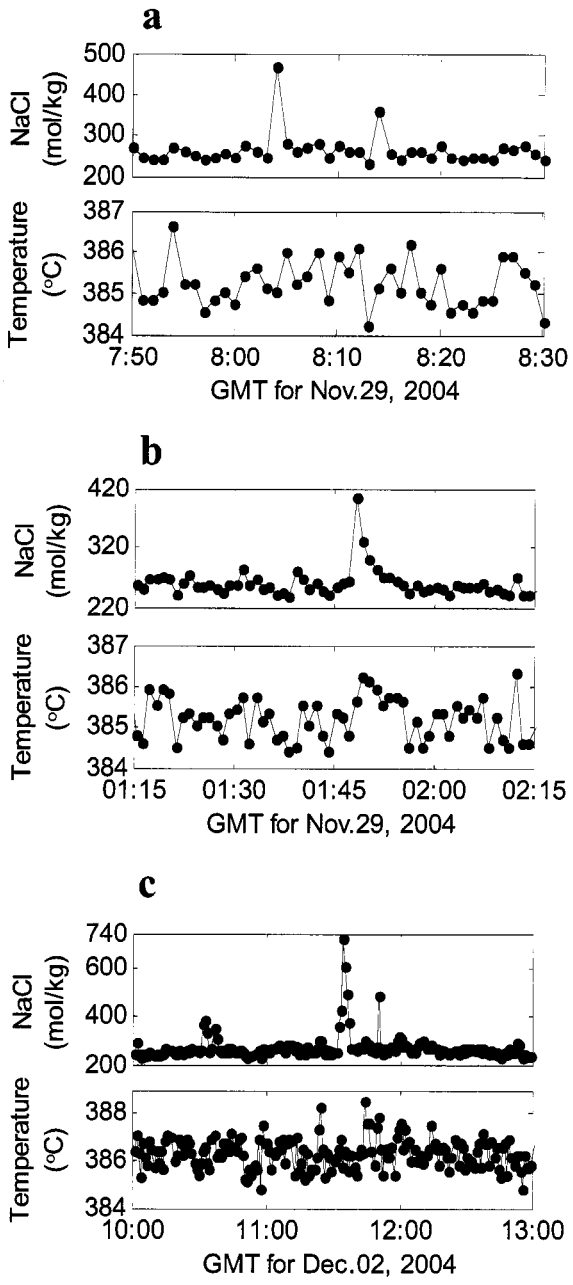

Figure 37. Expanded sections of data in Figure 36 depicting peak shapes of chloride spikes including (a) chloride spike lasting only a single data point, (b) chloride spike with a rapid onset and gradual decay and (c) chloride spike with both a gradual onset and gradual decay.

This chloride value is higher than any other measured chloride in fluids from both the Bio 9 complex and the nearby P vent over the last 15 years (Von Damm et al., 2004; Von Damm, pers comms).

4.1.3 Lack of coherence between temperature and chloride signals

Beyond the initiation and conclusion of the hydrothermal response to the increased seismicity on Nov. 27, chloride and temperature at Bio 9' show little correlation with the exception that degree of variability for each parameter is most pronounced over the 10 day period depicted in Figure 36. This coincident heightened variability and the duration of the chloride spike on Dec. 2 bolster the case that although conductivity excursions are generally short-lived, they represent actual changes in fluid chemistry which, however, lack coherence with respect to changes in temperature.

4.2. Variability in fluid composition surrounding the Dec. 17 seismic swarm

On December 17, the number of seismic events peaked at over 975 (Figure 35) and once again, we observe a significant hydrothermal response (Figure 38) the temporal nature of which, however, is somewhat different than the response to the Nov. 27 swarm. As with the Nov. 27 swarm, the hydrothermal response to the Dec. 17 swarm occurs on the same day as the intense seismic activity and is preceded by a decrease in fluid temperature. However, the temperature decrease on Dec. 17 is sustained for a longer period of time prior to the swarm than on Nov. 27.

4.2.1 Temperature variability

On Dec. 12, 5 days prior to the seismic swarm, we see a slow but jagged decrease in temperature from 387 to 385°C (Figure 38). Temperature rebounds by 0.8 ° C on Dec. 13 over about 20 hours, then remains steady for ~3 days before a 1°C increase over a five hour period on Dec. 17 coinciding with intense seismic activity (Figure 35).

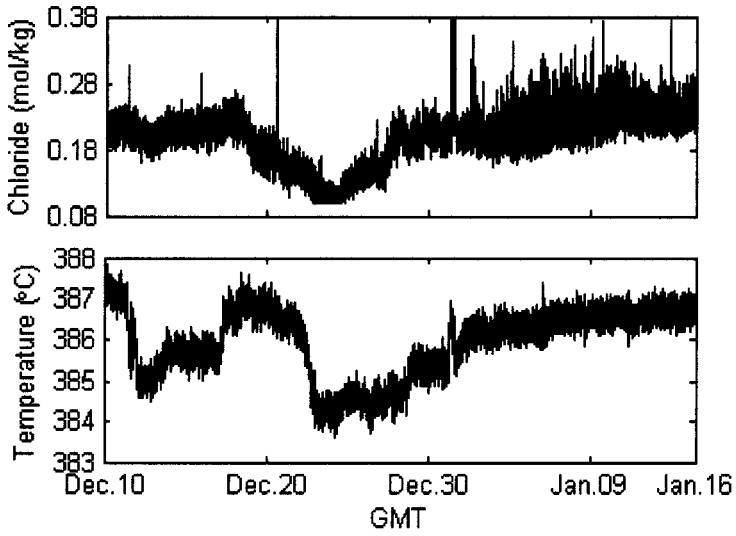

Figure 38. Expanded view of data in Figure 34 showing chloride and temperature variability from 7 days before the Dec. 17 seismic swarm to 29 days after the event. Temperature has been filtered using a running average with a 10 min window size.

Temperature remains elevated around 386.5°C for 4.5 days before decreasing to 384.3°C over the next 1.5 days. Temperature rebounds once more over the next 2 weeks, leveling of at ~386.5°C on Jan. 7 for the remainder of the record.

4.2.2 Chloride variability

Prior to the Dec. 17 swarm, mean chloride exhibits a slow and steady decrease from 240 mmol/kg a week after the Nov. 27 swarm to 220 mmol/kg just before a rapid decrease in chloride coinciding with the intense seismic activity observed on Dec. 17 (Figure 38). This downward trend is part of an overall decrease in baseline chloride from the start of the deployment to just before the Dec. 17 seismic swarm. On Dec. 17, mean chloride decreases from 228 to 110 mmol/kg over the course of 6.58 days, reaching a minimum on Dec. 23 and coinciding with the minimum temperature for the record. The minimum value of the chloride dip, 110 mmol/kg, represents the lowest observed chloride for fluid from the Bio 9 complex with the exception of fluid samples taken in 1992 which reached as low as 50 mmol/kg (Von Damm, 2004). After bottoming out at

110 mmol/kg on Dec. 23, chloride rebounds over the next 6 days reaching a mean value of 212 mmol/kg.

Two days later on Dec. 31, we observe a 1°C increase in temperature lasting ~8 hours and coinciding with a slight bump in chloride also lasting 8 hours. This coincident increase in chloride and temperature is similar to features at the start and end of the hydrothermal response to the Nov. 27 seismic swarm with one notable exception. On Dec. 31, we see repeated and short lived spikes in chloride ranging close to 700 mmol/kg superimposed on the more slowly varying chloride signal (Figure 39). After each excursion, chloride returns to the local baseline value.

Throughout the 2 weeks following the Dec. 17 seismic swarm we see virtually no interruptions of the chloride baseline with the exception of 1 isolated spike reaching 600 mmol/kg but lasting for only a single data point. On Jan. 1, we observe the reappearance of recurrent chloride spikes for the next 10 days, but none of these spikes exceeds 400 mmol/kg or lasts longer than 1 min.

4.2.3 Intense seismicity results in rapid and long term temperature changes

In the case of both the Nov. 27 and Dec 17. seismic swarms, we observe an immediate hydrothermal response which is significantly shorter than the delay in the hydrothermal response to a seismic event recorded in the study area on March 22, 1995 (Fornari et al., 1998, Sohn, 1998). In this latter instance, a perturbation to Bio 9 fluid temperature was not recorded until 4 days after the March 22 seismic event

Temperature changes accompanying intense seismicity from Nov. to Dec. 2004 in the present study persisted for at least another 3 months at 386.5°C, 3.5°C lower than before the seismicity. In comparison, the 8°C temperature increase associated with the seismicity in 1995 decayed slowly over a 3.5 month period, eventually returning to a pre-event level of 366°C (Fornari et al., 1998).

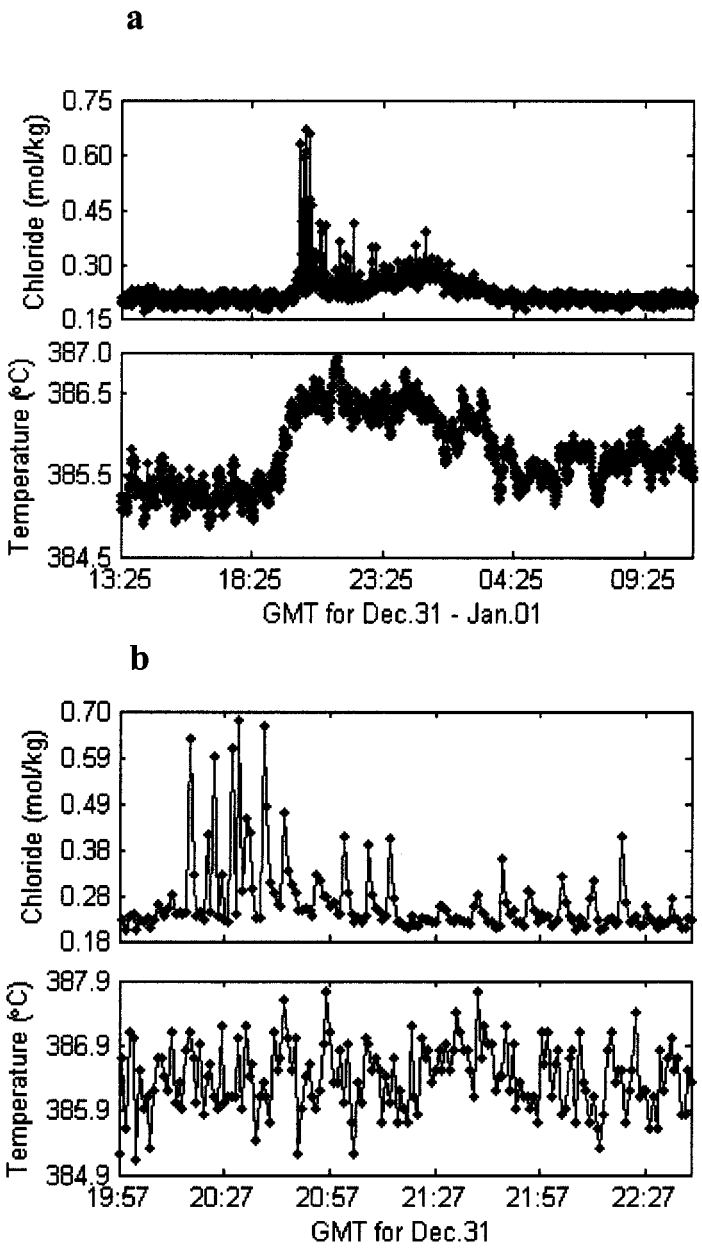

Figure 39. (a) Expanded section of data in Figure 38 depicting a coincident increase in chloride and temperature. Superimposed on the broad chloride bump are recurring chloride spikes. Temperature has been filtered using a running average with a 10 min window size. (b) Expansion of data in part (a) depicting chloride spikes in greater detail. Peak shape is similar to spikes in Figure 37a, b.

5. Discussion

The hydrothermal system at 9°50'N is located within a magmatically robust portion of the EPR wherein both the chemistry of hydrothermal fluids (Foustoukos and Seyfried, 2007; Von Damm and Lilley, 2004; Von Damm et al., 2004) and the seismic structure of the ridge (Sohn et al., 2004; Detrick et al., 1987) have been intensively studied. It is well known that phase separation plays in important part in the modification of fluid chemistry in this area, however, the PT conditions of phase separation are less clear. Inferences of hydrothermal root zone conditions from fluid chemistry measurements made in 2002 range between shallow subcritical PT conditions of 275 bars and 398°C (Von Damm, 2004), to deeper supercritical conditions of 320 bars and 420°C (Foustoukos and Seyfried, 2007). Phase separation during upflow may obscure the true PT conditions of the root zone so the seafloor chloride signature may actually represent the point of last phase separation.

A seismic study of the ridge estimates depth to an axial magma lens of 1.4 km below the seafloor (Detrick et al., 1987) which is consistent with supercritical PT conditions hypothesized by Foustoukos and Seyfried (2007). Observation of a cracking event in 1995 and subsequent modeling of the event (Sohn et al., 1998) also suggest hydrothermal circulation at a depth of at least 1.1 km. However, eruptions at 9°50' N in 1991 and 2006 provide clear evidence that magma migration plays an important role in determining the depth of hydrothermal penetration such that root zone conditions may be quite variable.

5.1. Inferring subsurface pressure and temperature (PT) conditions from seafloor measurements of chloride and temperature

It is well established that phase separation is the dominant influence on chloride concentration in high temperature hydrothermal fluid (Butterfield et al., 1994; Butterfield

et al., 1990, Von Damm, 1995) and that PT conditions of phase separation determine the composition of the two phases generated from a given precursor fluid (Bischoff and Pitzer, 1989). Thus chloride concentration in hydrothermal fluid can be used to infer the PT conditions at which that fluid was generated (Seyfried et al., 2003; Von Damm, 2004; Von Damm, 1995). However, given the likelihood that phase separation is not confined to a single portion of the crust (Lewis and Lowell, 2003; Seyfried et al., 2003; Von Damm et al., 2003) and that segregation of phases and conductive cooling can further obfuscate the history of seawater entering the hydrothermal cell, care must be taken when inferring subsurface PT conditions from seafloor measurements.

5.1.1 Seafloor phase separation

One possibility is that phase separation is occurring at the seafloor and obscuring the subsurface signature. Chloride spikes such as those observed from Nov.27 to Dec.3 are very similar to the pattern observed in our experimental setup under 2 phase PT conditions where we observed a varying mixture of vapor and liquid phases (Figure 33). Chloride measured in fluid samples taken from Bio 9' around the time of deployment had an average end-member chloride concentration of 260 mmol/kg and ranged in temperature from 384-389°C. At a seafloor pressure of 250 bars, seawater intersects its phase boundary at 388.7°C (Figure 40a) producing small amounts of a 58 mmol/kg vapor coexisting with a liquid phase with seawater chloride (Figure 40b). If the chloride baseline in the present study is assumed to be a constant mixture of vapor and liquid phases generated at the vent orifice, then chloride spikes would reflect increases in the fraction of the liquid phase as they do in our bench-top simulation (Figure 33). If this were the case, however, we would also expect the 2-phase signature to subside once seawater crossed into the 1-phase region. Temperature for most of the 6 day interval following the Nov. 27 seismic swarm is well below the phase boundary for seawater, yet we continue to see chloride spikes throughout this interval (Figure 40a).

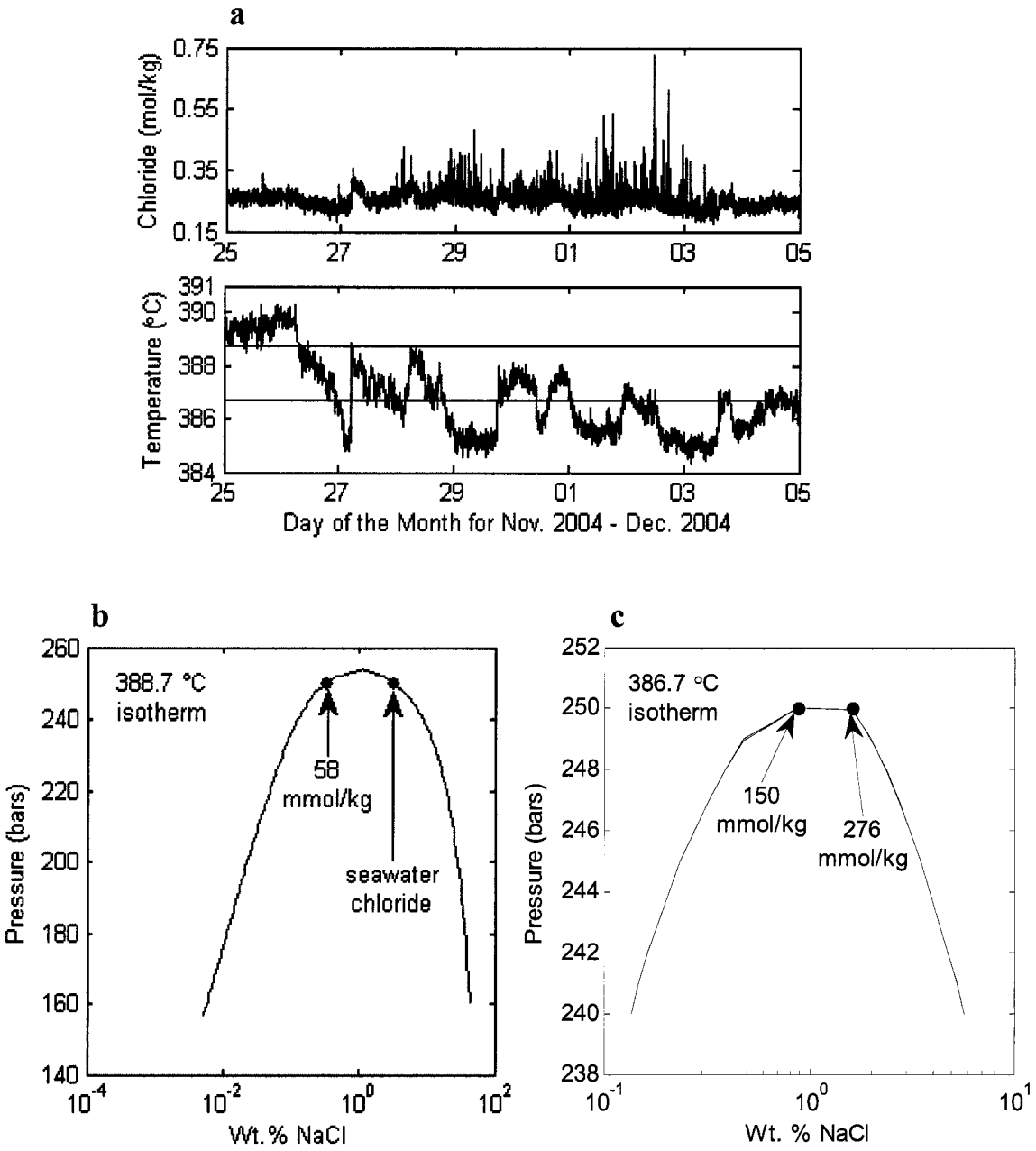

Figure 40. (a) Data from Figure 36 showing fluid temperature relative to temperature of the 2-phase boundary for sweater (red lined) and 260 mmol/kg (blue line) at a seafloor pressure of 250 bars. (b) Phase separation at 250 bars and the temperature of intersection on the 2-phase boundary, 388.7°C. (c) Phase separation of 260 mmol/kg NaCl solution at 250 bars and the temperature of intersection on the 2-phase boundary, 386.7°C

The precursor fluid undergoing phase separation need not be seawater. A 260 mmol/kg chloride solution at 250 bars phase separates at 386.7°C (Berndt et al., 2001), generating a 150 mmol/kg vapor with a mass fraction of 0.12 coexisting with a 276 mmol/kg liquid phase with a mass fraction of 0.88 (Figure 40c). Temperature swings following the Nov. 27 swarm and ranging up to 4°C in magnitude about a mean temperature of 385.4°C result in repeated shifting between 1 and 2 phase PT conditions for a 260 mmol/kg pre-cursor fluid (Figure 40a). If chloride spikes are assumed to be the result of seafloor phase separation under these conditions, observed chloride would reflect a mixture of vapor and liquid phases with spikes representing increases in the mixing fraction of liquid. However, we would expect the phenomenon to cease once temperature dipped below the phase boundary. Once again, the data does not bear this out. It is also worth noting that we do *not* observe chloride spikes for large portions of the record where temperature *is* sufficiently high to permit phase separation of a 260 mmol/kg fluid at the seafloor (Figure 34).

The implication of these observations is that even if seawater or a 260 mmol/kg fluid intersects its phase boundary at the surface, we are observing conductivity of the bulk fluid. This theory contrasts with results from our laboratory setup where a jumpy baseline (Figure 33b) implies incomplete mixing. The discrepancy is likely due to differences in flow under simulated conditions vs. flow at the vent orifice. Given the foregoing discussion, the chloride signature likely reflects effects of subsurface rather than seafloor processes.

5.1.2 Phase segregation and distillation

At the intersection of its 2 phase boundary, seawater generates a chloride depleted vapor or chloride enriched brine depending on whether PT conditions are sub or supercritical respectively (Figure 27). If phase separation is followed by complete phase segregation – an open system – and no further phase separation occurs, then the phase coexisting with vapor or brine at the point of phase separation will have seawater chloride

concentration (Figure 41a). If phase segregation is followed by further phase separation of a non-seawater precursor – distillation (Figure 27) – or if the phases do not immediately segregate – a closed system (Figure 41b) – a wider range of chloride concentrations is possible (Figure 41b).

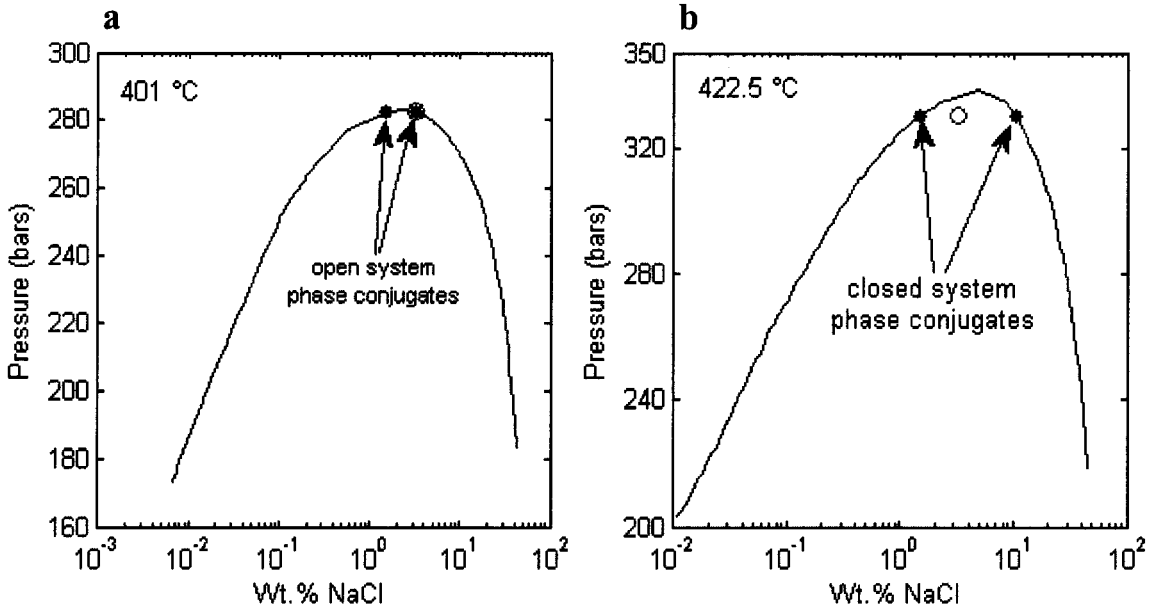

Figure 41. Composition of phase conjugates under (a) subcritical conditions in an open system at 282.5 bars 401°C and (b) supercritical conditions in closed system at 320 bars and 422.5°C. The open red circle in parts (a) and (b) denotes seawater chloride.

The concept of phase segregation has been postulated by theoretical studies (Fontaine and Wilcock, 2006; Seyfried et al., 2003; Schoofs and Hansen, 2000) and observed in the field (Von Damm et al., 2003; Von Damm et al., 1997; Butterfield et al., 1994). However the timing and extent of phase segregation and the distribution of phase separation are not well known. In this section, we assess the likelihood of each scenario.

5.1.3 Subsurface PT conditions inferred from baseline chloride

For the majority of the record, chloride falls within a narrow range from ~210 to 280 mmol/kg. Under subcritical PT conditions in an open system, our data is consistent with a scenario in which seawater phase separates at 282.5 bars and 401°C, generating a

260 mmol/kg NaCl solution (Bischoff and Pitzer, 1989; Von Damm, 2004). Baseline chloride in our data would represent the more buoyant vapor phase after segregation from a liquid phase with close to seawater chloride (Figure 41a). However, the volume fraction of the vapor phase would be unrealistically small and the seawater 'brine' would either need to be stored subsurface in large quantities or vented somewhere else altogether.

Under supercritical PT conditions in a closed system, our data is consistent with a scenario in which seawater phase separates at 330 bars and 421.5°C generating a 257 mmol/kg vapor (Bischoff and Pitzer, 1989). Baseline chloride in our data would represent the vapor phase, which could be produced in sufficient proportions to explain the continuous venting of a chloride depleted fluid (Figure 41b). Furthermore, this scenario is supported by silica geobarometry studies (Foustoukos and Seyfried, 2007). However, for this scenario to work, it must be assumed that the two phases remain homogenized or that each phase is independently undergoing phase separation (distillation).

The brine condensate from closed-system phase separation would be 1785 mmol/kg, which is 2x the maximum observed chloride in vent fluids anywhere along the East Pacific Rise (Von Damm et al., 1997). If it is assumed that distillation is occurring, then the range of possible PT conditions expands dramatically. In reality, hydrothermal effluent may reflect some complex combination of all three processes: phase separation under partially closed conditions and interspersed with distillation. Our goal is to use the in-situ chloride data to help place constraints on the complex evolution of subsurface PT conditions.

5.2. Hydrothermal PT conditions inferred from chloride and temperature response to Nov. 27 seismic swarm

The hydrothermal response to the seismic swarm on Nov. 27 (Figure 36) initiates with a 4°C temperature jump over 19 minutes and a coincident 78 mmol/kg increase in chloride over 1 hour. Temperature exhibits intense variability over the next 8 days eventually leveling off 5°C lower than before the swarm. The temperature signature is

consistent with repeated cracking events driven by hydrothermal cooling and followed by heat pulses as fresh hot rock is exposed (Lister, 1974). The brief temperature spikes are superimposed on an overall temperature decline reflecting the continued hydrothermal mining of heat from the newly exposed rock. Although thermal cracking resulting from melt migration has been postulated as a source of axial seismicity (Van Ark et al., 2007), we would expect such a process to be accompanied by a larger sustained heat pulse as well as dramatic and sustained dips in chloride (Lilley et al, 2003; Fornari et al., 1998; Von Damm et al., 1995) rather than rapid temperature swings, an overall temperature decrease and a transient increase in chloride. Thus we postulate that the Nov. 27 swarm reflects a tectonic rather than magmatic event.

5.2.1 Chloride variability reflects removal of subsurface brines

Unlike the chloride spikes in the week following the Nov. 27 swarm, the initial jump in chloride and the subsequent decay (Figure 36) persists for a relatively long time, taking place over 7.5 hours. Nevertheless, the duration of the variation is short compared to sustained brine venting at other sites on the EPR (Von Damm, 1995). The magnitude of the chloride increase is small enough that it could be the result of changes in water/rock reactions at the root zone (Seewald and Seyfried, 1990), however, the transient nature of the change suggests it is the result of either a shift in PT conditions of phase separation owing to the cracking related pressure and temperature changes or the influence of subsurface brines released by cracking events.

If the chloride signature were the result of an increase in PT conditions of phase separation in an open system driven by crack propagation into hot rock (Lister, 1974), we expect an increase in vapor phase salinity (Figure 42). A shift in PT conditions from 400°C and 280 bars to 403°C and 288 bars would produce an increase in vapor phase salinity from 237 mmol/kg to 315 mmol/kg which is consistent with the observed chloride change. However, the predicted temperature change at depth is smaller than what we observe at the vent orifice and, if anything, we expect a temperature perturbation

at depth to decay during ascent (Seyfried et al., 2003; Wilcock, 1998) not increase. Furthermore, chloride changes at depth are conserved during ascent in the absence of phase separation while temperature changes at depth are buffered by the host rock during ascent. Thus, we would expect the temperature increase to lag the chloride increase not coincide with it (Wilcock, 2004).

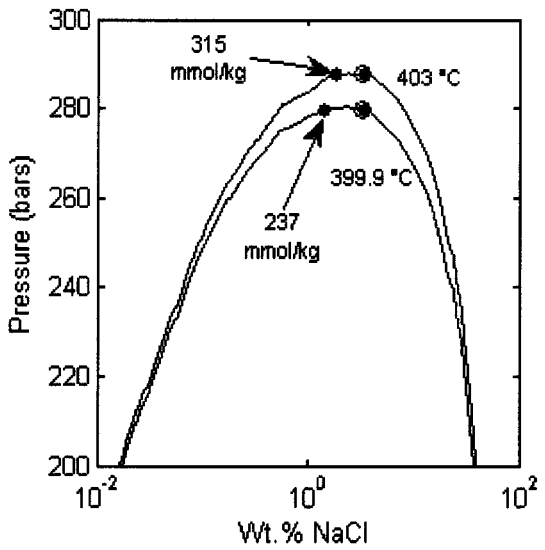

Figure 42. Shift in phase compositions expected for an increase in PT conditions of phase separation originating from downward crack propagation into hot rock.

Another scenario consistent with the chloride increase is the release of subsurface brines from rock exposed by a cracking event (Figure 43). Storage of subsurface brines is a likely fate for the denser of two phases produced by phase separation (Fontaine and Wilcock, 2006; Fontaine et al., 2005; Michael and Cornell, 1998; Larson et al., 2007; Lowell and Germanovich, 1997) and given differences in density between phases (Seyfried et al., 2003; Berndt et al., 2001; Anderko and Pitzer, 1993), it is typically assumed that a ubiquitous vapor phase will ascend preferentially over a denser brine phase. Under these assumptions, vent effluent during the chloride excursion on Nov. 27 may reflect mixing of small amounts of brine with a predominant vapor phase while PT conditions of phase separation remained undisturbed. This scenario is consistent with the

observation that chloride never exceeds seawater concentration during the excursion and that baseline chloride remains relatively constant. The eventual decay back to baseline chloride after 6.5 hours suggests the brine reservoir tapped by cracking in the rock is finite.

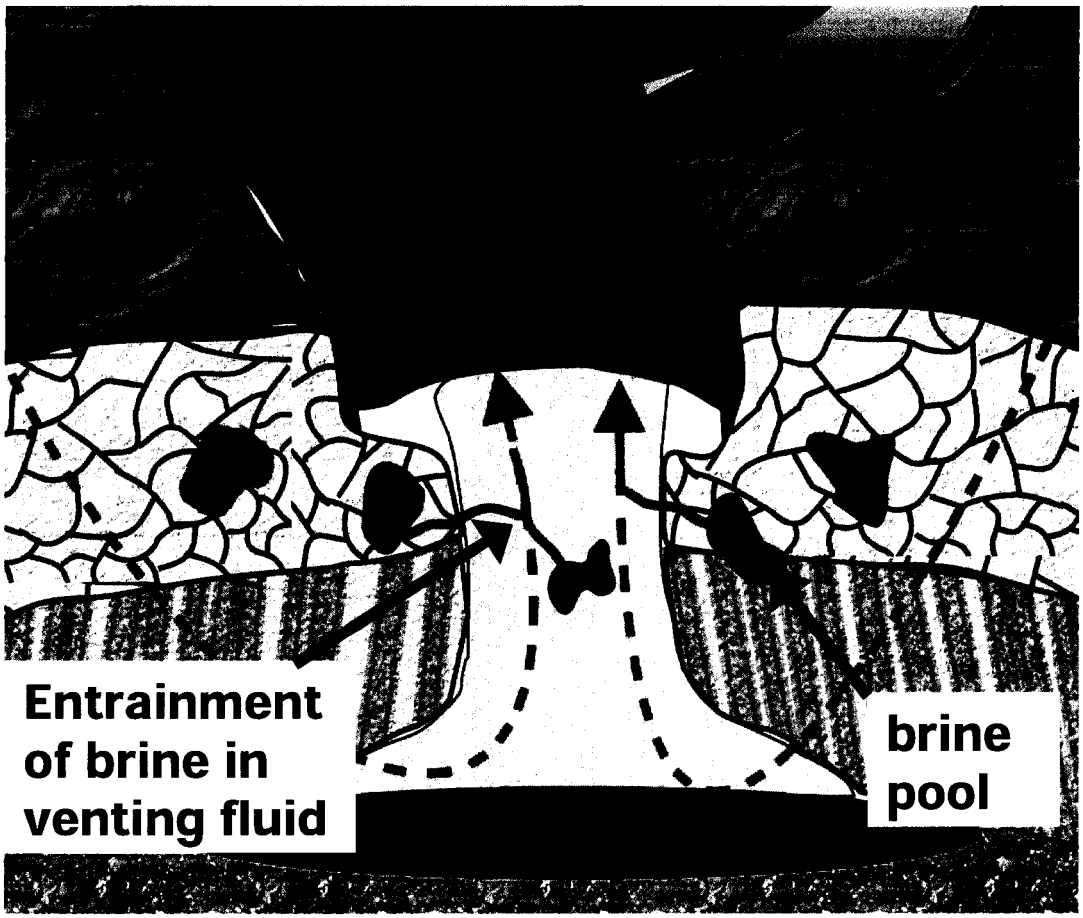

Figure 43. Schematic of subsurface brine reservoirs tapped by cracking in the rock. Blue reservoirs represent brine pools. Graded arrows represent new cracks tapping subsurface brine pools.

Brine mining by chloride depleted fluid has also been observed at the Main Endeavour Field (MEF) on the Juan de Fuca Ridge 12-15 months after a magmatic event (Larson et al., Subm), though the mechanism of brine mining differs between the MEF and EPR hydrothermal systems. In the case of MEF, brine mining can only account for a

small fraction of the supposed subsurface reservoir (Larson et al., in prep). In order to calculate the impact of brine mining at Bio 9' on the EPR we must first determine the likely composition of brines underneath this vent.

5.2.2 PT conditions of brine formation

Chloride excursions in the wake of the Nov. 27 seismicity are generally greater in magnitude and shorter in duration than the 6.5 hour chloride excursion coinciding with the Nov. 27 seismicity (Figure 36). We observe a general increase in the maximum magnitude of the short-lived chloride spikes beginning on Nov. 27 and culminating on Dec. 2 in a spike lasting 7 mins and reaching 720 mmol/kg (Figure 37c). One scenario consistent with both the longer lived chloride excursion and the more transient spikes is that they are manifestations of the same brine mining process. The longer lived excursion could represent a slow controlled depletion of a brine deposit under confined mixing conditions while the brief spikes represent expulsion of less diluted brines from pore space violently opened up by cracking in the rock. The latter process represents a mechanism whereby hot brine phases, which are less buoyant than their conjugate vapors but still more buoyant than ambient seawater, may vent at the seafloor.

If we assume brines are stored at the depth of formation and that the conjugate phase for the stored brine has the same composition as the vapor phase currently venting, we can infer possible PT conditions of brine formation from phase relations (Berndt et al., 2001; Bischoff and Pitzer, 1989). We take the maximum observed chloride during this period, 720 mmol/kg, as the concentration of undiluted brine and we use a typical chloride baseline value, 252 mmol/kg, as the undiluted vapor phase. At 288 bars and 403.5°C, phase separation of seawater generates a 252 mmol/kg vapor phase with a density 0.38 g/cm^3 and a 732 mmol/kg brine phase with a density of 0.43 g/cm^3 (Figure 44 and Berndt et al., 2001). A kg of seawater phase separating at these conditions would produce 1.47 L of brine and 0.97 L of vapor. To make this calculation, we assumed no vertical brine migration and temporal invariability but there is evidence that these

assumptions may not always be valid (Fontaine and Wilcock, 2006; Goldfarb and Delaney, 1990; Lilley et al, 2003; Von Damm, 2004).

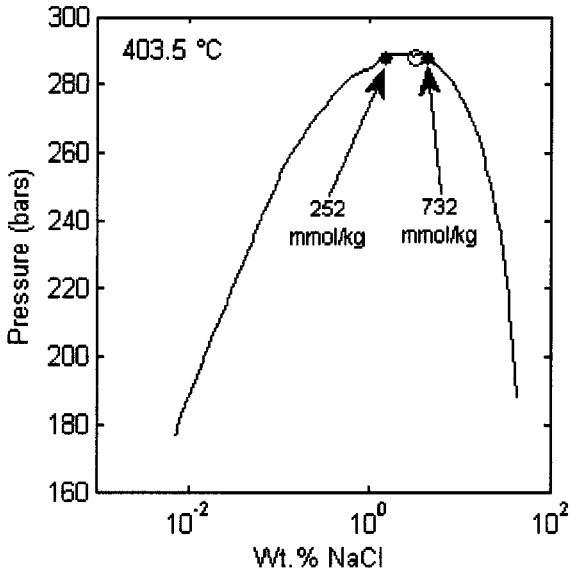

Figure 44. Inferred PT conditions of root zone based on chloride concentration of baseline and peak values between Nov. 25 and Dec. 5. The red open circle represents seawater chloride.

Our calculated PT conditions (Table 13) are within the range of conditions inferred by other investigators (Von Damm, 2004; Foustoukos and Seyfried, 2007) and are unique conditions under which phases with the specified compositions coexist (Berndt et al., 2001).

Table 13. Calculated root zone conditions for Bio 9' vent 9°50'N on the East Pacific Rise based on in situ measurements or fluid samples from 2004

Reference	Pressure (bars)	Temperature (°C)
present study	288	403.5
Von Damm (2004 and pers comms)	282.5	401
Foustoukos and Seyfried (2006)	320	422.5

It is important to note that these PT conditions imply phase separation slightly beyond the phase boundary (Figure 44) indicating a closed system for at least a portion of the

circulation pathway. The temperature difference between the depth of phase separation, 403.5°C, and the mean temperature at the seafloor, 386.7°C, is entirely accounted for by adiabatic cooling of a 1.5 Wt.% solution assuming a bulk fluid enthalpy of seawater at time of phase separation of 2075 J/g (Figure 45).

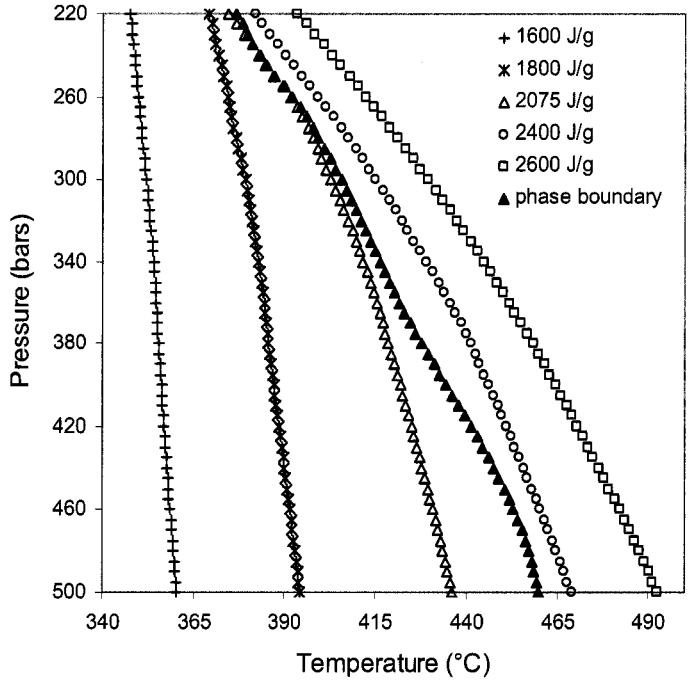

Figure 45. Phase boundary and isenthalps for a 252 mmol/kg NaCl solution. Assuming PT conditions of phase separation at 403.5°C and 288 bars, the seawater precursor has a bulk fluid enthalpy of 2075 J/g which translates to a seafloor temperature of 386.7°C for a 252 mmol/kg solution

Given the low density of both phases compared to ambient seawater and their temporal proximity, it's possible that chloride spikes represent intermittent venting of brines produced concurrently with the predominant vapor phase. However, coincidence of chloride spikes with intense seismicity and their general absence throughout the remainder of the record despite similar temperatures argues for the release of pre-existing brines. The duration of brine storage remains open to question. In our analysis we assume no vertical brine migration but both theoretical studies (Fontaine and Wilcock, 2006) and field observations (Von Damm et al., 1997) suggest that brines, in fact, do move upwards

within the crust over timescales on the order of years. Thus, coexistence of a brine phase and a vapor phase at a depth that is unique to that combination suggests the brine could be vented not long after its creation.

5.2.3 Brine flux calculations

The duration and magnitude of the chloride excursion on Nov. 27 suggest the subsurface brine deposit exposed by the seismic swarm is small and once it has been mined, chloride returns to a value similar to the pre-excursion value. Nevertheless, we can calculate the mass of brine contained in the reservoir. Using equation (8) and phase compositions as calculated in section 5.2.2., we can calculate vapor and brine mixing fractions.

$$(8) \quad x_v = \frac{s_f - s_l}{s_v - s_l}$$

where x is mixing fraction, s is Wt.% NaCl, and the indices v, l and f indicate vapor, liquid (brine) and vent effluent respectively. s_v and s_l from section 5.2.2. are 1.55 and 4.28 Wt.% respectively. The observed chloride concentration at the height of the excursion, 315 mmol/kg (1.84 Wt.%), represents s_f. Using these values, we calculate a vapor fraction, x_v, of 0.84 and a brine fraction, x_l, of 0.16. After the initial spike, chloride returns to a value similar to the pre-excursion value, over a period of 6.5 hours. If we assume a linear decrease in the fraction of brine over this interval, then the amount of 4.28 Wt.% brine removed in this fashion can be calculated with equation (9),

$$(9) \quad m_b = \frac{1}{2} \cdot x_l \cdot r \cdot \Delta t$$

where x_l is the maximum mixing fraction of brine, r is the mass flux of vent effluent, Δt is the duration of the excursion and m_b is the mass of brine removed. Assuming a mass flux similar to high temperature fluids further South on the EPR at 21 °N, r has a value of 150 kg/s (Converse et al., 1984). Under these conditions, 2.81×10^5 kg brine can be removed over the course of 6.5 hours. At the conditions of the mixing zone, 288 bars and 403.5°C, a 4.28 Wt.% brine has a density of 0.43 g/cm^3. Under these conditions the mass of the brine deposit equates to a volume of 6.53×10^5 L (653 m^3).

5.3. Hydrothermal PT conditions inferred from chloride and temperature response to Dec. 17 seismic swarm

The hydrothermal response to the seismic swarm on Dec. 17 is notably different than the response to the Nov. 27 swarm exhibiting a dramatic and sustained dip in the baseline chloride value coinciding with temperature swings up to 3°C in magnitude and interrupted by only a few brief positive chloride excursions (Figure 38). After a small initial increase, chloride begins a sustained downward trend over 6 days bottoming out at a mean value of 110 mmol/kg. For 4.5 days of this decrease, mean temperature is elevated by 1.5°C over mean temperature before the seismic swarm. However, even at its maximum value during the chloride dip, temperature is comparable to the observed range for the remainder of the record during which the chloride baseline is relatively stable. In the following section, we address the various processes that could explain the chloride and temperature signature.

5.3.1 Magmatic heat input – Heating at decreasing or constant pressure

Upwards migration of melt within the crust is consistent with the both the chloride decrease and temperature increase (Lilley et al., 2003; Wilcock, 2004) and has been postulated for the study area (Von Damm, 2004). The result of a dike injection would be a shift in PT conditions to higher temperatures at decreasing or stable pressures

(Delaney et al., 1998). We can calculate a variety of changes in PT conditions that reproduce the observed decrease in chloride following the Dec, 17 seismicity (Figure 27). However, a temperature perturbation arising from a magmatic heat pulse would likely be significantly greater in magnitude and last significantly longer than the observed local elevation in temperature of 1.5°C lasting only 4.5 days (Butterfield et al. 1997; Lilley et al., 2003; Von Damm et al., 1995; Wilcock, 2004). Moreover, the chloride dip in the wake of a magmatic event would likely be sustained for more than the observed 6 days (Lilley et al., 2003). Thus the observed chloride and temperature changes are inconsistent with the expected signature of a significant magmatic event. We can not, however, rule out the possibility of very small amounts of magma expelled through newly created cracks in the roof of a magma chamber at the base of the root zone. This scenario is consistent with both the chemical and seismic signatures.

5.3.2 Downward or lateral propagation of a hydrothermal cracking front – heating at increasing pressure or constant pressure

Another explanation consistent with the local elevation in temperature following the Dec. 17 seismicity is penetration of a cracking front down into hot rock resulting in both a heat pulse and an increase in the pressure of phase separation (Fornari et al., 1998 Lister, 1974; Wilcock, 2004). Phase separation in an open system as pressure increases from pressure postulated in the present study, 288 bars, to pressure predicted by Foustoukos and Seyfried (2006), 330 bars, generates an increase in chloride of the vapor phase which is opposite the observed trend (Figure 46a). If we assume closed system conditions for a portion of the circulation pathway and a shift in PT conditions from this study to PT conditions similar to Foustoukos and Seyfried (2006), we can reproduce a shift in chloride similar to the observed shift.

A PT shift from 288 bars and 403.5°C to 320 bars and 422.5°C yields a change in vapor phase chloride from 252 mmol/kg to 111 mmol/kg (Figure 46b).

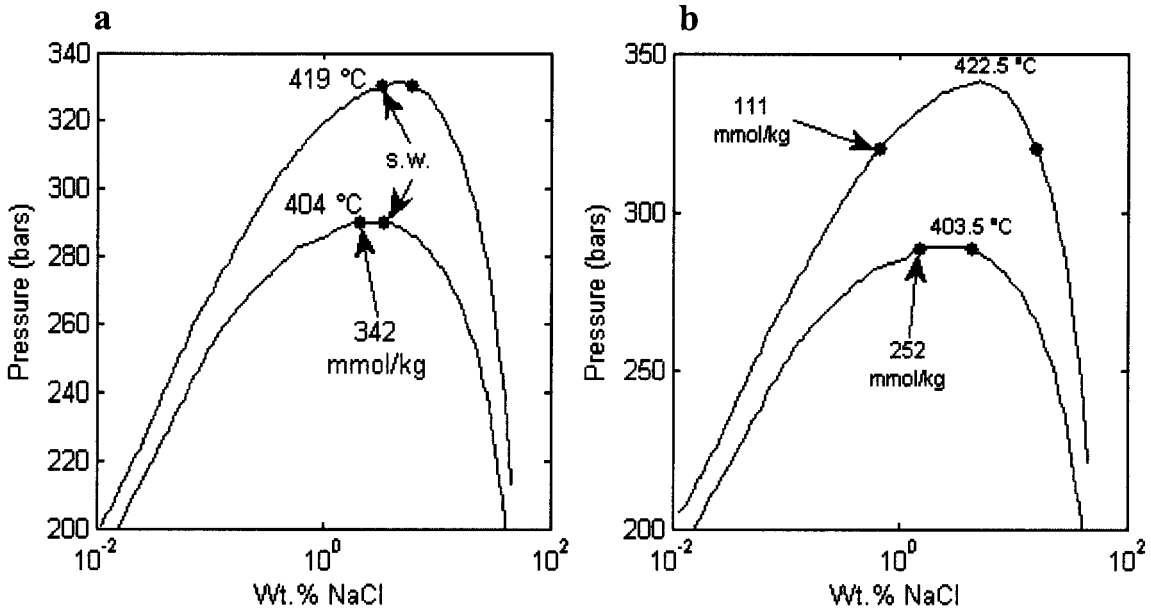

Figure 46. PT conditions predicted from propagation of a cracking front from pressure predicted in the present study to pressures similar to results of Foustoukos and Seyfried (2006) under (a) open system conditions and (b) closed system conditions.

This scenario would imply crack propagation over a distance of ~320 m or, more likely, an increase in pressure as fluid enters a tightly confined space opened by cracking. However, the expected brine phase composition of 2686 mmol/kg is almost 4 times larger than any chloride concentration observed during the course of the record. We can reproduce the observed chloride decrease with a smaller increase in pressure but the brine phase composition for an increase in pressure as small as 7 bars is 1689 mmol/kg, more than twice the maximum observed chloride.

We can perform a similar analysis for a lateral cracking front in which heat is injected into the system at constant pressure but here again, brine compositions cannot be reconciled with maximum observed chloride values. However, it is important to note that even the highest chloride concentrations at the seafloor may not represent undiluted brine concentrations at depth.

5.3.3 Change in upflow zone pressure gradient – effective reduction in pressure of phase separation

A third scenario consistent with the observed decrease in chloride is the reduction in pressure of phase separation (Figure 27) resulting from either a physical decrease in depth of hydrothermal circulation or an effective decrease in the pressure of phase separation without a physical change to the geometry of hydrothermal flow. A physical change in depth of hydrothermal circulation may result from upwards melt migration (Delaney et al., 1998; Von Damm, 2004) or the sealing of hydrothermal flow paths by hydrothermal precipitates and deposits (Fournier, 1985; Lowell et al., 2003; Martin and Lowell, 2000).

In the first case, upwards melt migration, the magma injections would need to be relatively small to explain the transience of the changes following Dec. 17 seismicity (see section 5.3.1). Nevertheless, a small intrusion of magma from the lid of the magma lens is consistent with increased temperature, decreased chloride and increased seismicity.

For the second scenario, hydrothermal precipitation, there are several inconsistencies. Predicted timescales of sealing are on the order of years, much longer than the observed perturbation in chloride (Fournier, 1985; Martin and Lowell, 2000). Also, hydrothermal precipitates would first drive the pressure up by constricting flow before they drive the pressure down by limiting depth of circulation. Finally, intense seismicity is not very conducive to the restriction of hydrothermal flow. Thus, chloride and temperature changes following the Dec. 17 seismic swarm likely do not reflect changes in hydrothermal flow paths brought on by the accumulation of hydrothermal precipitates.

An effective reduction in pressure of phase separation without lasting changes to hydrothermal flow paths may be generated via multiple mechanisms. One such process has been modeled by Berndt et al. (2001) and involves evolution of hydrothermal fluid properties in a two phase system such that the pressure gradient in the upflow zone is reduced from cold hydrostatic seawater to hot hydrostatic vapor conditions. This process

has been applied to the evolution of the hydrothermal fluid at MEF in the wake of a magmatic event in order to explain the observation of hydrothermal effluent with virtually no chloride (Seyfried et al., 2003).

We attempted to apply the model of Berndt et al. (2001) in a similar fashion to the chloride dip following the Dec. 17 seismic swarm (Figure 47).

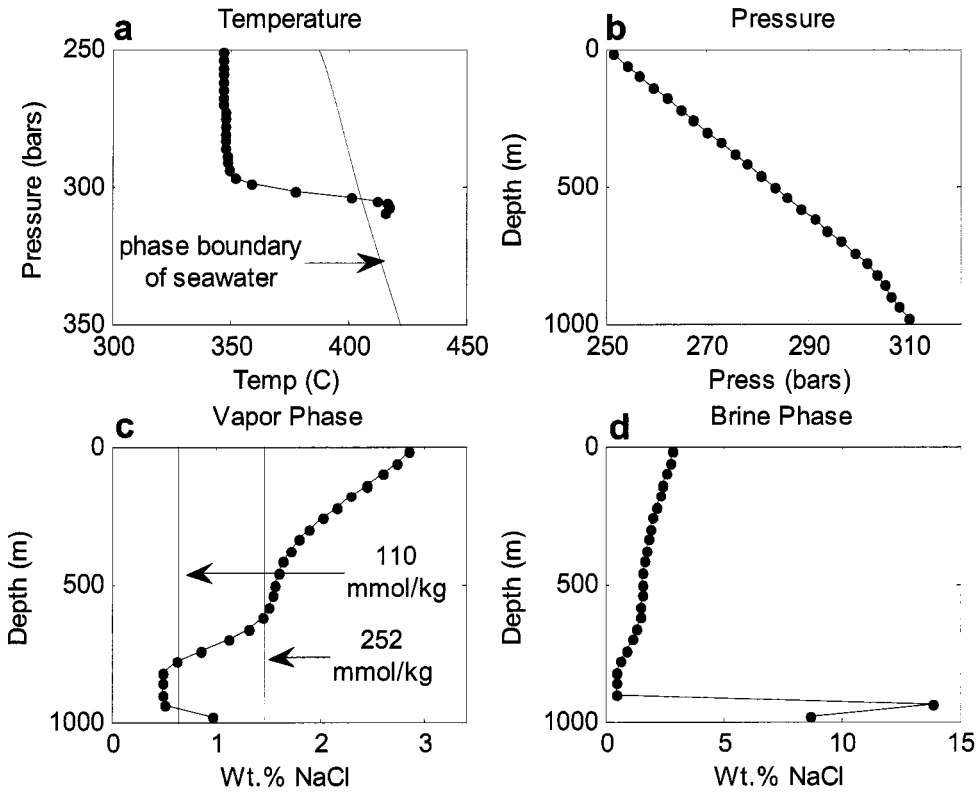

Figure 47. Results of model of Berndt et al. (2001) applied to PT conditions within range of inferred root zone at EPR. Each of the four plots shows how a given property varies with depth after heat has been added to the bottom cell at a rate of 334 kJ/s/m^2 for 5 days. (a) Temperature profile (black dots) and phase boundary of seawater (red line). (b) Pressure profile depicting variation in pressure gradient near the bottom of the cell. (c) Profile of vapor phase salinity showing chloride shift at depth similar to observed seafloor shift in chloride. (d) Profile of brine phase salinity. For the portion of the cell not in the two phase region, vapor and brine salinities are identical.

After model testing over a wide range of conditions, a combination of model parameters was achieved that reproduced the magnitude of the observed chloride change at the root zone without a physical change in depth of hydrothermal circulation which is constant for any given model run. However, the model failed to reproduce the timing and magnitude of the seafloor chloride signature owing to instabilities which prevented propagation of the chloride change to the surface.

5.3.4 Incomplete phase segregation – effective reduction in pressure of phase separation

The model of Berndt et al. (2001) represents the best available simulation of 2-phase flow but its inability to reproduce the chloride dip may reflect inaccuracy in one or more underlying assumptions. Specifically, the model assumes complete phase segregation at every point where phase separation occurs, as in an open system, but as we suggested in section 5.2.2 and at several other points in the foregoing discussion, phase separation may occur within a closed system for at least portions of the circulation pathway. We can calculate the required PT conditions of phase separation by assuming the minimum observed chloride during the dip on Dec. 23, 110 mmol/kg (Figure 38), represents the vapor phase and the maximum magnitude of chloride spikes occurring 7 days later on Dec. 31, ranging up to 700 mmol/kg (Figure 39), represents the conjugate brine phase. At 269 bars and 396.7°C, phase separation of seawater generates a 113 mmol/kg vapor phase and a 762 mmol/kg brine phase (Figure 48), very similar to the minimum and maximum observed chloride following the Dec. 17 seismic swarm. It is worth noting that implicit in the assumption that chloride spikes on Dec. 31 represent manifestation of a conjugate phase produced 1 week earlier is that when generated at shallow depths, brines can have relatively short residence times compared with brines generated deeper in the crust (Fontaine and Wilcock, 2006; Von Damm et al., 1997). PT conditions for this scenario, 269 bars and 396.7 °C, are 19 bars lower in pressure and 6.8 °C cooler in temperature than predicted PT conditions in the wake of the Nov. 27 swarm, 288 bars and 403.5 °C. The heat content of seawater under these lower PT conditions is

2085 J/g which is only slightly higher than the 2075 J/g calculated for the fluid under higher PT conditions in the wake of the Nov. 27 swarm suggesting adiabatic ascent of a fluid with bulk chloride equivalent to seawater.

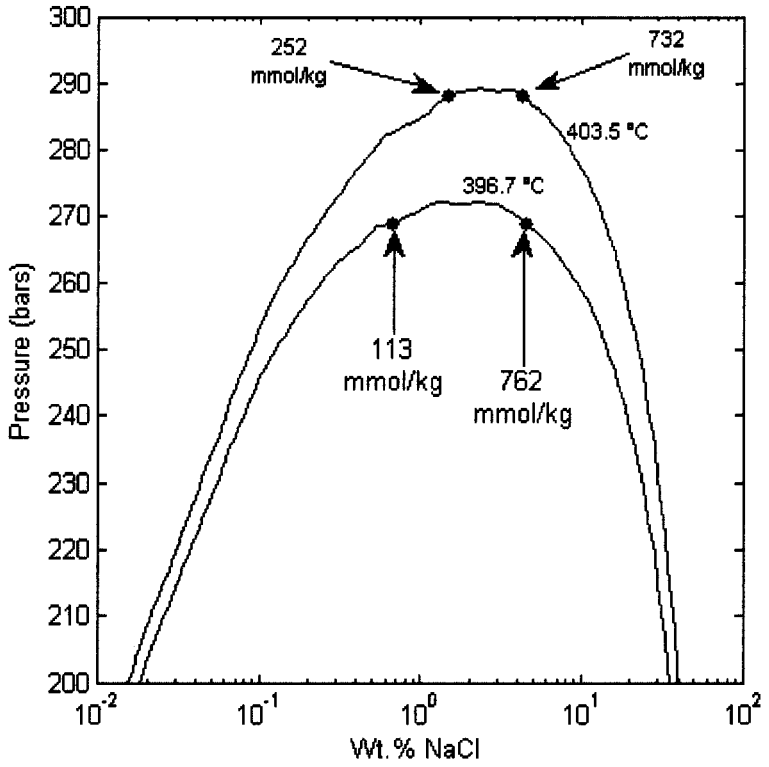

Figure 48. Shift in PT conditions following Dec. 17 inferred from minimum and maximum observed chloride within 2 weeks after the seismic swarm. We postulate an effective reduction in phase separation generated by incomplete phase segregation.

The implication of this flow path is that phase separation is occurring without subsequent phase segregation until much shallower in the upflow zone. In this manner, a decrease in chloride can be generated without significant heat input to the system or a permanent physical change in the depth of hydrothermal circulation which is consistent with the transient nature of the chloride change and the absence of a significant temperature increase.

This result conflicts with previous studies that argue for complete and immediate phase segregation (Fox, 1990; Seyfried et al., 2003; Von Damm et al., 2003). In addition to differences in density, phase segregation is attributed to crack geometry and differential flow of brines in confined spaces (Fontaine and Wilcock, 2006; Fox, 1990). In the present study, we observe what appears to be a transient decrease in the inferred pressure of phase separation owing to ascent of a non-segregated two-phase fluid. Density differences as discussed in section 5.2.2 are sufficiently similar that phase segregation may be less favored under the PT conditions calculated above. Furthermore, if the seismicity is attributed to cracking in the rock which increases permeability without changing the depth of hydrothermal circulation, then the new flow regime may be temporarily less conducive to phase segregation than the more confined flow paths prior to the seismic swarm (Figure 49). As steady state conditions are reestablished, brines are once again segregated closer to their point of origin and chloride returns to the baseline value observed before the seismic swarm.

Although this interpretation is the favored explanation of the chloride dip beginning on Dec. 17 and culminating on Dec. 23, we cannot rule out other possibilities with out either further empirical results or numerical modeling investigations (Table 14). Furthermore, it is important to note that none of these explanations can explain the temperature drop on Dec. beginning at the end of Dec. 22 followed by the temperature rebound about a day later. Here again, we emphasize that care must be taken when correlating subsurface chloride and temperature changes due to differences in how changes in each parameter behave during ascent.

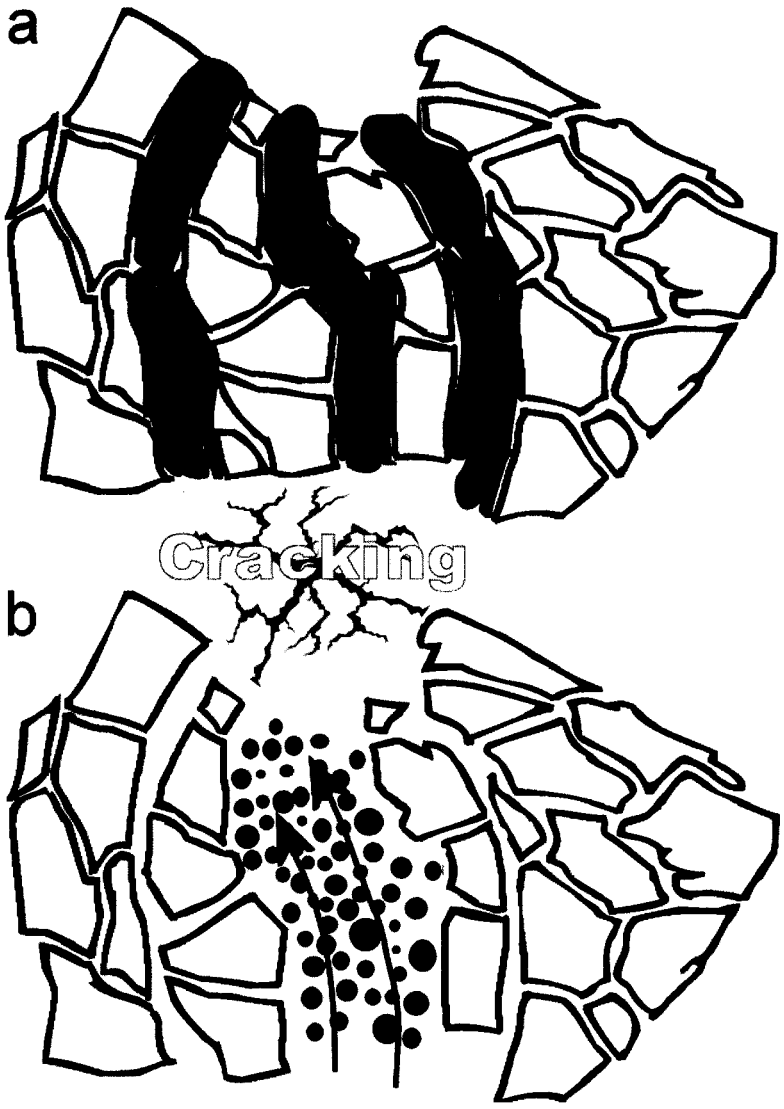

Figure 49. Schematic of cracking induced transition from segregated to non-segregated flow of vapor and brine following Dec. 17 seismic swarm. When brines (in blue) and vapors (in red) flow together as bulk fluid, the effective pressure of phase separation is reduced without a lasting physical change in the depth of the root zone.

Table 14. Comparison of possible sources of chloride dip occurring from Dec. 17 – Jan. 1. With the proper assumptions, all scenarios can explain the chloride decrease but each explanation has its limitations.

Process	PT Shift	Limitations
Magmatic heat input	heating at constant or decreasing pressure	• magnitudes of chloride dip and temperature increase are fairly small • duration of fluid perturbation is relatively short-lived • expected brine compositions higher than maximum observed chloride
Downward or lateral propagation of a hydrothermal cracking front	heating at constant or increasing pressure	• assumes heating of seawater well beyond the phase boundary without phase segregation • expected brine compositions higher than maximum observed chloride
Change in upflow zone pressure gradient causing an effective reduction in pressure of phase separation	decreasing pressure from increase in fluid temperature	• best available numerical model of phase separation and segregation reproduces observed changes at depth but cannot replicate seafloor changes, possibly reflecting the need for further refinement
Incomplete phase segregation causing an effective reduction in pressure of phase separation	decreasing pressure at constant enthalpy	• requires brine and vapor phases to remain in close proximity despite differences in fluid density.

6. Conclusion

In the 9-14 months leading up to an eruption at 9°50'N along the East Pacific Rise, we had in place a second generation conductivity-temperature package for the purpose of monitoring chloride and temperature on a magmatically robust mid-ocean ridge. The resulting data record represents the most temporally resolved data record to date of the evolution of hydrothermal chemistry preceding an eruption.

We interpret intense chloride variability following a seismic swarm on Nov. 27 as the violent release of subsurface brines by cracking in the rock which, however, does not substantially change the depth of hydrothermal circulation. PT conditions inferred from the range of chloride values observed during the week following the Nov. 27 seismic swarm place the PT conditions of the root zone at 288 bars and 403.5°C.

Chloride variability following the Dec. 17 seismic swarm is interpreted to be the result of an effective reduction in phase separation brought on by changes in the permeability structure of hydrothermal circulation and the resulting non-segregated flow of a 2-phase fluid with seawater chloride. PT conditions inferred from the chloride range following the Dec. 17 seismic swarm indicate a pressure of 269 bars and a 369.7°C. This shift in PT conditions relative to PT conditions inferred after the Nov. 27 seismic swarm is roughly equivalent to 200 m of vertical flow within the 2-phase region before the 2 phases finally segregate. Once again, there does not appear to be a permanent change in the physical depth of the root zone.

Our inferred PT conditions agree reasonably well with those of Von Damm (2004) who also uses chloride to estimate depth of circulation. However, we estimate much shallower cooler conditions than Foustoukos and Seyfried (2007) who use a chloride dependent silica geobarometer to put the root zone at 320 bars and 422°C. It may be that the chloride signature is distorted by phase separation during ascent while the Si content remains unchanged. However, chloride should be more conservative than Si,

not less. If, for instance, Si concentration goes down during ascent while chloride is conserved, inferred circulation depth would be artificially deep Foustoukos and Seyfried (2007). However we cannot rule out the possibility of supercritical conditions with our current dataset

The overall temperature decrease relative to the beginning of the record over the course of these two seismic swarms, the inferred tectonic nature of the seismicity and the overall upwards melt migration postulated for this period of ridge evolution suggest we may be observing recovery of the hydrothermal system from a recent dike emplacement occurring just prior to our instrument deployment.

Chapter 5 – Summary

Every year, huge amounts of seawater circulate through the hot rock at mid-ocean ridge spreading centers. Phase separation at high temperatures and pressures splits this fluid in two separate fluids with vast differences in chloride concentration. Chloride values below seawater levels over decadal timescales suggest the presence of large subsurface chloride-enriched brines.

We have constructed and calibrated an instrument capable of making in-situ chloride measurements in high temperature fluids. Our measurements of hydrothermal fluid from two divergent plate boundaries have allowed us to identify possible brine removal mechanisms and constrain brine properties in ways not possible with conventional chloride measurements. We also use the data to establish likely pressure-temperature conditions of fluid circulation and show how these conditions evolve. The primary conclusions of the research are listed below:

- Calibrated in-situ chloride sensor at temperatures relevant to Juan de Fuca Ridge, 220-300 bars and temperatures up to 380°C
- Calibrated in-situ chloride sensor at temperatures relevant to 9°50' N on the East Pacific Rise, 250-300 bars and temperatures up to 400°C
- Observed tidally correlated changes in high temperature vent effluent at Main Endeavour Field on the Juan-de-Fuca Ridge and observed non-tidal changes on timescales as short as minutes and hours
- Tidal signature consistent with the presence of subsurface mixing at depths ranging from 486 to 695 meters, possibly involving near-critical fluids.
- Twice observed hydrothermal response to intense seismic activity at 9°N50'N (9N) on the East Pacific Rise

- Constrained conditions of phase separation at 9N to pressures between 288 to 269 bars and temperatures between 396.7 and 403.5°C
- Observed short-lived chloride spikes lasting up to 7 minutes and almost 3× greater than local baseline values

This research required the construction of a hydrothermal simulator for sensor calibration and the investigation of new materials potentially suitable for an extreme environment. Tested materials include Alumina, Alumina stabilized-zirconia, Beryllia, Zirconia as well as several proprietary materials. Based on experiments in the field and under simulated conditions, Zirconia exhibited the greatest degree of stability.

The large amounts of unique multi-dimensional data generated by our sensor necessitated data manipulation and processing methods not readily available. Thus, an important result of the research was the development of a Matlab-based interface designed to facilitate graphical exploration of extensive time-series measurements. Additional programs were written to analyze chloride data in the context of the pressure-temperature-NaCl surface of Bischoff and Pitzer (1989).

Lessons learned during engineering the instrument and data processing methods highlight the challenges facing an observatory approach to oceanography. Our solutions to those challenges could be a useful contribution to the infrastructure needed for the tectonic plate observatories currently under construction.

BIBLIOGRAPHY

Alt J. C. (1995) Subseafloor processes in mid-ocean ridge hydrothermal systems. In *Mid-ocean ridges; hydrothermal interactions between the lithosphere and oceans, AGU Monograph* **148** (eds. C. R. German, J. Lin, L. M. Parson), 243-266. AGU.

Alt J. C. and Bach W. (2003) Alteration of oceanic crust: subsurface rock-water interactions. In *Energy and Mass Transfer in Marine Hydrothermal Systems* (eds. P. E. Halbach, V. Tunnicliffe and J. R. Hein), 123-161. Dahlem University Press.

Anderko A. and Pitzer K.S. (1993) Equation-of-state representation of phase equilibria and volumetric properties of the system NaCl-H_2O above 573 K. *Geochim. Cosmochim. Acta* **57**, 1657-1680.

Baker E. T., Lowell R. P., Resing J. A., Feely R. A., Embley R. W., Massoth G. J., and Walker S. L. (2004) Decay of hydrothermal output following the 1998 seafloor eruption at Axial Volcano: Observations and models. *J. Geophys. Res.* **109,** Art. No. B01205.

Baker E. T., Massoth G. J., Feely R. A. and Cannon, G. A. (1998) The rise and fall of the CoAxial hydrothermal site, 1993-1996. *J. Geophys. Res.-Solid Earth* **103,** 9791-9806.

Barber C. B., Dobkin D. P., and Huhdanpaa H. T. (1996) The Quickhull Algorithm for Convex Hulls. *ACM Trans. on Mathematical Software* **22**, 469-483.

Berndt M. E., Person M. E., and W. E. Seyfried Jr.(2001) Phase separation and two-phase flow in seafloor hydrothermal systems: Geophysical modeling in the NaCl-H_2O system, paper presented at the Eleventh Annual V. M. Goldschmidt Conference, Geochem. Soc., Hot Springs, VA.

Berndt M. E. and Seyfried, Jr. W. E. (1990) Boron, bromine and other trace elements as clues to the fate of chlorine in mid-ocean ridge vent fluids. *Geochim. Cosmochim. Acta* **54,** 2235-2245.

Berndt M. E., Seyfried, Jr. W. E., Janecky D. R. (1989) Plagioclase and epidote buffering of cation ratios in mid-ocean ridge hydrothermal fluids: Experimental results in and near the supercritical region. *Geochim. Cosmochim. Acta* **53,** 2283-2300.

Bianchi H., Corti H. R., and Fernandezprini R. (1989) The conductivity of concentrated aqueous mixtures of NaCl and $MgCl_2$ at 25 °C. *J. Sol. Chem.* **18,** 485-491.

Bischoff J. L. and Pitzer K. S. (1989) Liquid-Vapor Relations for the System NaCL-H2O: Summary of the P-T-x Surface from 300 to 500 °C. *Am. J. Sci.* **289,** 217-248.

Bischoff J. L. and Rosenbauer (1989) Salinity variations in submarine hydrothermal systems by layered double-diffusive convection. *J. Geology* **97,** 613-623.

Bischoff J. L. and Pitzer K. S. (1985) An empirical equation of state for hydrothermal seawater (3.2 % NaCl). Am. J Sci. **285**, 725-763.

Butterfield D. A., Seyfried, Jr. W. E., Lilley M. D. (2003) Composition and Evolution of Hydrothermal Fluids. In *Energy and Mass Transfer in Marine Hydrothermal Systems* (eds. P. E. Halbach, V. Tunnicliffe and J. R. Hein), 123-161. Dahlem University Press.

Butterfield D. A., Roe K. K., Kadko D., Tivey M. K. (2001) Tidal Variability in Diffuse Flow Vents in the Main Endeavour Field. *Eos Trans. AGU* **82**(47) Fall Meet. Suppl., Abstract OS21B-0449.

Butterfield, D. A., Jonasson I. R., Massoth G. J., Feely R. A., Roe K. K., Embley R. E., Holden J. F., McDuff R. E., Lilley M. D. and Delaney J. R. (1997) Seafloor eruptions and evolution of hydrothermal fluid chemistry. *Transactions of the Royal Society of London, Series A: Mathematical and Physical Sciences* **355,** 369-386.

Butterfield D. A., McDuff R. E., Mottl M. J., Lilley M. D., Lupton J. E., and Massoth G. J. (1994) Gradients in the composition of hydrothermal fluids from the Endeavour segment vent field: Phase separation and brine loss. *J. Geophys. Res.-Solid Earth* **99**, 9561-9583.

Butterfield D. A., Massoth G. J., McDuff R. E., Lupton J. E. and Lilley M. D. (1990) Geochemistry of hydrothermal fluids from axial seamount emissions study vent field, Juan de Fuca Ridge: subseafloor boiling and subsequent fluid rock interaction. *J. Geophys. Res.-Solid Earth and Planets* **95,** 12895-12921.

Cherkaoui A. S. M., Wilcock W. S. D., Dunn R. A., and Toomey D. R. (2003) A numerical model of hydrothermal cooling and crustal accretion at a fast spreading mid-ocean ridge. *Geochem. Geophys. Geosys.* **4** (9), 19 pp.

Converse D.R., Holland H. D. and Edmond J. M. (1984) Flow rates in the axial hot springs of the East Pacific Rise (21 °N): Implications for the heat budget and the formation of massive sulfide deposits. *Earth Planet. Sci. Lett.* **69,** 159-175.

Crone T. J. and Wilcock, W. S. D. (2005) Modeling the effects of tidal loading on mid-ocean ridge hydrothermal systems. *Geochemistry Geophysics Geosystems* **6** (7). 25 pp.

Cudrak C. F. and Clowes R. M. (1993) Crustal structure of Endeavour ridge segment, Juan de Fuca ridge, from a detailed seismic refraction study. *J. Geophys. Res.* **98,** 6329-6349.

Currie D. J. and Gordon A. R. (1960) Transference numbers for the concentrated aqueous sodium chloride solutions, and the ionic conductances for potassium and sodium chlorides. *J. Phys. Chem.* **64**, 1751-1753.

De Boor C. (1978) A practical guide to splines. *Applied Mathematical Sciences* **27**, 1-392.

Delaney J. R., Kelley D. S., Lilley M. D., Butterfield D. A., Baross J. A., Wilcock W. S. D., Embley R. W. and M. Summit (1998) The quantum event of oceanic crustal accretion: impacts of diking at mid-ocean ridges. *Science* **281,** 222-230.

Delaney J. R., Robigou V. and McDuff R. E. (1992) Geology of a vigorous hydrothermal system on the Endeavour segment, Juan de Fuca ridge. *J. Geophys. Res.-Solid Earth* **97**, 19663-19682.

Detrick R. S., Buhl P., Vera E., Mutter J., Orcutt J., Madsen J. and T. Brocher (1987) Multi-channel seismic imaging of a crustal magma chamber along the East Pacific Rise. *Nature* **326,** 35-41.

Detrick R. S., Carbotte S., Van Ark E., Canales J. P., Kent G., Harding A., Diebold J. and Nedimovic M. (2002) New multichannel seismic constraints on the crustal structure of the Endeavour Segment, Juan de Fuca Ridge: Evidence for a crustal magma chamber. *Eos Trans. AGU* **83**(47), Fall Meet. Suppl. Abstract T12B-1316.

Ding K., Seyfried W. E., Jr., Zhang Z., Foustoukos D. and Pester N. J. (2005) In-situ Chemistry of Hydrothermal Fluids from Black Smokers in Main Endeavour Field, Juan de Fuca Ridge. *Eos Trans. AGU* Fall Meeting Suppl., Abstract T31A-0488.

Ding K., Seyfried W. E., Jr., Tivey M. K., and Bradley A. M. (2001) In-situ measurement of dissolved H_2 and H_2S in the high temperature hydrothermal vent fluids at the Main Endeavour Field, Juan de Fuca Ridge. *Earth Planet. Sci. Lett.* **186,** 417-425.

Ding K. and Seyfried W. E., Jr. (1996) Direct pH measurement of NaCl-bearing fluid with an in-situ sensor at 400 °C and 40 megapascals. *Science* **272**, 1634-1636.

Ding K. and Seyfried W. E., Jr. (1995) In-situ measurement of dissolved H_2 in aqueous fluid at elevated temperatures and pressures. *Geochim. Cosmochim. Acta* **59**, 4769-4773.

Fontaine F. J., Wilcock W. S. D and Butterfield D. A. (2007) Physical controls on the salinity of mid-ocean ridge hydrothermal vent fluids. *Earth Planet. Sci. Lett.* **257,** 132-145.

Fontaine F. J. and Wilcock W. S. D. (2006) Dynamics and storage of brine in mid-ocean ridge hydrothermal systems. *J. Geophys. Res.* **111,** Art. No. B06102.

Fontaine F. J., Wilcock W. S. D. and Butterfield D. A. (2005), Physical Controls On The Salinity Of Mid-Ocean Ridge Hydrothermal Vent Fluids, *Eos Trans. AGU,* **86**(52), Fall Meet. Suppl., Abstract T31B-0497.

Fornari D., Tivey M., Schouten H., Perfit M., Yoerger. D, Bradley A., Edwards M., Haymon R., Scheirer D., Von Damm K., Shank T. and A. Soule (2004) Submarine lava flow emplacement at the East Pacific Rise 9° 50'N: Implications for uppermost ocean crust stratigraphy and hydrothermal circulation. In *Mid-ocean ridges: hydrothermal interactions between the lithosphere and oceans, AGU Monograph* **148** (eds. C. R. German, J. Lin and L. M. Parson), 187-217. AGU.

Fornari D. J., Shank T., Von Damm K. L., Gregg T. K. P., Lilley M., Levai G., Bray A., Haymon R. M., Perfit M. R., and R. Lutz (1998) Time-series temperature measurements at high-temperature hydrothermal vents, East Pacific Rise 9°49-51'N: Evidence for monitoring a crustal cracking event, *Earth & Planet. Sci. Lett.,* **160,** 419-431.

Fornari D. J., Haymon R. M., Perfit M. R., Gregg T. K. P. and H. M. Edwards (1998) Axial summit trough of the East Pacific Rise (9°-10°N: Geological characteristics and evolution of the axial zone on fast spreading mind-ocean ridges. *J. Geophys. Res.* **103,** 9827-9855.

Fournier R. O. (1985) The behavior of silica in hydrothermal solutions. *Reviews in Economic Geology* **2**, 45–62.

Foustoukos D .I. and W.E. Seyfried Jr. (2007) Quartz solubility in the two-phase and critical region of the NaCl-KCl-H2O system: Implications for submarine hydrothermal vent systems at 9°50'N East Pacific Rise. *Geochim. Cosmochim. Acta* **71,** 186-201.

Fox C. (1990) Consequences of phase separation on the distribution of hydrothermal fluids at ASHES vent field, Axial Volcano, Juan de Fuca Ridge. *J. Geophys. Res.* **95,** 12,923-12,926.

Frantz J. D. and Marshall W. L. (1982) Electrical conductances and ionization constants of calcium chloride and magnesium chloride in aqueous solutions at temperatures to 600 °C and pressures to 4000 bars. *Am. J. Sci.* **282**, 1666-1693.

German C. R. and J. Lin (2004) The thermal structure of the oceanic crust, ridge-spreading and hydrothermal circulation: How well do we understand their inter-connections? In *Mid-ocean ridges: hydrothermal interactions between the lithosphere and oceans, AGU Monograph* **148** (eds. C. R. German, J. Lin, L. M. Parson), 1-18. AGU.

Goldfarb M. S. and Delaney J. R. (1988) Response of two-phase fluids to fracture configurations within submarine hydrothermal systems. *J. Geophys. Res.* **93,** 4585-4594.

Goldfarb M. S., Converse D. R., Holland H. D., and Edmond J. M. (1983)The genesis of hot spring deposits on the East Pacific Rise, 21°N. In *Econ. Geol. Monograph 5* (eds. H. Ohmoto and B. J. Skinner), 184-197. The Economic Geology Publishing Company.

Haymon R. M., Fornari D. J., Edwards M. H., Carbotte S., Wright D. and K. C. Macdonald (1991) Hydrothermal vent distribution along the East Pacific Rise Crest (9°09'-54'N) and its relationship to magmatic and tectonic processes on fast-spreading mid-ocean ridges. *Earth & Planet. Sci Lett.* **104,** 513-534.

Henstock T. J., Woods A. W. and R. S. White (1993) The accretion of oceanic crust by episodic sill intrusion. *J. Geophys. Res.-Solid Earth* **98,** 4143-4161.

Johnson H. P., Hutnak M., Dziak R. P., Fox, C. G., Urcuyo I., Cowen J. P., Nabelekk J. and Fisher C. (2000) Earthquake-induced changes in a hydrothermal system on the Juan de Fuca mid-ocean ridge. *Nature* **407,** 174-177.

Johnson J. W. and Norton D. (1991) Critical phenomena in hydrothermal systems: state, thermodynamic, electrostatic and transport properties of H_2O in the critical region. *American Journal of Science* **291,** 541-648.

Kadko D. (1994) Time-series gamma spectrometry of diffuse flow from the North Cleft segment of the Juan de Fuca Ridge. *Eos Trans. AGU* **75**(44) Fall Meet. Suppl., 307.

Kadko D. K. and Butterfield D. A. (1998) The relationship of hydrothermal field composition and crustal residence time to maturity of vent fields on the Juan de Fuca Ridge. *Geochim. Cosmochim. Acta* **62**, 1521-1533.

Kelley, D. S., Baross J. A. and Delaney J. R. (2002), Volcanoes, fluids, and life at mid-ocean ridge spreading centers, *Annu. Rev. Earth Planet. Sci.*, **30**, 385–491.

Kelley D. S., Robinson P. T. and Malpas J. G.(1992) Processes of brine generation and circulation in the oceanic crust: Fluid inclusion evidence from the Troodos Ophiolite, Cyprus. *J. Geophys. Res.* **97,** 9307-9322.

Kent G. M., Harding A. J. and J. A. Orcutt (1993) Distribution of magma beneath the East Pacific Rise between the Clipperton transform and the 9°17' deval from forward modeling of common depth point data. *J. Geophys. Res.-Solid Earth.* **98,** 13945-13969.

Kinoshita M. S., Von Herzen R. P., Matsubayahsi O. and Fujioka K. (1997) Tidally-driven effluent detected by long-term temperature monitoring at the TAG hydrothermal mound, Mid-Atlantic Ridge. *Phys. Earth Planet. Inter.* **108**, 143-154.

Larson B. I., Olson E. J. and M. D. Lilley (2007) In situ measurement of dissolved chloride in high temperature hydrothermal fluids. *Geochm. Cosmochim. Acta.* **71,** 2510-2523.

Larson B. I., Olson E. J. and M. D. Lilley (in prep) Parameters of subsurface brines and hydrothermal processes 12-15 months after the 1999 magmatic event at Main Endeavour Field inferred from in-situ time series measurements of chloride and temperature.

Lewis K. C. and Lowell R. P. (2004) Mathematical modeling of phase separation of seawater near an igneous dike. *Geofluids* **4,** 197-209.

Lilley M. D., Butterfield D. A., Lupton J. E. and Olson E. J. (2003) Magmatic events can produce rapid changes in hydrothermal vent chemistry. *Nature* **422**, 878-881.

Lister C. R. B. (1974) On the penetration of water into hot rock. *Geophys. J. R. Astr. Soc.* **39**, 465-509.

Little S. A., Stolzenbach K. D. and Grassle F. J. (1988) Tidal current effects on temperature in diffuse hydrothermal flow: Guaymas Basin. *Geophys. Res. Lett.* **15**, 1491–1494. (Correction to "Tidal current effects on temperature in diffuse hydrothermal flow: Guaymas Basin." *Geophys. Res. Lett.* **16**, 985–986, 1989.

Lowell R. P. and Germanovich L. N. (1997) Evolution of a brine saturated layer at the base of a ridge-crest hydrothermal system. *J. Geophys. Res.* **102,** 10245-10256.

Lowell R. P., Yao Y. and L. N. Germanovich (2003) Anhydrite precipitation and the relationship between focused and diffuse flow in seafloor hydrothermal systems. *J. Geophys. Res.* **108,** Art. No. doi:10.1029/2002JB002371.

Malinvero, A. and Pockalny R. A. (1990) Abyssal hill topography as an indicator of episodicity in crustal accretion and deformation. *Earth Planet. Sci. Lett.* **99,** 154-196.

Martin J. T. and R. P. Lowell (2000) Precipitation of quartz during high-temperature, fracture-controlled hydrothermal upflow at ocean ridges: Equilibrium versus linear kinetics, *J. Geophys. Res.* **105**, 869– 882.

Massoth G. J., Butterfield D. A., Lutpon J. E., McDuff R. E., Lilley M. D., Jonasson I. R. (1989) Submarine venting of phase separated hydrothermal fluids at Axial Volcano, Juan de Fuca Ridge. *Nature* **340,** 702-705.

McClain, J. S., Begnaud M. L., Wright M. A., Fondrk J. and Von Damm G. K.. (1993) Seismicity and tremor in a submarine hydrothermal field: the northern Juan de Fuca Ridge. *Geophys. Res. Lett.* **20**, 1883-1886.

Michael P. J. and Cornell W. C. (1998) Influence of spreading rate and magma supply on crystallization and assimilation beneath mid-ocean ridges: Evidence from chlorine and major element chemistry of mid-ocean ridge basalts. *J. Geophys. Res.* **103,** 18325-18356.

Oosting, S .E. and K. L. Von Damm (1996) Bromide/chloride fractionation in seafloor hydrothermal fluids from 9-10°N East Pacific Rise. *Earth & Planet. Sci. Lett.,* **145,** 133-145.

Parks T. W. and Burrus C. S. (1987) Conversion of analog-to-digital transfer functions. In *Digital Filter Design*, 213-218, John Wiley & Sons, New York.

Pawlowicza R., Beardsley B., Lentz S. (2002) Classical tidal harmonic analysis including error estimates in MATLAB using T_TIDE. *Computers & Geosciences* **28,** 929–937.

Povodyrev A. A., Anisimov M. A., Sengers J. V., Marshall W. L., and Levelt Sengers J. M. H. (1999) Critical locus of aqueous solutions of sodium chloride *Int. J. of Thermophys.,* **20,** 1529-1545.

Quist A. S. and Marshall W. L. (1969) The electrical conductances of some alkali metal halides in aqueous solutions from 0 to 800°C and at pressures to 4000 bars. *J. Phys. Chem.* **73,** 978-985.

Quist A. S. and Marshall W. L. (1968) Electrical conductances of aqueous sodium chloride solutions from 0 to 800 °C and at pressures to 4000 bars. *J. Phys. Chem.* **72**, 684-703.

Rogers P. S. Z. and Pitzer K. S. (1982) Volumetric properties of aqueous sodium chloride solutions *J. Phys. Chem. Ref. Data* **11,** 15-81.

Scheirer D. S., Shank T. M. and D. J. Fornari (2006) Temperature variations at diffuse and focused flow hydrothermal vent sites along the northern East Pacific Rise. *Geochem. Geophys. Geosys.* **7,** Q03002, doi:10.1029/2005GC001094.

Schoofs, S. and Hansen U. (2000) Depletion of a brine layer at the base of ridge-crest hydrothermal systems. *Earth Planet. Sci. Lett.* **180:** 341-353.

Schultz A., P. Dickson and Elderfield H. (1996) Temporal variations in diffuse hydrothermal flow at TAG. *Geophys. Res. Lett.* **23**, 3471–3474.

Seewald J. S., Cruse A., Saccocia P. (2003) Aqueous volatiles in hydrothermal fluids from the Main Endeavour Field, northern Juan de Fuca Ridge: temporal variability following earthquake activity. *Earth. Planet.Sci. Lett.* **216**, 575-590.

Seewald J. S. and Seyfried, Jr. W. E. (1990) The effect of temperature on metal mobility in subseafloor hydrothermal systems: constraints from basalt alteration experiments. *Earth Planet. Sci. Lett.* **101**, 388-403.

Seyfried, Jr., W. E., Seewald J. S., Berndt M. E., Ding K. and Foustoukos D. I. (2003) Chemistry of hydrothermal vent fluids from the Main Endeavour Field, northern Juan de Fuca Ridge: geochemical controls in the aftermath of June 1999 seismic events. *J. Geophys. Res.* **108**, Art. No. 2429.

Seyfried, Jr. W. E., and Ding K. (1995) Phase equilibria in subseafloor hydrothermal systems; a review of the role of redox, temperature, pH and dissolved Cl on the chemistry of hot spring fluids at mid-ocean ridges. In *Seafloor hydrothermal systems; physical, chemical, biological, and geological interactions* (eds. S. E. Humphris, R. A. Zierenberg, L. S. Mullineaux and R. E. Thomson), 248-272. AGU.

Seyfried, Jr. W. E., Berndt M. E. and Janecky D. R. (1986) Chloride depletions and enrichments in seafloor hydrothermal fluids: constraints from experimental basalt alteration studies **50,** 469-475.

Smedley S. I. (1980) *The interpretation of ionic conductivity in liquids*. Plenum Press, New York.

Sohn R. A., Webb S. C. and J. A. Hildebrand (2004) Fine scale seismic structure of the shallow volcanic crust on the East Pacific Rise at 9°50'N. *J. Geophys. Res.* **109,** Art.. No. B12104.

Sohn, R. A., Fornari D. J., Von Damm K. L., Hildebrand J. A., and S. C. Webb (1998) Seismic and hydrothermal evidence for a cracking event on the East Pacific Rise at 9°50'N. *Nature* **396,** 159-16.

Tivey M. K., Bradley A. M., Joyce T. M., and Kadko D. (2002) Insights into tide-related variability at seafloor hydrothermal vents from time series temperature measurements. *Earth Planet. Sci. Lett.* **202**, 693-707.

Tivey, M. A. and Johnson H. P. (2002) Crustal magnetization reveals subsurface structure of Juan de Fuca Ridge hydrothermal vent. *Geology.* **30,** 979-982.

Tivey M. K., Olson O., Miller V. W., Light R. D. (1990) Temperature measurements during initiation and growth of a black smoker chimney. *Nature* **346,** 51-54.

Tolstoy M., Cowen J. P., Baker E. T., Fornari D. J., Rubin K. H., Shank T. M., Waldhauser F., Bohnenstiehl D. R., Forsyth D. W., Holmes R. C., Love B., Perfit M. R., Weekly R. T., Soule S. A., Glazer B. (2006) A Sea-Floor Spreading Event Captured by Seismometers. *Science* **314,** 1920-1922.

Turcotte D L. and Schubert G. (2002) *Geodynamics*. Cambridge University Press, New York.

Van Ark E. M., Detrick R. S., Canales J. P., Carbotte S. M., Harding A. J., Kent G. M., Nedimovic M. R., Wilcock W. S. D., Diebold J. B. and J. M. Babcock (2007) Seismic structure of the Endeavour Segment, Juan de Fuca Ridge: Correlations with seismicity and hydrothermal activity. *J. Geophys. Res.* **112,** B02401, doi:10.1029/2005JB004210.

Vanýsek P. (2005) Ionic conductivity and diffusion at infinite dilution. In *CRC Handbook of Chemistry and Physics* (ed. D. R. Lide), 5-76 – 5-78. CRC Press.

Veirs S. R., McDuff R. E., Stahr F. R. (2006) Magnitude and variance of near-bottom horizontal heat flux at the Main Endeavour hydrothermal vent field. *Geochem. Geophys. Geosys.* **7,** Art. No. Q02004.

Veirs S. R., Stahr F. R., McDuff R. E., Thompson R. E., Yoerger D. R. and Bradley A. M. (2001) Measurements and models of heat flux magnitude and variance from the Main Endeavour hydrothermal vent field. *EOS Trans. AGU,* **82**(47), Fall Mett. Suppl., Abstract OS21B-0444.

Von Damm, K. L. (2004) Evolution of the hydrothermal system at East Pacific Rise 9°50'N; geochemical evidence for changes in the upper oceanic crust. In *Mid-ocean ridges; hydrothermal interactions between the lithosphere and oceans, AGU Monograph* **148** (eds. C. R. German, J. Lin, L. M. Parson), 243-266. AGU.

Von Damm, K. L. and M. D. Lilley (2004) Diffuse flow hydrothermal fluids from 9°50'N East Pacific Rise: Origin, evolution and biogeochemical controls. In *The Subsurface Biosphere at Mid-Ocean Ridges, AGU Monograph* **144** (eds.W.S.D. Wilcock, E. F. DeLong, D.S. Kelley, J.A. Baross and S.C. Cary), 243-266. AGU.

Von Damm, K L; Lilley, M D; Shanks, W C, III; Brockington, M; Bray, A M; O'Grady, K M; Olson, E; Graham, A; Proskurowski, G; Collier, R; Cowen, J; Haymon, R; Tivey, M K; Fornari, D; Nakamura, K; McLaughlin-West, E; Shank, T; Kaye, J; Hobson, J; Sarrazin, J; Sparrow, M; Hubbard, D; McGee, D; Brinson, S and Cushman, B (2003) Extraordinary phase separation and segregation in vent fluids from the southern East Pacific Rise. *Earth Planet. Sci. Lett.* **206,** 365-378.

Von Damm K. L. (2000) Chemistry of hydrothermal vent fluids from 9°-10° N, East Pacific Rise: "Time Zero," the immediate post-eruptive phase. *J. Geophys. Res.-Solid Earth* **105,** 11203-11222.

Von Damm K. L., Buttermore L. G., Oosting S. E., Bray A. M., Fornari D. J., Lilley M. D. and Shanks III W. C. (1997) Direct observation of the evolution of a seafloor 'black smoker' from vapor to brine. *Earth Planet. Sci. Lett.* **149,** 101-111.

Von Damm K. L., Oosting S. E., Kozlowski R., Buttermore L. G., Colodner D. C., Edmonds H. N., Edmond J. M. and J. M. Grebmeier (1995) Evolution of East Pacific Rise hydrothermal vent fluids following a volcanic eruption. *Nature.* **375,** 47-50.

Von Damm, K. L. (1995) Controls on the chemistry and temporal variability of seafloor hydrothermal fluids. In *Seafloor hydrothermal systems: physical, chemical, biological and geological interactions, AGU Monograph* **91** (ed. S. E. Humphris), 222-247. AGU.

Welch P. D. (1967) The Use of fast fourier transform for the estimation of power spectra: a method based on time averaging over short, modified periodograms. *IEEE Trans. Audio Electroacoustics*. **AU-15**, 70-73.

Wheat C. G., Jannasch H. W., Plant J. N., Moyer C. L., Sansone F. J., and McMurtry G. M. (2000) Continuous sampling of hydrothermal fluids from Loihi Seamount after the 1996 event. *J. Geophys. Res.-Solid Earth* **105**, 19353-19367.

Wilcock W. S. D. (1998) Cellular convection models of mid-ocean ridge hydrothermal circulation and the temperatures of black smoker fluids. *J. Geophys. Res.-Solid Earth* **103,** 2585-2596.

Wilcock W. S. D. (2004) Physical response of mid-ocean ridge hydrothermal systems to local earthquakes. *Geochemistry Geophysics Geosystems* **105**(11), 26 pp.

VITA

Ben Larson was born in Ithaca, New York and raised in Cincinnati, Ohio. He acquired his bachelor's degree in chemistry from The Ohio State University in the spring of 1999, where he worked on the spectroscopic study of ogranometallic compounds using Nd:YAG pumped dye lasers. Matriculating in the field of Oceanography at the University of Washington in the autumn of 1999, he has worked on a variety of projects, including in-situ sensing of high temperature hydrothermal fluids and the gas chromatographic study of hydrothermal volatiles. He obtained his masters degree in Chemical Oceanography from the University of Washington in the winter of 2003 and did a stint as a science writer for The Oregonian in the summer of 2006. In 2008 he earned a Doctor of Philosophy at the University of Washington in Chemical Oceanography.